

Investigation of the thermodiffusion behavior
of complex fluids
and development of new methods

I n a u g u r a l - D i s s e r t a t i o n

zur

Erlangung des Doktorgrades

der Mathematisch-Naturwissenschaftlichen Fakultät

der Heinrich-Heine-Universität Düsseldorf

vorgelegt von

Philipp Naumann

aus Solingen

Jülich, Mai, 2014

aus dem Institut für Komplexe Systeme
am Forschungszentrum Jülich

Gedruckt mit der Genehmigung der Mathematisch-Naturwissenschaftlichen Fakultät der
Heinrich-Heine-Universität Düsseldorf

Referent: Prof. Dr. J. K. G. Dhont

Korreferent: Prof. Dr. S. U. Egelhaaf

Mentorin: PD Dr. S. Wiegand

Tag der mündlichen Prüfung: 30.06.2014

ABSTRACT

Thermodiffusion or thermophoresis occurs when a fluid mixture is exposed to a temperature gradient, leading to partial separation of the different components. It is still an unresolved non-equilibrium problem in physical chemistry. Thermodiffusion can be used for large scale separation and polymer characterization and furthermore it has been related to the origin of life occurring at deep sea regions with strong temperature gradients caused by hot vents or other volcano activities. The basic parameter is referred to as the Soret coefficient which is defined as the ratio of the thermal diffusion coefficient D_T and the mass diffusion coefficient D .

Despite a long time of research there is still a lack of a microscopic understanding of thermodiffusion. In order to study the origin of thermodiffusion, it is required to use well suited model systems and reliable methods. The model systems need to be accessible with theoretical concepts and show simplified geometries such as spheres. Additionally the model system must allow a systematic variation of properties such as size, mass or charge. The requirements for experimental methods are a small sample volume to be able to use rare materials and a well shaped experimental geometry to be accessible by theoretical models, for example well characterized walls, edges and interfaces. Furthermore measurements need to be contact free in order to minimize artificial distortions like the sample-removal geometry through an outlet. This work contains both aspects, the development of a new experimental method and the systematic investigation of microemulsion droplets, which can be regarded as a tunable colloidal model system.

A well suited experimental method employs the classical so-called thermogravitational columns (TGs), which were one of the first devices using thermodiffusion for separation, and which rely on sample extraction and additional measurements to determine the concentration and thereby the thermodiffusion properties. One main aspect of this work was the

development of a classical TG combined with an optical detection method which requires only very small sample volumes. This project was accomplished in cooperation with the group of M. M. Bou-Ali at the Mondragon-University. The thermogravitational micro column (μ -TG) was constructed with a small sample volume of 50 μ L for investigation of very rare or expensive samples such as biological samples. The dimensions are chosen to achieve a parabolic, laminar flow field inside the column, which is required for theoretical modeling. We chose a gap width of only around 500 μ m and a height of 3 cm. The μ -TG is operated contact free by using an interferometrical detection method to determine the concentration differences at two different heights of the column. This optical method allows sensitive and time resolved measurements of the concentration difference. Although, the analysis of the time dependent concentration profile was not yet possible with existing theoretical models which assume infinite short rising times of the temperature gradient. We used an active phase tracking procedure using a piezo actuator at one of the mirrors, which changes the mirror position, leading to the phase difference. This robust method is independent of the intensity and contrast fluctuations. The μ -TG has been validated by measuring three binary benchmark mixtures and by investigating the mixture of toluene and *n*-hexane. The obtained results agree within 5% with literature results.

Additionally, measurements of a microemulsion system were performed, which allow a systematic investigation of the thermal diffusion behavior as function of the microemulsion droplet size and their interfacial tension. The size dependence of the thermodiffusion is controversially discussed. Theoretical studies propose the Soret coefficient a linear, quadratic and power laws of higher order. Experimentally a linear and quadratic size dependence of the Soret coefficient for hard and soft colloids has been found. Two different studies on the same sample system led to a linear and a quadratic dependence. One reason for this discrepancy might be the surface properties of the studied colloidal systems. Although hard spheres with different sizes can be synthesized, the grafting density or charge may differ substantially. A phase transition temperature of colloidal systems stemming from different batches differ often by several 10 K. To overcome this drawback, we have chosen microemulsion droplets as model system, which can be tuned in size, shape and their interfacial tension over a wide range. They consist of a polar liquid such as water, a non-polar liquid such as an oil and a surfactant. By adjusting the appropriate concentration and temperature, a microemulsion (μE) forms discrete water/oil or oil/water aggregates, which are thermodynamically stable and can be used as a colloidal model system. In this study we avoid complications due to surface charge effects and use a non ionic surfactant.

We chose a system of water, n -alkanes and the non-ionic surfactant $C_{12}E_5$ at the water-rich side of the phase diagram. All measurements have been performed in the one-phase region between the upper near critical boundary (ncb) and the lower emulsification failure boundary (efb). The droplets have been characterized by Dynamic Light Scattering (DLS) and Small Angle Neutron Scattering (SANS). The results show that the shape varies strongly with temperature, from network like (close to the ncb) to elongated to spherical droplets at lower temperature close to the efb . The thermal diffusion behavior of the μE -droplets has been investigated by the *Infrared Thermal Diffusion Forced Rayleigh Scattering* technique. With this method we obtain the mass diffusion coefficient D , the thermal diffusion coefficient D_T and the Soret coefficient S_T . In a first study we used only n -decane as oil and investigated the behavior along three different paths. We varied the temperature between the ncb and the efb and could relate the results to the influence of the shape of the droplets. Close to the efb the results for low temperatures and thus spherical droplets are compared for different volume fractions of droplets and different oil content and thereby size. We found only a very small influence of the volume fraction below 10% on the thermodiffusion coefficients. The comparison of different sizes showed an increase of the Soret coefficient with radius but the measurement range was too small to differentiate between a linear and quadratic behavior. Additionally we compared our results with a model of *Parola* and *Piazza*, who proposed that the Soret coefficient depends linearly on the radius and on the temperature derivative of the product of the interfacial tension and some characteristic length l . This length is a measure for thickness of the interfacial layer, which is influenced by the temperature gradient. The interfacial tension measurements were conducted by the group of *Strey* at the University of Cologne. The results of the thermodiffusion measurements and the calculated values show fairly good agreement for spherical droplets. The drawback of this study was a shift in the efb temperature accompanied by increasing the oil content and thereby the size.

To access a wider parameter space for size and interfacial tension, we used different n -alkanes, so it was possible to measure different droplet sizes at the same temperature. Also, as before the micro emulsions were characterized by DLS and SANS measurements to obtain the structure and size close to the efb . The Soret coefficient increases linearly with the droplet radius for spherical particles. Furthermore we were able to extend the investigation of the thermodiffusion behavior in relation with interfacial tension. We determined the characteristic length l between 1 and 2 Å. Although we used different oils in our studies, we assumed that the droplets core does not influence the thermodiffusion behavior but only the shell and the interface interact with the surrounding. We found that for our sample system, the

interfacial tension dependence is dominated by the particle size due to a small derivative of the interfacial tension by temperature, which was proposed in the theory. Thereby we gave a first insight into this model applied to soft colloidal particles.

KURZZUSAMMENFASSUNG

Thermodiffusion oder Thermophorese tritt auf, wenn eine flüssige Mischung einem Temperaturgradienten ausgesetzt wird. Dies führt zur teilweisen Trennung der verschiedenen Komponenten. Es ist ein noch immer ungelöstes Nicht-Gleichgewichtsproblem in der physikalischen Chemie. Thermodiffusion kann für Stofftrennung in großem Maßstab und zur Polymercharakterisierung eingesetzt werden. Darüber hinaus wird das Phänomen mit dem Ursprung des Lebens in Tiefseeregionen in Verbindung gebracht, da dort starke Temperaturgradienten z.B. an heißen Quellen oder anderen vulkanischen Aktivitäten auftreten. Ein grundlegender Parameter ist der Soret Koeffizient, der als Quotient vom thermischen Diffusionskoeffizienten D_T und dem Massendiffusionskoeffizienten D definiert wird.

Trotz intensiver Forschung existiert immer noch kein mikroskopisches Verständnis der Thermodiffusion. Um den Ursprung der Thermodiffusion adäquat untersuchen zu können, ist es erforderlich, geeignete Modellsysteme und zuverlässige Methoden zu verwenden.

Die Modellsysteme müssen mit theoretischen Konzepten zugänglich sein und vereinfachte Geometrien wie Kugeln aufweisen. Zusätzlich sollte das Modell eine systematische Variation von Parametern wie Größe, Masse oder Ladung ermöglichen. Um auch seltene Materialien untersuchen zu können, ist ein kleines Probenvolumen wünschenswert. Ausserdem ist eine einfache Geometrie erforderlich, um diese theoretisch modellieren zu können. Darüber hinaus sollten Messungen berührungslos sein, um das Messsystem nicht zu stören, wie durch eine Probenentnahme. Diese Arbeit enthält beide Aspekte, die Entwicklung einer neuen experimentellen Methode und die systematische Untersuchung von Mikroemulsionsströpfchen, die als abstimmbare kolloidale Modellsysteme betrachtet werden können. Eine klassische experimentelle Methode ist die sogenannte Thermogravitations säule (TG). Sie wurde als eine der ersten Apparaturen zur Materialtrennung mit Thermodiffusion genutzt. Ein mit

einer TG durchgeführtes Experiment beruht auf der Probenentnahme und deren Konzentrationsbestimmung zur Bestimmung des Thermodiffusionskoeffizienten. Ein Hauptaspekt dieser Arbeit war die Entwicklung einer neuartigen TG, um sie mit einem optischen Detektionsverfahren kombinieren zu können. Dieses Projekt wurde in Zusammenarbeit mit der Gruppe von M. M. Bou- Ali an der Mondragon-Universität durchgeführt. Die Mikrothermogravitations säule (μ -TG) wurde für ein sehr kleines Probenvolumen zur Untersuchung sehr seltener oder teurer Proben, wie biologischen Systemen, konstruiert. Die Dimensionen sind so gewählt, dass sich ein parabolisches, laminares Strömungsfeld ausbildet, das eine große Auftrennung erreicht wird und um sicherzustellen, dass die Voraussetzungen für die theoretische Modellierung erfüllt sind. Die Säule besitzt eine Spaltbreite von nur rund $500\ \mu\text{m}$ und einer Höhe von $3\ \text{cm}$. Die Konzentrationsunterschiede zwischen zwei Punkten innerhalb der Probe werden berührungslos mithilfe einer interferometrischen Nachweismethode bestimmt. Diese optische Methode ermöglicht sehr hochaufgelöst und zeitaufgelöst zu Messen. Die Analyse des zeitabhängigen Konzentrationsprofils war noch nicht möglich, da die vorhandenen theoretischen Modelle eine unendlich kurze Schaltzeit des Temperaturgradienten annehmen, welche experimentell nicht erreicht werden kann. Die interferometrische Messmethode wurde im Vergleich zu einer kontinuierlichen Intensitätserfassung durch eine aktive Phasenkontrolle verbessert. Einer der Spiegel sitzt auf einem Piezoaktuator. Durch das Anlegen einer sinusförmigen Spannung verändert sich die Position des Spiegels, was zu einer bekannten Phasendifferenz führt. Dies ermöglicht eine zuverlässige Phasenbestimmung unabhängig Intensität des Lasers oder dem Kontrast des Interferenzmusters. Das System wurde durch Messungen der drei binären Benchmark-Mischungen und durch die Untersuchung der Mischung von Toluol und *n*-Hexan validiert. Die erhaltenen Ergebnisse stimmen innerhalb von 5% mit den Literaturwerten überein.

Zusätzlich wurden Messungen an Mikroemulsionen durchgeführt. Die Größe der Tröpfchen kann systematisch variiert werden und die Grenzflächenspannung lässt sich bestimmen. Die Größenabhängigkeit des Soret Koeffizienten wird kontrovers diskutiert. Theoretische Modelle kommen zu einer linearen, quadratischen oder sogar kubischen Abhängigkeit des Soret Koeffizienten vom Radius. Experimentell wurden sowohl lineare als auch quadratische Größenabhängigkeiten des Soret Koeffizienten für harte und weiche Kolloide gefunden. Zwei Studien an demselben kolloidalen System führten zu unterschiedlichen Ergebnissen. Ein Grund für diese Diskrepanz könnten die Oberflächeneigenschaften der untersuchten kolloidalen Systeme sein. Obwohl harte Kugeln mit verschiedenem Radius synthetisiert werden können, kann die

Oberflächenbeschaffenheit oder Ladungsdichte stark variieren. Die Phasenübergangstemperaturen für harte kolloidale Systeme aus verschiedenen Chargen können im Bereich von mehreren 10 K schwanken. Um diesen Nachteil zu umgehen, haben wir uns für Mikroemulsionströpfchen als Modellsystem entschieden, da die Tröpfchen in Größe, Form und deren Grenzflächenspannung über einen großen Bereich angepasst werden können. Sie bestehen aus einer polaren Flüssigkeit wie Wasser, einer nicht-polaren Flüssigkeit wie einem Öl und einem Tensid. Durch das Einstellen der geeigneten Konzentration und Temperatur bildet eine Mikroemulsion (μE) diskrete Wasser / Öl oder Öl / Wasser- Aggregate, die thermodynamisch stabil sind. In dieser Studie haben wir Komplikationen aufgrund von Oberflächenladungseffekten vermieden und verwenden dazu ein nicht-ionisches Tensid.

Wir haben ein System von Wasser, n -Alkanen und dem Tensid C_{12}E_5 an der wasserreichen Seite des Phasendiagramms untersucht. Zwischen der oberen Grenze in der Nähe der kritischen- (ncb) und der unteren Emulgationsgrenze (efb), findet sich ein Ein-Phasen-Bereich mit diskreten Aggregaten, die mit dynamischer Lichtstreuung (DLS) und Kleinwinkelneutronenstreuung (SANS) charakterisiert wurden. Die Ergebnisse zeigen, dass die Form stark mit der Temperatur variiert, vom Netzwerk (in der Nähe der ncb), über längliche, bis zu kugelförmigen Tröpfchen bei niedriger Temperatur in der Nähe der efb . Das Thermoeffusionsverhalten der μE -Tröpfchen wurde mithilfe der *Infrared-Thermal Diffusion Forced Rayleigh-Scattering* Methode untersucht. Mit dieser Methode erhalten wir den Massendiffusionskoeffizienten D , den thermischen Diffusionskoeffizienten D_T und den Soret Koeffizienten S_T . In einer ersten Studie verwendeten wir nur n -Dekane als Öl und untersuchten das Verhalten entlang von drei unterschiedlichen Pfaden. Wir variierten die Temperatur zwischen der ncb und dem efb und konnten den Soret Koeffizienten mit der Form der Tröpfchen in Verbindung bringen. Die Messungen bei niedrigen Temperaturen in der Nähe der efb an kugelförmigen Tröpfchen wurden für verschiedene Volumenanteile der Tropfen und dem Ölgehalt und damit der Größe verglichen. Wir fanden nur einen sehr geringen Einfluss des Volumenanteils unter 10% auf die Thermoeffusion. Der Vergleich der verschiedenen Größen zeigte einen Anstieg des Soret Koeffizienten mit dem Radius, aber der Meßbereich war zu klein um zwischen einem linearen und einem quadratischen Verhalten zu unterscheiden. Zusätzlich haben wir unsere Ergebnisse mit einem Modell von *Parola* und *Piazza* verglichen, die vorschlagen, dass die Soret Koeffizienten linear vom Radius und der Temperaturableitung des Produkts aus der Grenzflächenspannung und einer charakteristischen Länge l abhängen. Diese Länge ist ein Maß für die Dicke der Grenzflächenschicht, die durch den Temperaturgradienten beeinflusst wird. Die Messungen der Grenzflächenspannung wurden in der Gruppe

von *Strey* an der Universität zu Köln durchgeführt. Die Ergebnisse der Thermodiffusionsmessungen und die berechneten Werte zeigen recht gute Übereinstimmung für kugelförmige Tröpfchen. Der Nachteil dieser Studie war eine Verschiebung der *efb* Temperatur begleitet durch die Erhöhung des Ölgehaltes und damit der Größe der Tröpfchen.

Um einen größeren Parameterraum für die Größe und Grenzflächenspannung zu eröffnen, haben wir das System mit verschiedenen *n*-Alkanen untersucht. Dadurch war es möglich, verschiedene Tröpfchengrößen bei der gleichen Temperatur zu messen. Auch hierbei wurden die Mikroemulsionen durch DLS und SANS Messungen charakterisiert um die Struktur und Größen in der Nähe der *efb* zu bestimmen. Wir fanden dass der Soret Koeffizient linear mit dem Tropfenradius der sphärischen Teilchen ansteigt. Außerdem waren wir in der Lage, die Untersuchung des Thermodiffusionsverhaltens in Bezug auf die Grenzflächenspannung zu erweitern. Wir bestimmten die charakteristische Länge l im Bereich zwischen 1 und 2 Å. Obwohl wir in unseren Studien verschiedene Öle nutzten, haben wir angenommen, dass der Kern der Tröpfchen nicht das Thermodiffusionsverhalten beeinflusst, sondern nur die Hülle in Wechselwirkung mit der Umgebung steht. Wir fanden heraus, dass die Abhängigkeit von der Grenzflächenspannung für unsere Beispielsysteme durch die Tröpfchengröße dominiert wird, da die in der Theorie vorgeschlagene Ableitung der Grenzflächenspannung nach der Temperatur sehr klein ist. Dadurch haben wir einen ersten Einblick erhalten und dieses theoretische Modell erstmals auf weiche kolloidale Partikel angewendet.

CONTENTS

Titlepage	i
Abstract	iii
Kurzzusammenfassung	xi
Contents	xi
1 Introduction	1
1.1 Thermal diffusion	1
1.2 Application of thermal diffusion	2
1.3 Theoretical description of thermal diffusion	4
1.3.1 Introduction to theoretical concepts	4
1.3.2 Theoretical concepts regarding Colloids	5
1.4 Experimental thermal diffusion studies	6
1.4.1 Organic systems	7
1.4.2 Hard and soft colloids in aqueous systems	8
1.4.3 Microemulsions	9
2 Sample System	11
2.1 Molecular solutions	11
2.2 Characterization of the studied microemulsions	11
2.2.0.1 Ionic/Nonionic	11
2.2.0.2 Phase behavior	12

3	Methods	15
3.1	Measurement schemes	15
3.2	Introduction of methods	15
3.2.1	Comparison of other methods with TDFRS	15
3.2.2	Set-up TDFRS	19
3.2.3	Working principle	21
3.2.4	Contrast factors	24
3.2.4.1	Refractive index increment by concentration, $(\partial n/\partial c)_{p,T}$	24
3.2.4.2	Refractive index increment by temperature, $(\partial n/\partial T)_{p,c}$	26
4	Objectives of the work - Motivation	29
5	Micro-thermogravitational Column	31
5.1	Introduction	32
5.2	Experimental Setup	33
5.2.1	Materials	33
5.2.2	Design and construction of the TG micro-column	34
5.2.3	Design and construction of the interferometer	34
5.2.3.1	Interferometric measurement	36
5.2.3.2	Characterization of the cell	37
5.3	Theoretical approaches	37
5.3.1	Determination of the phase shift due to concentration	37
5.3.2	Determination of the concentration change	39
5.4	Numerical Simulations	40
5.4.1	Numerical validation of the TG micro-column	40
5.4.1.1	Simulation results	42
5.5	Results and discussion	43
5.6	Appendix	45
5.6.1	Characterization of the temperature switching	45
5.6.2	Stability and response of the interferometer	46
6	Soret Coefficient in Nonionic Microemulsions: Concentration and Structure Dependence	53
6.1	Introduction	54

6.2	Experimental details and characterization	57
6.2.1	Experimental details	57
6.2.1.1	Sample preparation	57
6.2.1.2	Refractive index increments	58
6.2.1.3	Dynamic light scattering	58
6.2.1.4	Small angle neutron scattering	59
6.2.1.5	Infrared-Thermal Diffusion Forced Rayleigh Scattering	59
6.2.2	Characterization of the microemulsion system	60
6.2.2.1	Phase behavior	60
6.2.2.2	Microstructure	61
6.3	Results	64
6.3.1	$path_T$: structure dependence	65
6.3.2	$path_{w_B}$: size dependence	65
6.3.3	$path_\phi$: volume fraction dependence	68
6.4	Discussion and Conclusion	70
6.4.1	Structure and shape	70
6.4.2	Interfacial tension	72
7	Isothermal Behavior of the Soret Effect in Nonionic Microemulsions: Size Variation by Using Different n-Alkanes	77
7.1	Introduction	78
7.1.1	Thermodiffusion	78
7.2	Experimental details and characterization	80
7.2.1	Experimental details	81
7.2.1.1	Sample preparation	81
7.2.1.2	Refractive index increments	81
7.2.1.3	Small angle neutron scattering	82
7.2.1.4	Dynamic light scattering	84
7.2.1.5	Infrared-Thermal Diffusion Forced Rayleigh Scattering	84
7.3	Results	85
7.3.1	Phase behavior	85
7.3.2	Microstructure	85
7.3.3	Thermodiffusion behavior	91
7.3.3.1	Temperature dependence	91

7.3.3.2	Size dependence	93
7.3.4	Interfacial tension	93
7.4	Discussion and Conclusion	99
7.5	Acknowledgments	100
8	Conclusion	101
8.1	Outlook	103
	Appendix	105
	Danksagung	107
	List of Figures	xv
	List of Tables	xxi
	Bibliography	xxiii
	Erklärung	xxxv

INTRODUCTION

1.1 Thermal diffusion

Thermal diffusion occurs in many transport processes in liquid mixtures of two or more components exposed to a temperature gradient. The result is a separation between the different species within the mixture. Discovered by Carl Ludwig [72] and later systematically investigated by Charles Soret [129–131], thermal diffusion is also known as Soret effect.

The mass flow J in a binary fluid mixture in a temperature gradient along one axis can be described by:

$$J = -\rho D \nabla c - \rho c(1 - c) D_T \nabla T \quad (1.1)$$

with the density ρ , the concentration of one species c , temperature T , the mass diffusion coefficient D , and the thermal diffusion coefficient, D_T . The first term describes Fick's law of diffusion, the second represents the thermal diffusion. The two processes oppose each other, while the thermal diffusion generates a concentration gradient, the Fickian diffusion homogenizes the mixture. For the stationary state with $J = 0$ and thus the Fickian diffusion just compensate the thermal diffusion, the Soret-coefficient is defined by $S_T = D_T/D$.

1.2 Application of thermal diffusion

Application of thermal diffusion can be found in many areas, such as separation techniques, analytical measurements or biological phenomena.

One of the first applications of thermal diffusion in history was the Manhattan Project by the US government. Already in 1939, the German scientists Clusius and Dickel [30] introduced a new method for isotope separation in gases, which was then used for the enrichment of the uranium isotope U-235 in uranium hexafluoride gas in the Manhattan Project. A large facility was built, using thermogravitational columns, containing an inner pipe of nickel and an outer, surrounding pipe of iron running vertically. The inner pipe contained hot steam, while the outer pipe was surrounded by water and the gap in between contained the uranium hexafluoride. These columns had an impressive height of around 15 m and were able to enrich the preprocessed gas from 0.71 % to 0.89%.

In the last years, thermal diffusion was used for characterization of polymers and colloids in solution, for example in the so-called Thermal-Field-Flow-Fractionation (TFFF) [28]. The basic setup consists of a thin "flow" channel with a laminar flow from an inlet to the outlet end. Over the length of this channel the separation is achieved by different basic phenomena: in a TFFF, the temperature gradient causes one or more species to leave the center of the flow channel and thus the region of large velocity and wander to either the warm or the cold wall, depending on the thermal behavior of the components. The species with the strongest reaction to the temperature gradient will accumulate on a wall and slow down, while an only weakly responding species will flow through the channel faster and is detected earlier at the outlet. By adjusting the channel properties like length and width and the flow speed, it was possible to analyze the samples, mainly polymer and colloidal solutions [71] [123] [28]. For low molecular weight mixtures, a high temperature gradient is required.

Nowadays, thermal diffusion is used in technologies for investigation of DNA [39], nucleotides [6], quantification of biomolecular binding reactions [7] and the transport of biomolecules in water, enriching or depleting in warm or cold regions. Studies of DNA and nucleotides also were used to argue for thermal diffusion playing a role in the origin of life, such as accumulating the basic building blocks of DNA in regions of temperature gradients in the early stage of earth, such as hydrothermal vents at the bottom of the ocean [6, 81].

The next step to the first life forms would be the formation of biological cell like structures containing DNA. Even if the formation of fatty acids and amphiphiles is occurring within or near hot vents or regions at the bottom of the ocean, [120] the accumulated concentration within a small volume would not be sufficient to create vesicles. *Budin* et al. [20] showed that the critical aggregate concentration can be achieved with a thermogravitational setup of micro capillaries, being similar to thin channels within the wall of a hot smoker.

Starting in the earth's core and crust, there are several works proposing a rather large influence of thermal diffusion on the formation of different solid structures. *Lundstrom* [76] uses thermal diffusion as an important factor in his hypothesis on the origin of granitoid, a widespread formation within the earth's structure and the preferred distribution of minerals within. Also a work of *Huang* et al. [50] discusses the role of thermal diffusion for the isotope fractionation in silicate melts, finding a Soret-coefficient unequal to zero and independent of composition and temperature.

Ascending further, through the deep sea regions and the origin of life scenario, to the oceans surface one encounters a very widespread large temperature gradient. The sunlight heats up the upper layers of the sea while deeper regions are much cooler, producing a vertical temperature gradient, like in a Soret-cell. A concentration gradient evolves with an accumulation of salt ions in deeper regions. This concentration imbalance should be reduced by Fickian diffusion. When the salt concentration is large enough, so called brines are formed, sheets of high salt amount. Between these brines and the sea water with depleted salt content, a jump in the density profile occurs. This jump hinders backdiffusion and thus remixing. Also the brines absorb more sunlight leading to larger temperatures below the surface [19] [23]. Making use of this phenomenon with Solar ponds, heat energy can be stored properly and used for heating or energy production [4, 116, 135].

Another biological reaction can be investigated with *NanoTemper*, a device based on thermal diffusion which can determine binding/reaction parameters of proteins/biomolecules and ligands. NanoTemper® uses the different thermal diffusion behavior of unbound proteins and proteins with a ligand attached to it, since the ligand changes the chemical/physical properties. Thereby, the thermal diffusion properties are changed and by measuring for different times or ligand concentrations, the binding parameters can be obtained. The biomolecules in aqueous solution are fluorescently labeled and inserted into a small capillary. An IR-laser illuminates the region of interest in the capillary and heats up the water. The biomolecules react to the temperature gradient from the center of the IR-spot and accumulate in or diffuse

away from the heated area. Thereby the fluorescence intensity changes with the concentration of the labeled molecules and can be analyzed to determine the transport coefficients.

1.3 Theoretical description of thermal diffusion

To understand the phenomenon and to be able to make predictions it is necessary to build a solid theoretical background.

1.3.1 Introduction to theoretical concepts

The theory by Chapman and Enskog [25, 41] is able to describe the thermodiffusion phenomenon for gaseous systems but failed to be expanded for liquid mixtures [108]. Only some basic principles such as the moment of inertia, mass and size of the particles can be used for many, but not all systems. The heavier and the larger particle in mixtures of species with similar masses are more likely to wander to the cold side.

Different approaches like lattice model calculations [74, 75], focussing on particle-particle and particle-solvent interactions and molecular dynamics (MD) simulations are used to understand the background behind thermal diffusion. The MD simulation includes equilibrium MD [124] simulations and synthetic/homogeneous non-equilibrium MD [77, 94, 96] simulations. Other attempts were done trying to connect thermal diffusion to a local pressure gradient at the particle solvent interface induced by the temperature gradient finding rather good agreement for a sample system of benzene cyclohexane mixtures [85] and toluene/*n*-hexane mixtures [125].

Many MD simulations of binary organic mixtures, like of two different alkanes, treat them as Lennard-Jones fluids with short range van-der-Waals interactions. Simulations describing molecules as single Lennard-Jones atom were able to give a correct trend but no qualitative description of the thermal diffusion behavior [117] [128]. The model was improved by using the united atom model to represent the chemical groups CH_2 and CH_3 by molecular atoms with a soft pair interaction term. [97]. With this approach and in combination with experiments it was possible to find the general trend mentioned above: The heavier, larger and stronger interacting species generally tend to accumulate at the cold side inside a temperature

gradient. The size effect on the other hand is still an open critical question in the community.

Molecular dynamics simulations for aqueous systems show an important role to the cross interaction between the different species [88]. By increasing the concentration of one strongly pair-interacting species at either the warm or cold region may lead to a lower total energy of the system, similar of cohesion forces, where surrounding particles act as a good solvent. Similar results are found for two-chamber lattice calculation by *Luettner-Strathmann* [74] and *de Gans* [32]. As one of these pair wise interactions works the formation and break up of hydrogen bonds. These bonds and their strength influences the energy landscape. Since these bonds are sensitive to temperature, ions and more, this leads to a complex behavior for different compositions and temperatures.

An even more complex situation occurs for mixtures of three different species. These mixtures can contain water and different salts or ions like *NaCl* solutions with charge effects dominating. Also ternary mixtures of water, surfactant and oils are of interest for thermodiffusion studies, where the formation of aggregates has large effect on the physical behavior.

1.3.2 Theoretical concepts regarding Colloids

In order to understand the thermodiffusive behavior of colloids, particles much larger than the surrounding small solvent molecules, the effect of a flow field around the particles and the interaction between the surface and the surrounding solvent need to be considered [34] [35]. In aqueous systems the electric-double-layer and dispersion forces play an important role. The electric-double-layer around a colloid is affected strongly by temperature and thus a temperature gradient over the particle dimension. Thermal diffusion of these ions around the particle leads to an excess hydrostatic pressure pushing the colloid.

The presence of another compound, such as polymers around a colloid will also affect and alter the thermal diffusion behavior due to depletion forces. After applying the temperature gradient, the concentration of polymers around the colloid will change, leading to a relative increase on the one side and a relative decrease on the other. This depletion force will act on the colloid, the region with increased polymer concentration acts with a larger pressure on the particle, while the region with less polymers acts with a smaller pressure on the particle. This effect is able to increase the thermal diffusion behavior or even to change the sign for

very strong depletion forces.

Obviously considering flow fields around a colloid as source of thermal diffusion, the shape or symmetry of the particle plays a great role. Looking at an asymmetric particle, like a stretched sphere, the strength of a thermally induced flow around the particle may differ due to different curvatures of the interface. Additionally, a nonuniform particle may feel a stronger or weaker temperature gradient depending if the long or short axis is parallel to the temperature gradient. For example, rod like aggregates like the fd-virus can be oriented parallel or vertical to the temperature gradient. This will cause different flow fields for each configuration. If the particles are arranged along one axis, like for concentrations high enough, this will alter the thermodiffusion behavior. Additionally the interaction length can be tuned by adjusting the ion concentration of the solvent and thereby the *Debye* length of the viruses. An experimental study by *Wang* [149] showed a sign change and an increase of the Soret coefficient for increasing *Debye* length, leading to particles with a smaller length to width ratio.

Temperature and a flow field around or close to the particle interface influence the particle differently depending if the shell is hard or soft. For hard shells, the particle shape will not change due to temperature or surrounding. Soft shells on the other hand, for example microemulsion droplets, are able to be deformed and thus alter the flow field around them. If the shell is made up of surfactant molecules for example, a flow field around the particle will induce a motion of these molecules and generate a second flow field inside the particle [158]. Soft particles also may react on the temperature gradient by deforming even without external flow fields but due to a change of the interfacial tension difference between the hot and the cold side. This effect forces the particle to the region of smaller interfacial tension [95].

1.4 Experimental thermal diffusion studies

In the last years, many thermodiffusive studies on a variety of sample systems with many different methods have been performed. In principle, the measurement principles used can be divided into two classes, with and without convection taking part in the separation process. To investigate the thermodiffusion behavior systematically, different sample systems with a

variety of interactions, charge, size, and mass have been used and will be described in the following. Due to the importance of the characterization of crude oil reservoirs, especially alkanes, organic one and two ring compounds have been investigated.

1.4.1 Organic systems

Organic compounds are used as model systems to search for correlations of the Soret-coefficient with physical properties like mass, size and so on. A fairly good working principle is the connection of the Soret-coefficient with the solubility which can be obtained with the *Hildebrandt* parameter δ , which is defined as $\delta = \sqrt{(\rho(\Delta H_v - RT))/M}$ [151] [159] with the density ρ , the gas constant R , enthalpy of vaporization H_v , temperature T and the molar mass M . This approach works well for liquids containing compounds which can be described with a Lennard-Jones fluid.

The *Hildebrandt* approach results in the crude rule of thumb stating the heavier and denser species wanders to the cold, which works fine for binary mixtures containing *Cis*-decalin, Cyclohexane and 2-methylbutane. *Polyakov* et al. [107] studied the thermodiffusion of binary mixtures containing the spherical molecules carbontetrachloride in addition of carbontetramide and the silanes tetraethylsilane and di-tert-butylsilane. He was able to achieve similar results for the experiment and MD simulations within a deviation of 10–20%. Also, the most asymmetric molecule di-tert-butylsilane accumulated stronger at the cold side, which was in agreement with the simulations. Another try to connect the thermodiffusive behavior with the moment of inertia was not able to give a clear statement but it seemed that the moment of inertia has to be split up into different contributions to fulfill the theory.

Sample systems which are still non-polar and without specific interactions but can not be mapped into a Lennard-Jones sphere already show deviations from this rule. Results for binary mixtures of Toluene, *n*-hexane and *n*-pentane show the largest value of S_T for the system with the largest difference of M and not δ .

Even increasing the asymmetry of the molecules as for 1,2,3,4-tetrahydronaphthalene, *n*-dodecane and Isobutylbenzene leads to a failure of the solubility approach, with the density as governing parameter. *Blanco* et al. [12] found a quantitative correlation of the thermodiffusion with the molecular weight, the viscosity and the thermal expansion coefficient investigating equimolar mixtures of linear alkanes and proposed the possibility to estimate

the thermal diffusion behavior of n -alkane mixtures with knowledge of these three parameters.

Investigation of the mass effect on thermal diffusion was carried out by measuring binary isotopic mixtures of the same species chlorobenzene, brombenzene and benzene [121]. The results lead to two contributions on the Soret effect, the normalized difference in mass $\delta M = (M_1 - M_2)/(M_1 + M_2)$ and the difference in inertia $\delta I = (I_1 - I_2)/(I_1 + I_2)$ as:

$$S_T = a_M \delta M + b_I \delta I. \quad (1.2)$$

Studies with benzene/cyclohexane mixtures [33] expanded the result with an finite Soret effect S_T^0 for different species, assuming same mass and moment of inertia for both. Therefore it may be called the chemical contribution.

1.4.2 Hard and soft colloids in aqueous systems

As already mentioned, the thermal diffusion behavior for organic systems with small interactions could be described and predicted in rather good agreement with experimental results [107]. In a strong contrast to the small and short interactions of organic mixtures are molecules and colloids within an aqueous surrounding. Colloidal hard spheres are usually charge stabilized to avoid aggregation into clusters. Due to the complex behavior of water with hydrogen bonds, dissociation into free ions and the generally polar molecule, the thermal diffusion behavior consists of several competing mechanisms. Tuning them individually, for example adding salt or changing the temperature, may lead to strong variations in the amplitude and even invert the sign of S_T . A strong influence was found for the *Debye* length [99] [39], pH [150], concentration [89], temperature [89] [61] and molecular weight. *Putnam and Cahill* [110] observed a sign change of S_T for charged latex beads in aqueous solution on adding salt at high pH values. *Piazza* and coworkers found the trend that negative sign of S_T for low temperatures in systems of polypeptides, SDS micelles [52] and DNA. For high polymers, D_T shows to be independent of molecular weight, but changes drastically by going to very short polymers and even become negative [24] [114] [136]. The temperature influences the solvent-solvent and solvent-solute interaction due to the hydrogen bonds of the water molecules. At low temperatures, more hydrogen bonds with stronger force are present while a higher temperatures these bonds break up and are less present.

The influence of the colloidal radius to its thermal diffusion behavior is yet still discussed. Although, the trends show an increase of S_T with the radius, the question for a linear or

quadratic dependence is still open. *Duhr and Braun* [38] found a quadratic size dependence for carboxyl-modified polystyrene beads (radius from 20 nm to 1000 nm) in 1 mM TRIS buffer. *Vigolo et al* [146] investigated the size dependence of S_T with a sample system of AOT/isooctane/water microemulsion droplets with a radius between 1.8 nm and 16 nm and they found a linear relation, lacking proof of the shape of the droplets at the measurement temperature. Also *Putnam and Cahill* [111] found a linear relation for charged nanoparticles, carboxyl functionalized polystyrene (PS) spheres and proteins of T4 bacteriophage lysozyme with radii between 13 and 46 nm. Repeating measurements with a similar system of the one used by *Duhr and Braun*, the results of *Braibanti et al.* showed a linear relation instead of the quadratic. They assumed the difference originates in the fact that they used density matched samples to avoid sedimentation and this altered the sample. A reason for these discrepancies could be the modification of the surface charge density by synthesizing particles of different sizes. Increasing the radius leads to a smaller charge density, changing the electrostatic contributions to thermal diffusion.

1.4.3 Microemulsions

To understand how different parameters like surface charge, size and interfacial tension influence the thermal diffusion properties of colloids, systematic experiments need to be performed. Considering hard colloidal particles, this becomes very difficult, since the charge density at the surface will vary for different batches. Therefore it is unlikely to have the same surface charge density for colloids of different diameter. In the case of hard colloids the interfacial tension is constant and can not be varied. To overcome these problems, soft colloidal micelles or microemulsion droplets can be used. In ternary mixtures consisting of two liquids, aqueous and organic (polar and nonpolar) and surfactant, an interfacial layer composed out of the amphiphilic surfactant molecules is formed around a core of the organic or aqueous liquid (non polar or polar). For example, the polar head group of the surfactant faces the polar water on the outside while solving oil in the core between the surfactant tails. Within a given temperature range, chemically and thermodynamically stable aggregates are formed. These aggregates are reproducible and self assemble, reducing the synthesis effort drastically. Thereby, no additional steric stabilization is needed. By variation of composition and temperature, one can tune the shape and size of these droplets, accessing a rather large parameter space [137] [56] [53] [134].

The role the interfacial tension plays for thermal diffusion is emphasized in different works in the literature [100] [98] [51]. For solid particles, the interfacial tension is difficult to

obtain. For soft, self assembled particles like microemulsion droplets however the interfacial tension is an rather easy accessible parameter and can even be tuned by temperature and composition. [134] [58] [133]. The particle would favor the region where it has a lower interfacial tension, thus the systems energy could be decreased. For a particle within a temperature gradient and thus with a change of the interfacial tension over the diameter, the so called *Marangoni* effect is assumed, inducing a flow of the solvent around the particle to compensate for the interfacial tension difference. Also the size and the shape of the droplets plays a large role for the interfacial tension, since the curvature varies strongly with the two parameters and the curvature is directly connected with the interfacial tension. [54]

SAMPLE SYSTEM

2.1 Molecular solutions

As mentioned above to some extent, the thermal diffusion of some non polar molecular binary mixtures can be described by empirical correlations and some predictions based on the mass, moment of inertia and heats of transport can be made. For evaluation and comparison of different methods it is necessary to have reliable data for the chosen system, therefore a benchmark was initiated to compare different experimental methods by studying the same mixtures. It was agreed on the investigation of the three binary mixtures of 1,2,3,4-tetrahydronaphtalene, isobutylbenzene and *n*-dodecane. Five different groups using different techniques measured the thermal diffusion properties of these binary mixtures at 50%wt [101] [15] [31] [107]. All new developed methods need to be validated for these three benchmark mixtures. Additionally the thermal diffusion data of the mixture of toluene and *n*-hexane are often used as reference.

2.2 Characterization of the studied microemulsions

2.2.0.1 Ionic/Nonionic

Before the thermal diffusion of ternary microemulsion systems was studied, binary water/surfactant mixtures were investigated. Early studies concentrated on ionic [98] [99] [68]

[141] and mixtures of ionic surfactants and nonionic surfactants [52] in a wide concentration range. The basic results stated that in the lower concentration range the *Debye – Hckel* theory plays a governing role and for larger concentrations the electrostatic inter particle interactions dominate the behavior.

Nonionic surfactant mixtures were only barely investigated [92] [93]. One reason might have been the difficulty of a smaller surfactant density than water, leading to strong convection effects. Therefore a non convective measurement method is necessary, like the TDFRS-Setup, described later on. *Ning* et al. performed measurements of non-ionic surfactant in water and added a dye to the sample to gain enough energy conversion of the blue laser (480nm) which was used in previous studies on organic solvents. This dye however seemed to change the chemical properties and thus alter the thermal diffusion behavior [90]. Recently, *Arlt* et al. [5] used a modified setup [154] with an infrared laser being absorbed by the water in sufficient quantity to measure aqueous solutions without dye.

2.2.0.2 Phase behavior

As already mentioned, microemulsions consist of a ternary mixture of for example water (A), oil (B) and surfactant (C). The two species A and B are generally immiscible and form a flat interface with the oil on top of the water. Adding a surfactant yields a rich phase behavior of the ternary system with a large variety of micro structures and strong dependency on temperature. The phase behavior of the ternary system water-oil-nonionic surfactant is related to the interplay of the different binary systems water-oil, water-surfactant and oil-surfactant. Many studies on the phase behavior of nonionic microemulsions have been carried out in the past [56] [134] [133] [138]. The phase behavior must be investigated in the whole parameter space defined by the content of water, oil, surfactant and by the temperature. The resulting phase diagram can be illustrated in the so called phase prism.

The phase prism can be cut in directions of constant values of A, B and C giving individual sections. For example the $T(w_B)$ section, with constant surfactant mass fraction γ_a or the isothermal cut horizontally through the face prism. The terms w_B and γ_a are defined as follows with indices A referring to water, B referring to oil and C referring to surfactant:

$$\gamma_a = \frac{m_C}{m_C + m_A} \quad \text{and} \quad w_B = \frac{m_B}{m_A + m_B + m_C} \quad (2.1)$$

The one phase region with stable aggregates is of special interest for thermal diffusion studies.

This region is defined by two phase boundaries at lower (emulsification failure boundary (efb)) and higher temperatures (near critical boundary (ncb)).

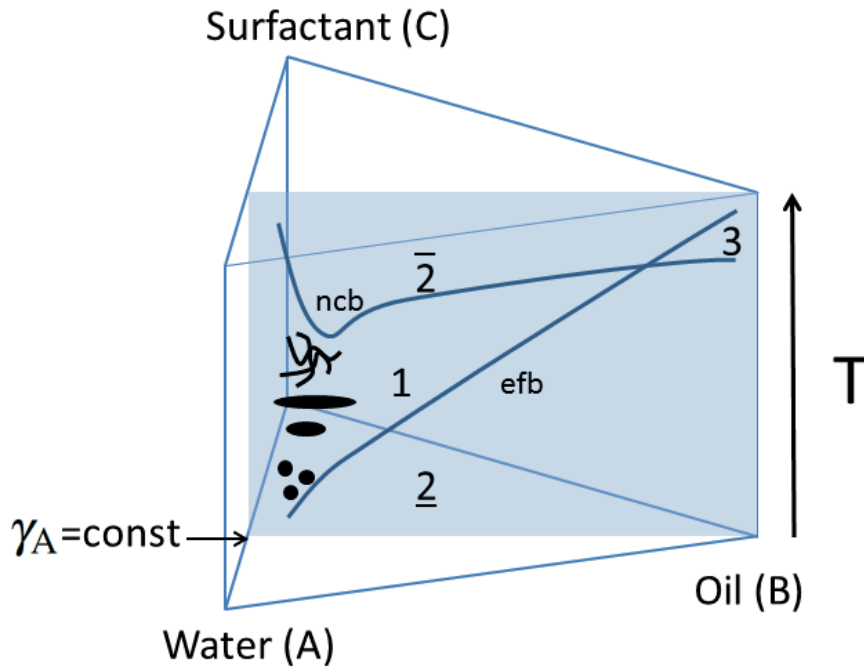


Figure 2.1: A cut through the phase prism along a fixed surfactant concentration γ_a . The two lines represent the phase transition temperatures along the axis of oil content w_B . With increasing temperature, the aggregates change from spherical droplets at the efb to elongated structures for intermediate temperatures and end up in network like structures at the ncb before phase separation occurs. The numbers indicate the phase regions with the upper and lower two phase regions marked with over and underlined numbers.

Since the studied non ionic microemulsions show a broad phase behavior and their size, shape, concentration and even interfacial tension can be varied, it is necessary to characterize the shape and size of the microemulsion droplets. As mentioned before we study the microemulsion droplets in the so-called one-phase region. To determine the size of the droplets, Dynamic Light Scattering (DLS) is used which measures the temporal fluctuations of the scattering intensity. The analysis of the intensity auto correlation function is in the simplest case monoexponential and gives the diffusion constant. Under the assumption of a spherical particle a hydrodynamic radius can be determined. DLS measurements of the microemulsion system show the following trend: Close to the efb, the radius changes only slightly with temperature. Increasing the temperature, an exponential increase of the radius close to the ncb is found. To verify the shape of the droplets, Small Angle Neutron Scattering (SANS) experiments are performed. In the SANS experiments we used deuterated

alkanes to change the contrast so that the thickness of the interfacial surfactant layer could be determined.

It is necessary to use an appropriate fitting model to analyze the data, which is briefly described in chapter 7. Further details can be obtained in ref. [43]. The determination of the phase transition borders was conducted by shining bright light through the samples in glass tubes within a thermostated water bath. To keep the samples homogeneous, a stirring bar was placed in the glass tube. The phase transitions could be identified by probing the turbidity of the sample. While the system is phase separated, the oil is forming rather large droplets which can not be solved anymore by the surfactant molecules. These oil droplets cause the sample to be turbid. On approaching the phase borders, the oil can be emulsified by the surfactant molecules, forming very small aggregates, leading to a clear sample. This process happens rather instantly in both directions for the upper phase boundary, crossing the ncb temperature from below or above. Approaching the lower phase transition temperature at the efb from below, the emulsification process finishes within minutes. By approaching and crossing the efb slowly from above, the system is meta stable for minutes up to a few hours, depending on the composition. That is because the phase boundary is kinetically hindered, meaning that the oil within microemulsion droplets is deprived on collision of different droplets. Thereby the systems could be investigated for temperatures even below the efb in further measurements.

To measure the interfacial tensions of the different systems, the so called "spinning-drop" method is used. The spinning-drop tension meter consists of a horizontally placed glass capillary rotating around its long axis. Based on a theory of *B. Vonnegut* [148], the shape of the drop formed inside the capillary at high angular velocities can be related to the interfacial tension. In the special case, the glass capillary had to be thermostated to avoid phase separation. Further details about the method can be found in ref. [133].

3.1 Measurement schemes

Thermal diffusion can be studied with different setups generating a temperature gradient, which must not cause nonlinearities in convection and being able to detect a resulting change in concentration.

The experimental configurations can be divided in four groups, as sketched in Fig.:3.1: A small, vertical temperature gradient without convection (a), a radial temperature gradient without convection (b), a small horizontal temperature gradient without convection and a larger horizontal temperature gradient with convection coupling (c).

3.2 Introduction of methods

3.2.1 Comparison of other methods with TDFRS

The Soret-cell is a setup of the first type. Two thermostated walls at the top and the bottom generate the temperature gradient while the side walls are made of material with low heat conductivity to minimize the heat transfer with the surrounding. To avoid free convection, the upper wall is heated and the lower wall is cooled. To measure the separation,

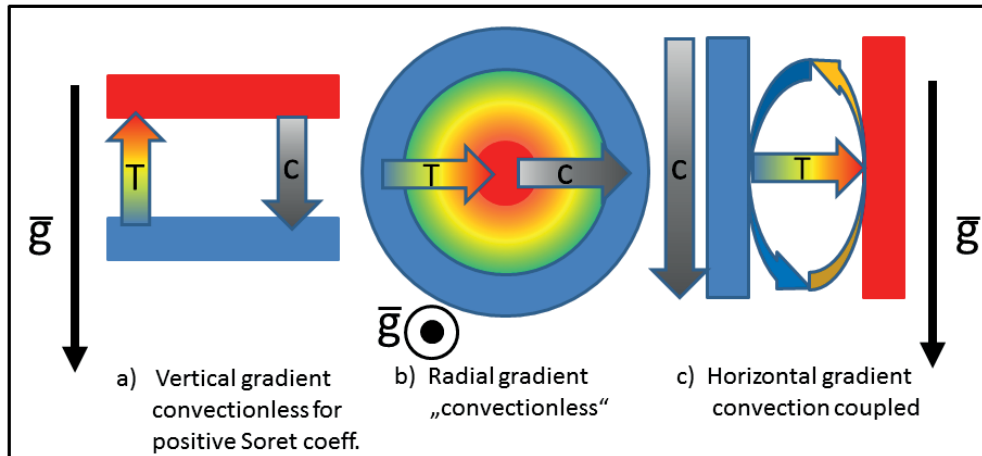


Figure 3.1: Different basic principles of thermodiffusion measurements. Type a) is the basis of a beam deflection or also called Soret-cell. It is heated from above to avoid convection. The concentration gradient (grey arrow marked with c) due to thermodiffusion occurs parallel to the temperature gradients (colored arrow marked with T) axis. Type b) shows the principle of a thermal lens. This temperature profile is created by irradiating a thin transparent cell with a gaussian laser beam being absorbed by the sample. Due to the gaussian intensity profile of the beam, the center is heated stronger than the outer regions, leading to a radial temperature gradient which is followed by a radial concentration gradient. This concentration gradient can be probed by investigating the strength of refraction similar to a thin or thick glass lens. Type c) shows the principle where thermodiffusion is coupled with convection. The horizontal temperature gradient causes a mixture to separate horizontally. The buoyancy due to thermal expansion at the warm/cold side causes the individual species to ascend/descend, respectively. This principle relies on the lighter species going to the warm side. For the opposite case, instabilities are generated leading to complex separation profiles. This type is used in thermogravitational columns

sample volume is extracted at different heights and analyzed separately. Another version of a Soret-cell is used for the so called *Beam Deflection* method (BD). Here, two opposite sidewalls are made of transparent material with good optical properties, such as low surface roughness and good flatness. Through these walls, a laser beam passes the sample at a defined height. Without a concentration gradient corresponding to a homogeneous refractive index, the laser will pass the sample without being deflected. For a vertical temperature and concentration gradient, the laser beam will be deflected to the region with higher refractive index. The deflection angle depends on the length of the sample cell and the changes in index of refraction with temperature and concentration. The deflection can be analyzed using a position detector at a fixed distance. The so called refractive index *contrast factors* with

temperature $(\partial n/\partial T)_{p,c}$ and concentration $(\partial n/\partial c)_{p,T}$ have to be measured independently. The total gradient of the refractive index n is given by:

$$\nabla n = \nabla T \cdot \left(\frac{\partial n}{\partial T} \right)_{p,c} + \nabla c \cdot \left(\frac{\partial n}{\partial c} \right)_{p,T} \quad (3.1)$$

∇n is extracted from the beam deflection and with known contrast factors and temperature gradient, ∇c can be calculated. Afterwards, the thermal diffusion coefficient can be obtained [65].

Another setup scheme works with a radial temperature gradient without convection, if the cell is thin enough and if the gravity field is perpendicular to the temperature gradient, which is called the *Thermal Lens* method. Like the *Beam Deflection*, this method makes use of the change in refractive index by changes in temperature and concentration. Usually, the generation of the thermal gradient and the optical measurement are done by only one laser beam. Choosing the wavelength to gain a sufficient absorption within the sample will lead to local heating by the laser light. Due to the gaussian laser intensity profile the highest temperature is reached in the center of the beam and decays radially. Due to a negative $(\partial n/\partial T)_{p,c}$ factor, a concave thermal lens is formed [119] [106]. The following concentration gradient based on the thermal diffusion will either enhance or decrease this effect. Thereby the focussing effect of the sample will change over time and can be evaluated to achieve the concentration profile for known contrast factors and thereby the thermal diffusion coefficient can be calculated. Compared with the *Beam Deflection* method, the thermal lens usually achieves much shorter equilibration times due to the small dimensions of a strongly focused laser in contrast to the rather thick cells of the BD. Some results though showed significant deviation for benchmark systems in the *Thermal lens* systems. *Luo et al.* and *Tabiryan et al.* [37] [140] investigated strongly absorbing ferrofluids, observing a bleaching effect. This bleaching was connected with the depletion of absorbing particles due to the Soret motion, leading to a temporal change in the temperature profile. *Hoffmann* and *Köhler* developed an analytical expression to correct for this effect, bringing the results in better agreement with results of the same sample system in a thermogravitational column [147].

A horizontal temperature gradient is applied within the so called *Thermal diffusion forced Rayleigh scattering* (TDFRS) method sketched in Fig. 3.2. Two laser beams are crossed and thereby brought to interference within the sample volume. The interference generates

an intensity grating in the vertical plane with periodic regions of high and low intensity. Similar to the *Thermal Lens* method, the laser wavelength is chosen to be absorbed by the sample, generating a horizontally periodic temperature gradient. This temperature difference is chosen so small, that convection is avoided during the measurement. The temperature grating leads to a refractive index grating and when thermal diffusion occurs it also leads to a concentration grating which enhances or decreases the refractive index grating. This refractive index grating is probed by a read out beam with a different wavelength to avoid absorption. The beam is diffracted, proportional to the strength of the refractive index gradients. By the analysis of the diffracted light and known contrast factors, the thermal diffusion properties can be obtained. The measurement times vary between a few milliseconds up to 30 seconds. The laser wavelength and the intersection angle between the two writing beams is chosen such as the fringe spacing is around $20 \mu m$.

The thermogravitational column is a method which combines the thermal diffusion due to a horizontal temperature gradient and convection. The temperature gradient leads to a horizontal concentration gradient. For mixtures where the denser species wanders to the cold side, it will sink down due to gravity and when the lighter species wanders to the warm side the buoyancy will drive it upwards, generating a vertical concentration gradient. Partially the convection leads also to remixing. It is very difficult to measure negative Soret coefficients, where the denser species wanders to the warm side. In that case, the two processes of convection and thermal diffusion work against each other. Under the assumption of linear velocity profiles, the separation process can be described by the Furry-Jones-Onsager theory [45]. Like for all the other methods, the separation due to the Soret effect is counterbalanced by regular diffusion until an equilibrium is reached. To measure the concentration profile and determine the thermal diffusion coefficient, samples at different heights are extracted and analyzed separately. By combination of thermal diffusion and convection, the total separation can be increased compared to a Soret cell, though an important drawback of this method is the lack of time resolved measurements. Extracting sample volume during the separation process will influence the results due to disturbances of the flow profile.

An improvement of the thermogravitational column (TG) are time resolved high precision measurements of the vertical concentration difference and thereby the thermal diffusion coefficient D_T . The aim was to combine the proven principle of the TG with an optical measurement similar to other methods relying on the contrast factor $(\partial n / \partial c)_{p,T}$. One approach is an interferometrical measurement of the optical properties of the sample inside the TG.

Table 3.1: Overview of different measurement setups used in thermal diffusion studies

Method	Measured quantities	Sample Amount /ml	Equil. time τ_{eq}/s	Auxiliary quantities	Operational effort/costs
Beam deflection	S_T, D_T D	0.5	1000	$(\partial n/\partial c)_{p,T}$ $(\partial n/\partial c)_{p,c}$	low
Thermal lens	S_T, D_T D	0.3	100	$(\partial n/\partial c)_{p,T}$ $(\partial n/\partial c)_{p,c}$	low
TDFRS	S_T, D_T	0.06	0.03	$(\partial n/\partial c)_{p,T}$	high
IR-TDFRS	D			$(\partial n/\partial c)_{p,c}$	high
				determination of conc.	medium
TG-column	D_T	10	10^5		
μ TG-column	D_T	0.05	1800	$(\partial n/\partial c)_{p,T}$	low

Taking the basic theory for TGs by Furry, Jones and Onsager into account and to keep the sensitivity to fluctuations of an interferometric device small, a compact size of the TG was chosen. To achieve short equilibration times, the gap width was with $500 \mu\text{m}$ thinner than regular columns but could still be produced in a machine shop with good manufacturing tolerance of $5 \mu\text{m}$. For optical access the cold and the warm walls have to be transparent for the laser. In a first experimental study [87], the chosen gap width of $500 \mu\text{m}$ lead to the name 'Thermogravitational micro column' or μ -TG. The measurement principle relies on the phase difference between two laser beams, which pass the cell at different heights. This procedure is described in further detail in chapter 5.

A comparison of different methods is shown in Table 3.1.

3.2.2 Set-up TDFRS

For most studies in this work, an infrared thermal diffusion forced Rayleigh scattering (IR-TDFRS) setup is used. The basic principle of a TDFRS is to generate a vertical intensity and thereby temperature grating inside the sample volume by interference of two laser beams. This is technically realized by splitting up one laser beam up into two beams which intersect inside the sample cell. Fig. 3.2 shows a sketch of the setup used. Two different lasers are used, a writing laser for the grating and a read out laser for the signal detection. The writing lasers wavelength has to be absorbed by the sample and as we use aqueous systems, we chose an infrared laser with a wavelength of 980 nm . The dashed line in the picture marks a thermally insulated box. A beam splitter cube separates the beam into two beams of similar intensity. One beam is reflected by a mirror mounted on a piezo, passes a

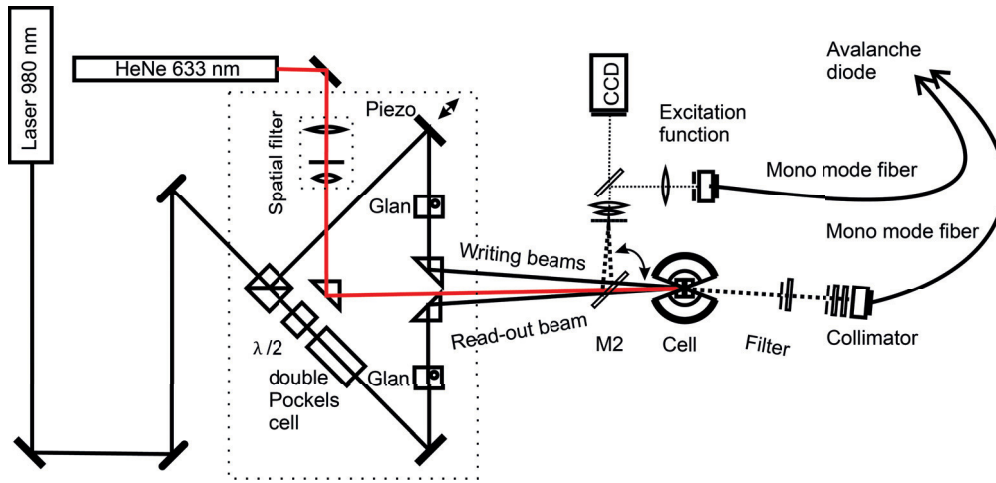


Figure 3.2: This picture shows a sketch of the (IR)TDFRS setup used in this work. The dotted line represents a thermally insulating box to reduce thermal fluctuations of the optical parts.

Glan-Thompson polarizer which polarizes the light vertically. Note that the beam should be vertically polarized leaving the laser or the polarization has to be rotated to achieve sufficient transmission intensity. Afterwards, the beam is reflected by a prism and directed to the sample cell.

The other beam is going through a $\lambda/2$ plate, which rotates its polarization by 90° . Afterwards it passes a double *Pockels* cell (Leysop, England) which is connected to a high voltage driver operating at around 1.5 kV, controlled by a measurement software. This *Pockels* cell rotates the polarization of the beam by plus and minus 90° so that it is vertically polarized at $+180^\circ$ or -180° , so that the phase of the two states is shifted by $\pi/2$. After the *Pockels* cell the beam is repolarized by a *Glan-Thompson* prism and then reflected by another prism into the sample cell where the two beams interfere. Because of the limited coherence length of the writing laser, the paths of both beams have to be adjusted to be the same optical path length. The infrared light trespassing the sample cell is then blocked by a special filter. The wavelength of the read out beam can be any arbitrary but sufficiently different from the writing beam so that it is not absorbed by the sample. In this setup we use a Helium-Neon laser with a wavelength of 633 nm. The beam is lead through a spatial filter and is reflected into the sample by another prism. The incident angle in respect to the writing beams has to be adjusted to fulfill the *Bragg* condition. The transmitted beam is blocked after the cell and only the diffracted light is collected by a collimator and an optical fiber guides the light

to a photo diode.

In order to determine the grating vector and the finite switching times of the *Pockels* cell, the so called *Excitation function* is measured by reflecting a small fraction ($< 10\%$) of the light by mirror (M2), positioned in front of the sample cell. The two reflected beams interfere at a reticle in front of a microscope objective. The reticle is placed exactly at the same distance from the mirror as the sample cell. The interference grating gets optically magnified and the light field is almost made parallel at the exit of the objective. The magnified light grating and the magnified reticle are mapped by the camera. Another partially reflecting mirror (M3) is placed behind the objective which reflects approximately 10% of the light to a fiber coupler connected with another avalanche diode. In the setup we use a grey filter for M3, which avoids ghost images on the camera due to internal reflections within the glass.

The sample cell is fixed in a custom built cell-holder which is thermostated with a stability of 0.1 K by an external thermostat. The temperature is measured inside the holder by a PT100 temperature sensor and the thermostat can be controlled by the measurement software.

3.2.3 Working principle

The basic principle of the system is to measure the heterodyne diffraction intensity of the read out beam. The two writing beams form an intensity grating with a grating vector q_w of

$$q_w = \frac{4\pi}{\lambda_w} \sin \frac{\Theta_w}{2} \quad (3.2)$$

with the writing lasers wavelength λ_w and the angle Θ_w in between the two beams. The bisecting line of the angle should be perpendicular to the cell surface.

This intensity grating is converted into a temperature grating by absorption in the sample volume. Due to a change in refractive index by temperature $\partial n / \partial T > 0$, a refractive index grating with the same q is generated. The read out beam is diffracted by this grating. To achieve the maximal diffraction intensity the read out laser beam must fulfill the *Bragg* condition in the way that

$$q_w = q_r = \frac{4\pi}{\lambda_r} \sin \frac{\Theta_r}{2} \quad (3.3)$$

holds. The index r refers to the read-out beam. For the He-Ne laser with a smaller wavelength than the IR-Laser the angle Θ_r is smaller than Θ_w , therefore the beam passes between

the two deflecting prisms. The detector is positioned at the diffraction angle of the first maximum to obtain only the diffracted but not the transmitted light.

The absorbed laser light induces a temperature grating. This leads to a periodic change in refractive index proportional to $(\partial n/\partial T)$ which forms a refractive index grating. The temperature grating also induces thermal diffusion, which leads to another change in the periodic refractive index grating.

When thermal diffusion occurs, the different components diffuse either to the cold or to the warm side, altering the refractive index distribution. The refractive index contrast factor $(\partial n/\partial c)$ measures the change in refractive index with concentration. For samples where the component with the higher refractive index diffuses to the cold side, the amplitude of the diffraction grating increases and for samples with the opposite trend, the amplitude of the grating decreases. Accordingly, the diffraction intensity increases or decreases, respectively. The two processes, the temperature and concentration grating, follow two significant different time regimes, with a very short equilibration time of around a few hundred μs for the temperature and usually a few ms for the concentration grating. Thus, the two resulting diffraction signals can be differentiated very well.

The intensity I at the detector consists of different contributions of electric fields, the diffracted E_d , the coherent E_c and the incoherent E_{inc} . They sum up to

$$I = |E_c + E_d e^{i\phi}|^2 + E_{inc}^2 = E_d^2 + 2E_c E_d \cos(\phi) + E_c^2 + E_{inc}^2 \quad (3.4)$$

containing the *homodyne* intensity $I_{homo} = E_d^2$, the *heterodyne* intensity $I_{het} = 2E_c E_d \cos(\phi)$ with the phase shift ϕ and the background intensity $I_b = E_c^2 + E_{inc}^2$. The coherent background intensity is generated by fixed inhomogeneities in the sample cell or scratches or dust sitting at the windows of the sample cell.

In order to obtain the heterodyne signal, which is less susceptible to distortions, one has to differentiate it from the homodyne part. This can be done by applying a phase shift of π with the *Pockels* cell to one of the two beams and by recording the intensities for both states, I_ϕ and $I_{\phi+\pi}$, we get

$$I_{\phi+\pi} = |E_d e^{i(\phi+\pi)} + E_c|^2 + E_{inc}^2 \quad I_\phi = |E_d e^{i\phi} + E_c|^2 + E_{inc}^2 \quad (3.5)$$

This can be split up into the homodyne part ξ_{homo} and the heterodyne part ξ_{het} as

$$\xi_{homo} = \frac{1}{2}(I_\phi + I_{\phi+\pi}) - I_b \quad \xi_{het} = \frac{1}{2}(I_\phi - I_{\phi+\pi}) \quad (3.6)$$

To improve the stability of the coherent background, the piezo mounted mirror is used to correct the phase and keep it constant. For very long measurement times of above 10 s, with slow drifts of the phase, this drift has to be measured by the camera and then it is corrected by the piezo mirror.

To evaluate the measured signal properly, one needs to measure also the excitation function which records the finite switching time of the *Pockels* cell. This is done by projecting the optical grating on an avalanche diode before it passes the sample cell.

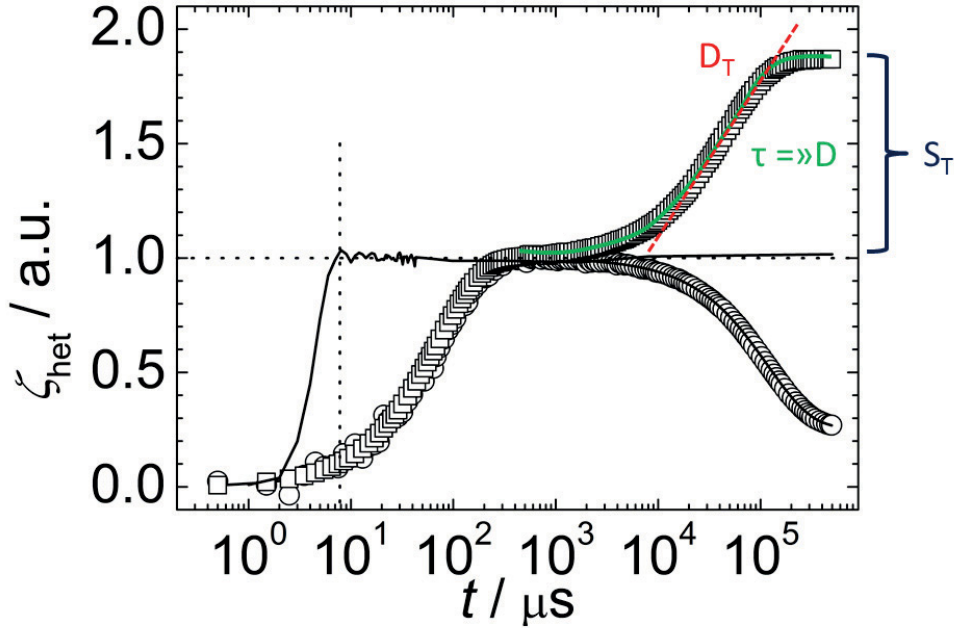


Figure 3.3: The normalized heterodyne intensity signal in the IR-TDFRS setup versus time. The sample is C_7G_1/H_2O with $w = 0.069 wt$ at $20^\circ C$ (circles) and $60^\circ C$ (squares). The horizontal dotted line is a guide to the eyes and marks the normalized thermal plateau. The excitation function (solid line) reaches the plateau after 8 ms (vertical dotted line). (Picture taken from B. Arlt.)

A typical result of a measurement is shown in Fig. 3.3, with the heterodyne intensity plotted

versus time on a logarithmic scale. The intensity reaches fast the thermal plateau and after some time it increases further until it reaches the concentration plateau. This is the case for a sample where the optically denser component accumulates in the cold regions. In the other case, the optical contrast of the grating decreases so that the concentration plateau lies below the thermal plateau. The Soret, thermal and mass diffusion coefficient can be determined from the normalized heterodyne diffraction signal.

$$\xi_{het}(t) = (1 - e^{-\frac{t}{t_h}}) - \frac{A}{\tau_c - \tau_{th}} [\tau_c(1 - e^{-\frac{t}{\tau_c}}) - \tau_{th}(1 - e^{-\frac{t}{t_h}})] \quad (3.7)$$

The thermal relaxation time of the grating is denoted as τ_{th} , the concentration relaxation time with τ_c and c is the concentration of one species in equilibrium. The amplitude A of the concentration signal can be described by

$$A = \left(\frac{\partial n}{\partial c} \right)_{p,T} \left(\frac{\partial n}{\partial T} \right)_{p,c}^{-1} c(1-c)S_T \quad (3.8)$$

and allows the calculation of the Soret coefficient when contrast factors and concentration are known.

The mass diffusion coefficient can be easily calculated from the relaxation time of the concentration signal and the grating vector.

$$D = \frac{1}{(\tau_c q^2)} \quad (3.9)$$

3.2.4 Contrast factors

The contrast factors are required in most optical measurement systems and even for sample analysis in regard to concentration as mentioned for thermogravitational columns. These contrast factors, the refractive index increments by concentration and temperature need to be determined additionally for each sample and probing wavelength.

3.2.4.1 Refractive index increment by concentration, $(\partial n / \partial c)_{p,T}$

The underlying effect of thermodiffusion is the separation of mixtures or the accumulation of particles in a solvent. This separation or accumulation leads to a local change in the optical properties of the probed sample. The refractive index will influence the optical path

length/phase through a sample, important for interferometrical methods, as described in chapter 5, or will generate diffraction in the TDFRS. From measuring the optical path/phase or the diffracted intensities, one can conclude to the local change in refractive index. Generally, this change comes from a local change in temperature and concentration. Due to the different time scales, one can distinguish these processes in most cases. The obtained change in refractive index due to concentration can then be processed with the refractive index increment by concentration $(\partial n/\partial c)_{p,T}$ to calculate the change in concentration, which usually is the parameter of interest. To measure these refractive index increments, we use an Abbe-refractometer, which uses total internal reflection as working principle. A flat glass window is illuminated from the bottom with light of a known wavelength. This light will be totally reflected at the window-air interface for the critical angle Θ_c which is defined as $\Theta_c = \arcsin(n_2/n_1)$ with the refractive indices n_1 of the glass and n_2 of the medium on top of the glass. The device is programmed to change the incident angle of the light source to achieve total reflection at the glass-medium interface. On applying a medium on the glass, the critical angle changes and by internal alignment inside the refractometer, the refractive index of the applied medium can be determined. By preparing samples of different concentrations in a range around the concentration of interest and measuring the refractive indices, we can determine the refractive index increment by concentration.

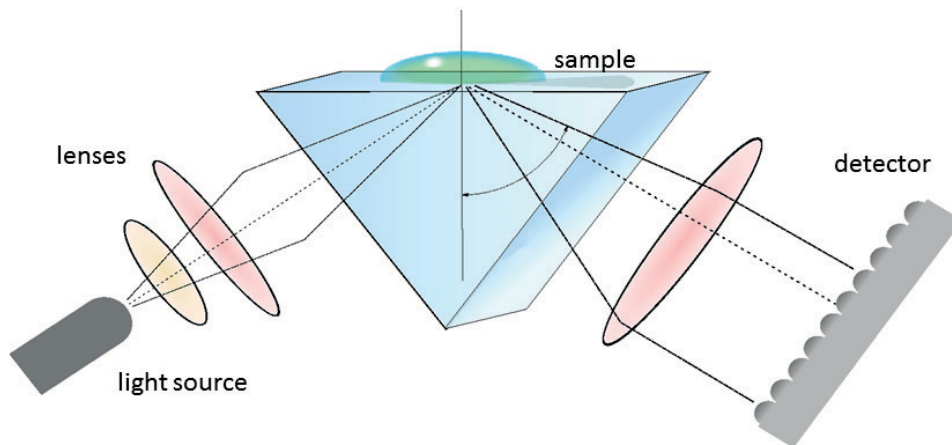


Figure 3.4: Working principle of the Abbe refractometer. The sample volume is applied onto the prism, leading to a change in the angle of total internal reflection. The light source and the lenses are adjusted to find the maximum intensity measured at the detector which also records the position of the detected light. This change of position is used to calculate the refractive index of the sample on top of the prism.

3.2.4.2 Refractive index increment by temperature, $(\partial n/\partial T)_{p,c}$

For different measurement techniques and also the (IR-)TDFRS the knowledge of the temperature effect on the refractive index is necessary. In the IR-TDFRS setup, the intensity grating leads to a temperature grating by absorption. This temperature grating is diffracting the light due to the different refractive indices between warm and cold regions, the larger the difference, the more light is diffracted. For signal evaluation and determination of the Soret coefficient it is required to know the increment of refractive index by temperature.

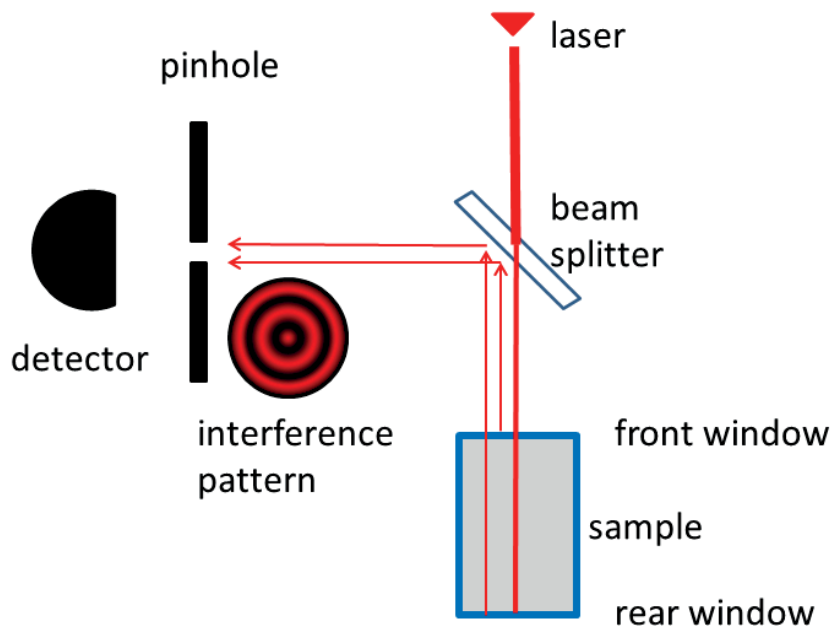


Figure 3.5: Schematic setup of the interferometer used to determine the refractive index increment by temperature. A laser beam is passing a beam splitter, where the reflected light is blocked by a wall. The passing light hits the sample cell, where part of the light is reflected at the front window and part is penetrating the sample volume and being reflected by the rear window. The light passing through the window is again blocked by a wall. The two reflections hit the beam splitter and are guided onto a pinhole. Due to interference of the two reflected beams, a fringe pattern can be observed. By adjusting the pinholes size to one fringe spacing, the detector achieves a large contrast. The temperature of the sample is ramped linearly, leading to a change in refractive index of the sample which causes a phase shift of the beam penetrating the sample. This phase shift can be recorded by analyzing the time dependent interference pattern.

To measure this increment, we use an interferometrical method relying on the change of the optical path due to a change in refractive index. A laser beam passes a beam splitter where a part of the beam is reflected into a wall and the other part is passing through to

the measurement cell made of glass. It is reflected from the front window and from the back window after passing the sample volume twice. These two beams hit the beam splitter and are reflected onto a pinhole after which the photodiode is positioned. The light of the two beams interferes and forms *Newton's Rings*. The pinhole is positioned in such a way that the opening lies in one of these rings and the size is also adjusted that one ring covers the whole opening. The phase of the beam reflected by the front window and the beam passing the cell differ by a fixed value for a steady state. For measurement, the sample temperature is changed linearly over time in the temperature range of interest. The change in temperature causes a change of refractive index in the sample and also thermal expansion leads to a change of thickness in the window. Thereby the phase of the beam passing the sample cell is changing with temperature which cause the *Newton's Rings* to wander. The intensity at the detector is recorded simultaneously with the temperature measured inside the cell holder. For each ring passing the pinhole, the intensity goes to a minimum and maximum sinusoidally representing a phase shift of 2π . This phase shift can be related with the change in refractive index of the sample and to determine the refractive index increment by temperature we compare the phase shift with temperature. In this process, one has to subtract the phase change due to expansion of the front window and consider that the sample beam passes the cell volume twice.

OBJECTIVES OF THE WORK - MOTIVATION

As mentioned in the introduction a deeper microscopic understanding of the thermophoresis requires careful experiments and theoretical models. Often it is necessary to design special experiments, which fulfill the assumptions used in the theoretical models. Additionally it is also useful to tailor model systems which can be easily described within a theoretical framework. On the experimental side, thermogravitational columns have a long history in thermodiffusion processes. Yet it was not possible to achieve time resolved measurements of the separation/concentration profile. To overcome this drawback a new type of thermogravitational column was designed and built. Classical columns used to be rather large to achieve a sufficient separation for the analysis of the sample. Therefore it was necessary to extract sample volume after the separation, which could lead to deviations from the actual sample composition of interest inside the column. The new thermogravitational column was planned and constructed to only need a small sample volume to access biological or other rare materials and to fit into an interferometric detection system to achieve high resolution and time resolved measurements of the concentration inside the column. This work was done in collaboration with the group of *Bou-Ali* at the Mondragon university, which carries a large wealth of experience in the design and manufacturing of thermogravitational columns, combined with our experience in design and optical detection methods.

Considering the model systems, several studies on thermodiffusion have been carried out using hard colloidal spheres. These experiments suffered from the problem of homogeneous interface properties of the particles and the reproducibility of those. The important question for the size dependence of the Soret coefficient is still open, especially for soft colloids.

The process of thermodiffusion for soft colloids is assumed to be much more complex than for hard colloids due to deformations of the soft interface and induced fluxes inside the particles. Microemulsions offered a wide range of size and shape and the possibility to precisely tune these parameters with very good reproducibility opposite to hard colloidal systems. Furthermore it is possible to avoid charge effects by using nonionic surfactant molecules. Thereby we are able to investigate different parameters systematically by fixing the surrounding. We chose a microemulsion containing n -decane, forming spherical droplets of nanometer size in proximity of room temperature, making them easy to handle. Also, the possibility to study the interfacial tension and how it is affecting the thermodiffusion properties was an important question in the field.

As already mentioned, the general question for the size dependence of the Soret coefficient in colloidal systems is not answered and still under discussion. The possibility to precisely tune the systems parameters by composition of the samples made it possible to investigate the radial dependency of the Soret coefficient by using different n -alkanes. This method offers an isothermal state with spherical particles of different radius with similar interfacial properties. All different n -alkane based microemulsions show a wide variety of structures, spherical, elongated and network like. Additionally, the different microemulsions inherit different interfacial tension properties, making it possible to explore the influence of interfacial effects in thermodiffusion.

MICRO-THERMOGRAVITATIONAL COLUMN

We present a new type of thermogravitational (TG) column, a so-called TG micro-column with transparent windows and a very small sample volume of less than 50 μL . The TG micro-column has a planar geometry with a thickness of 0.523 ± 0.004 mm, a height of 30 mm and a width of 3 mm. The concentration difference between two points at different heights is measured with an interferometer using active phase control. From the concentration difference we can determine the thermal diffusion coefficient, D_T , using the refractive index variation with concentration, which has to be determined independently. We studied the three binary mixtures of dodecane (DD), isobutylbenzene (IBB) and 1,2,3,4-tetrahydronaphthalene (THN) with a concentration of 50 wt% at a temperature of 298 K. The thermal diffusion coefficients agree within a few percent with the proposed benchmark values. In addition we investigated also the binary mixture toluene/n-hexane and compare the results with literature values. For the investigated mixtures the typical measurement times were between 30 minutes and 2 hours with an applied temperature difference of $\Delta T = 6$ K. *

*The work described in this chapter is based on J. Chem. Phys. B **116**, pp.13889-13897 (2012)

5.1 Introduction

One classical method to study the thermal diffusion or thermodiffusion behavior of binary and multicomponent mixtures is the use of a thermogravitational column (TG) [15]. Here, a vertical concentration profile develops due to a combination of thermal diffusion and convection. By combining these two effects, the separation ratio increases compared to a method only relying on the thermal diffusion process [102]. In order to make a precise measurement possible, the experiment needs to be designed carefully to avoid turbulence. The basic principle was first introduced by Clusius and Dickel [29] and has been evolved into different types of columns. Several designs of TG columns, such as annular TGs [15] and vertical parallelepipedic columns with velocity amplitude determination by laser Doppler velocimetry [103] have been successfully validated in a benchmark with other groups and methods. Nowadays, in conventional TGs a fairly large sample volume of 25 mL and more is required [11] and small samples of the mixture, typically 1.5mL, are extracted at different heights from the column after the steady state is reached [40]. These samples are analyzed to determine the composition and thus the separation ratio. For ternary mixtures, two additional properties should be determined (such as density and refractive index) in order to specify thermal diffusion coefficients [16, 67]. With classical TGs an investigation of expensive substances such as biological systems is often not possible due to the relatively large sample volume which is required to measure the refractive index and density from extracted samples with sufficient accuracy. Therefore, we developed a TG micro-column with a contactless optical detection system, which works as Mach-Zehnder interferometer. The sample volume is less than 50 μL , so that the investigation of expensive substances or substances which cannot be obtained in large quantities is feasible. Another advantage of the method is the continuous analysis of the concentration profile by measuring the phase difference between two different heights. The possibility to determine the gap width of the micro-column experimentally once it is mounted is one of the big advantages of our new micro-column, because the precise knowledge of the width is crucial as the determined thermal diffusion coefficient is proportional to the fourth power of the gap width (5.5) when calculated from the concentration difference. Using our optical method, D_T can directly be determined from the phase difference $\Delta\phi$ instead of the measured concentration differences as in conventional TG setups. In the resulting working equation for D_T , the exponent of the gap width reduces to three (5.6). Therefore, we are less dependent on the precision of fabrication. To validate the new setup, we investigated three binary mixtures of dodecane (DD), isobutylbenzene (IBB) and 1,2,3,4-tetrahydronaphthalene (THN) for a concentration of 50 wt% at a mean temperature

of 298 K, which had been used in a benchmark [101] [65] [84] . Beside the benchmark systems we investigated also the mixture toluene(TOL)/*n*-hexane(HEX) at 298 K and 50 wt%. This organic mixture has been studied by various groups [14, 62, 160] with convective and convective-free methods. In the following we discuss the design, construction and operation of the micro-column and the interferometer plus its stability. In the appendix we look into some technical details such as the instant when the temperature gradient is applied and the interferometer is disturbed by temperature inhomogeneities within and close to the column.

5.2 Experimental Setup

5.2.1 Materials

We investigated the three binary mixtures consisting of dodecane (Aldrich, purity 99%), isobutylbenzene (Aldrich, purity 99%) and 1,2,3,4-tetrahydronaphthalene (Aldrich, purity 99%) at a mean temperature of 298 K. Additionally, we studied also the binary mixture toluene (Aldrich, purity 99%) and *n*-hexane (Aldrich, purity 99%). All chemicals were used without further purification. The investigated mixtures contained 50 wt% of each component. Each sample has been investigated at least five times.

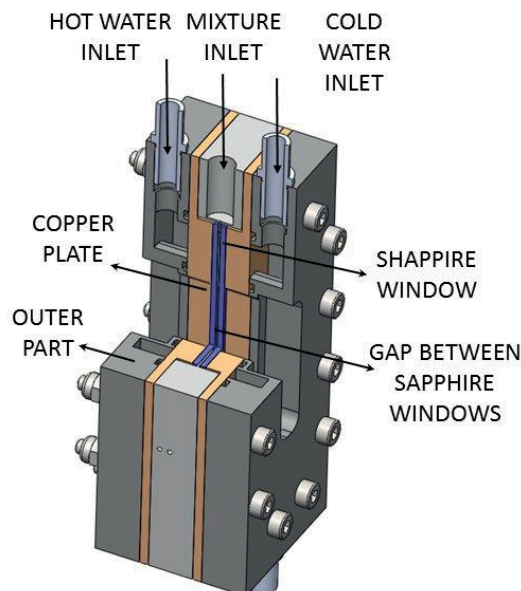


Figure 5.1: A sketch of the composed micro-column with a cut in the upper part.

5.2.2 Design and construction of the TG micro-column

The TG micro-column is composed of two sapphire windows, which are transparent in the visible range of light and have a high thermal conductivity of 34 W/mK at room temperature [22]. The transparency makes it possible to check the cell by eye for defects such as bubbles or dirt. In order to avoid a distortion of the phase front the material has been cut in the *c*-plane (0001). As thermally insulating gap material we used an advanced polymer material, polyetheretherketone (PEEK), with a very low thermal conductivity of (0.25 W/mK) [26], with good chemical resistance and a very low thermal expansion coefficient ($50 \cdot 10^{-6} \text{ K}^{-1}$) [27]. 5.1 shows a sketch of the cell. It consists of two outer parts made of stainless steel with channels for the thermostated water. For better temperature homogeneity two copper plates in good thermal contact with the two sapphire windows are inserted.

The prepared solutions were slowly inserted from below into the TG micro-column through two bores in the PEEK-Part by means of a syringe carefully avoiding bubbles. Once the cell was filled, it was closed by Teflon stoppers to avoid evaporation of the mixture.

On each side a thin channel with a length of 14.5 mm and a width of $250 \mu\text{m}$ is used to fill the gap. These inlets form dead volumes, which influence the concentration difference between the top and the bottom of the gravitational column and will be discussed in the numerical simulation section. The dimensions of the TG micro-column have been mainly determined by the limits of validity of the Furry-Jones-Onsager theory [45], the limitations on the machining process and experimental conditions such as a sufficient separation ratio and equilibration times in the order of several hours for the systems under investigation [80]. These considerations led to a gap width $L_x = 500 \mu\text{m}$, a cell height $L_{\text{total}} = 30 \text{ mm}$ and a width of $L_y = 3 \text{ mm}$, so that the aspect ratio is $L_{\text{total}}/L_x = 60$.

5.2.3 Design and construction of the interferometer

5.2 shows a sketch of the interferometer built around the TG micro-column. The micro-column is mounted inside the interferometer which is build up vertically, splitting the source beam in two parallel beams which probe the TG micro-column at different heights. The positioning of the cell and the beams is done in a way that one beam passes at the lower end of the window, the other at the upper end. Typically the vertical distance of the two beams is adjusted to 22 mm . In order to measure at other height differences the vertical position of one of the probing beams can be shifted by moving the two opposing optical elements up- or downwards. A He-Ne laser (Melles Griot) with a nominal power of 1 mW and a beam

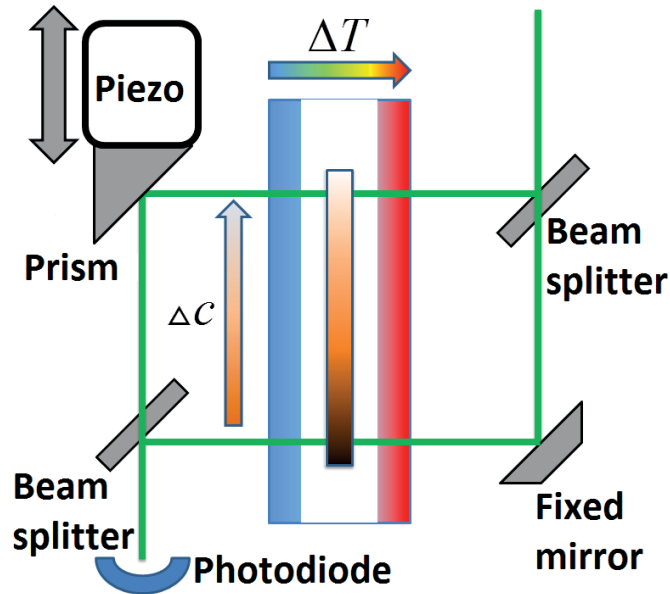


Figure 5.2: Schematic sketch of the interferometer probing the concentration difference at two different heights of the TG micro-column with a horizontal temperature gradient. The concentration difference results in a phase shift $\Delta\phi$ of the intensity signal determined by a 2π scan of the prism mounted on the piezo stack.

width of 1 mm, operating at 543 nm is used as beam source. The typical power at the photodiode (Hamamatsu S2386-8K, active dia. 5.8 mm) is 0.25 mW. Thermostated water from two thermostats (Lauda RE-306) flows through two stainless steel plates mounted at the two sides of the TG micro-column. To achieve homogeneous starting conditions and to determine the initial phase, the water of both thermostats is mixed and both sides are kept at the same temperature. At time t_0 the temperature gradient is applied by separating the flow from both thermostats.

We use a mirror mounted on a piezo stack (PI P-840-10) to control the phase position while measuring. The piezo is ramped with a step rate of 10 kHz so that we determine the phase from a full 2π scan 2 times per second. This will yield precise knowledge of the initial and final phase positions, making the determination of the absolute phase shift more exact than measuring only the intensity. The piezo and the recording of the phase shifts (π) are controlled by a computer equipped with an interface card (NI PCI-6014).

The beam width of 1 mm is quite broad compared to the distance between the two probing beams and the question is whether this will influence the measurements. We can do the following *Gedankenexperiment* by splitting artificially an arbitrary narrow laser beam in one center beam and two *edge beams*, one below and one above the center beam. The vertical concentration profile in the cell is linear, so that the phases of the *edge beams* are shifted by

the same amount but in different directions. The resulting *interfering beams* show equal phase shifts stemming from the center and the edges. The relative large area of the photodiode averages over the *beams* recording the same phase as the *center beam* with a slightly lower contrast. Due to the fact that we determine the concentration change by measuring the phase difference, the influence on the measurement should be small as long as the concentration profile is linear over the beam width. In our case the concentration profile is even linear over the entire cell height so there is no influence on the measured phase.

5.2.3.1 Interferometric measurement

In an interferometer the intensity varies when the relative phase between the two beams changes. In a simple analysis the phase change can be measured by counting the number of minima and maxima of the varying intensity. To achieve a higher resolution than π the current intensity can be compared to the intensity extrema. This simple method relies on the intensity stability. Therefore, we added an active phase control to our interferometer to achieve a higher precision and reliability. We change the optical path length of one of the beams with a mirror mounted on a piezo and record the modulated intensity (c.f. 5.3). The resulting intensity is fitted to a sinusoidal function which gives a phase value. The curves shown in 5.3 correspond to the starting time t_0 and a later time t_1 . Due to a relative phase shift between the two beams, the signal at t_1 is shifted by $\Delta\phi$ to the right. This full 2π -scan takes less than 1 second and is therefore much faster than the expected concentration changes in the micro-column. We can analyze the phase change by using the forward and the backward movement of the piezo. Both scans give the same phase behavior except for a constant offset caused by the known hysteresis effect of piezos. The interferometer with active phase control is less sensitive to intensity fluctuations caused by mechanical disturbances and we do not need the reference information about the actual intensity extrema to be measured in advance.

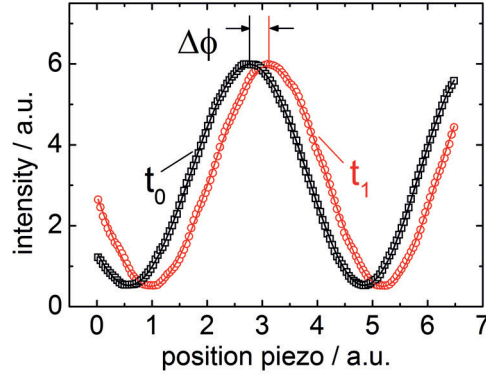


Figure 5.3: Sketch of the active phase control mechanism. Two intensity scans recorded at two different times t_0 and t_1 (squares and circles) and the fitted sinusoidal curves. The phase shift $\Delta\phi$ is caused by concentration changes.

5.2.3.2 Characterization of the cell

The gap width of the micro-column has been determined with a microscope setup, focusing a probing beam onto the surface and detecting the reflected signal. The objective used (10X Mitutoyo) has a long working distance of 33.8 mm and a very small focus depth of $3.58 \mu\text{m}$. A principle sketch of the setup is shown in 5.4 (a). When the beam is focused on an interface, the reflected beam forms a sharp focused spot and the intensity is on its local maximum. We record the focus shift from the first window-cell interface to the second via an elevator stage. The precision of the height reading is better than $0.5 \mu\text{m}$. With this method we determined the average cell thickness to be $523 \mu\text{m}$ with an uncertainty of $4 \mu\text{m}$. The roughness of the inner walls is smaller than the uncertainty.

5.3 Theoretical approaches

5.3.1 Determination of the phase shift due to concentration

As sketched in 5.2 we are probing the relative phase difference along the TG micro-column at two different heights. The phase ϕ between the two beams corresponds to their optical path lengths s_{top} and s_{bottom} inside the column gap via

$$\phi = k (s_{\text{top}} - s_{\text{bottom}}) \quad (5.1)$$

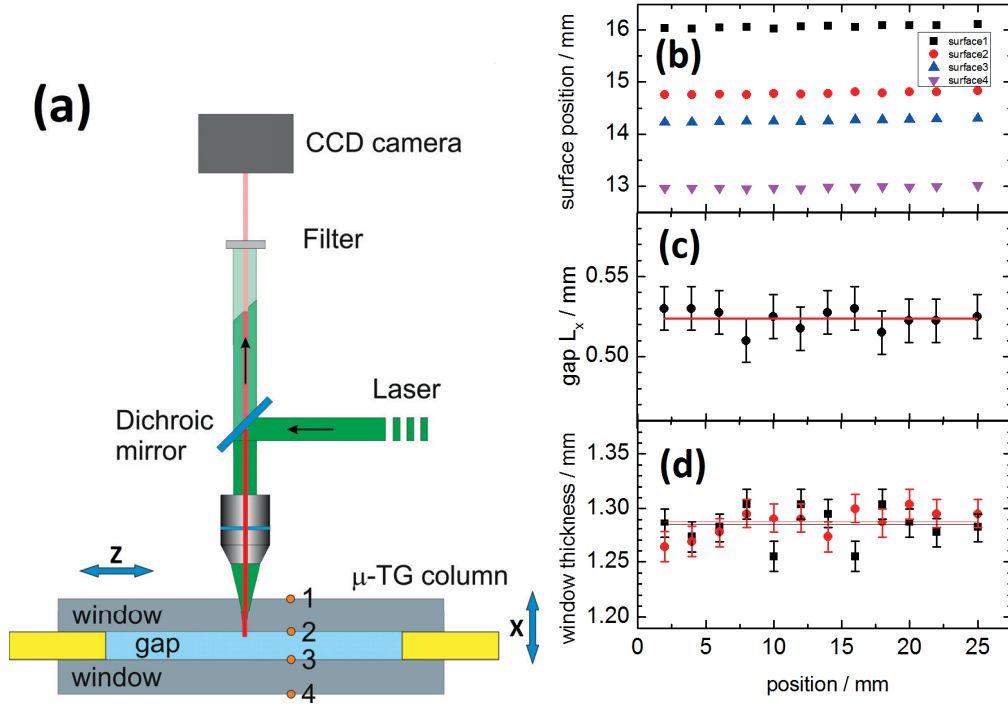


Figure 5.4: Optical tweezers setup to determine the position of the sapphire surfaces. The cell can be moved in x - and z -direction on a micrometer stage. (b) Position of the different surfaces along the cell. (c) The calculated gap width and the width of the (d) sapphire windows as function of the cell height.

with the wave vector $k = (2\pi)/\lambda$ and λ , the wavelength of the laser, assuming a perfectly frequency stable laser. A change in the optical path lengths, Δs_{top} and Δs_{bottom} at the top and bottom, respectively, leads to a change in the phase $\Delta\phi$:

$$\Delta\phi = k (\Delta s_{\text{top}} - \Delta s_{\text{bottom}}) \quad (5.2)$$

We assume here that the change in refractive index along the column in vertical direction depends only on the concentration difference between top and bottom beam positions. Supported by the simulations we suppose that the temperature changes linearly over the gap (c.f. 5.7 (a)). Therefore, the mean temperature is in the middle of the gap and it is a constant as function of the height. Looking at the horizontal variation of the refractive index we have on the warm side a slightly lower refractive index compared to the middle and at the cold side a slightly higher refractive index compared to the middle. Due to the linearity of the temperature the averaged refractive index probed by the laser beam corresponds to the value in the middle, which is constant over the height of the cell. Therefore we consider that all observed changes in the refractive index are due to concentration changes. Since the

change of the optical path results from the change in refractive indices, Δn_{top} and Δn_{bottom} at the top and bottom, respectively, one can write:

$$\begin{aligned} \Delta\phi &= kL_x(\Delta n_{\text{top}} - \Delta n_{\text{bottom}}) = kL_x\Delta n \\ \Leftrightarrow \Delta n &= \Delta\phi(kL_x)^{-1} \end{aligned} \quad (5.3)$$

with the gap width L_x and the refractive index difference Δn between top and bottom. Additionally, we neglect the phase changes between the top and bottom beam caused by refractive index change and thermal expansion of the sapphire windows (c.f. 5.1) and the air around the cell due to the temperature gradient, since both beams are affected in the same way. Dividing both sides of 5.4 by Δc and replacing $\Delta n/\Delta c$ by $(\partial n/\partial c)_{p,T}$, we obtain an expression for Δc :

$$\Delta c = \frac{1}{kL_x} \left(\frac{\partial n}{\partial c} \right)_{p,T}^{-1} \Delta\phi. \quad (5.4)$$

The refractive index increment $(\partial n/\partial c)_{p,T}$ can be determined independently. Furthermore, we would like to point out that due to continuous observation of $\Delta\phi$ also phase differences larger than 2π can be detected.

5.3.2 Determination of the concentration change

We use the Furry-Jones-Onsager (FJO) theory [45, 79] to calculate the concentration difference at the steady state at two points separated by L_z to

$$\Delta c = 504 \frac{\nu}{\alpha g} D_T c_0(1 - c_0) \frac{L_z}{L_x^4}, \quad (5.5)$$

where c_0 is the initial mass fraction concentration of the reference component, ν is the kinematic viscosity, α is the thermal expansion coefficient, L_z is the vertical distance between the probing laser beams (22 mm), D_T the thermal diffusion coefficient, and g the gravity acceleration. In the derivation it is used that the initial concentration c_0 changes only slightly, so that D_T and also D can still be treated as a constant. This assumption might break down, if large concentration changes occur. Combining 5.4 and 5.5 gives the thermal diffusion coefficient

$$D_T = \frac{1}{504} \frac{\alpha g}{k\nu} \frac{1}{c_0(1-c_0)} \frac{L_x^3}{L_z} \left(\frac{\partial n}{\partial c} \right)_{p,T}^{-1} \Delta\phi \quad (5.6)$$

Due to fact that we do have a method which measures the phase continuously, we might also look at the temporal behavior of the transient concentration difference. This is given by [145]

$$\Delta c = \Delta c_\infty \left(1 - ae^{-t/t_r} \right), \quad (5.7)$$

It needs to be pointed out that 5.7 is only satisfied for times t larger than one third of the relaxation time t_r , because it corresponds only to the first term of an infinite series. Another shortcoming of 5.7 is that an ideal infinitely sharp switching of the temperature gradient is assumed, which practically cannot be achieved. In the future we will develop an experimental procedure to obtain the molecular diffusion coefficient from the transient signal.

5.4 Numerical Simulations

5.4.1 Numerical validation of the TG micro-column

In order to validate the proposed geometry for the thermogravitational micro-column, a numerical study using ANSYS-Fluent software [1] is made. The simulations are performed using a finite volume (illustrated in 5.5) method in 3D (FVM) based on fluid flow solutions under the assumption of an incompressible fluid and laminar flow under atmospheric pressure.

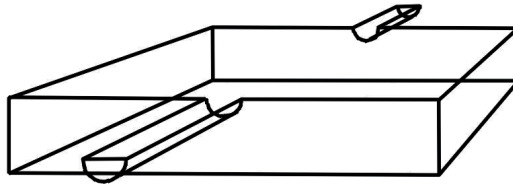


Figure 5.5: A sketch of the cell volume including the considered dead volumes, which are used for filling the micro-column.

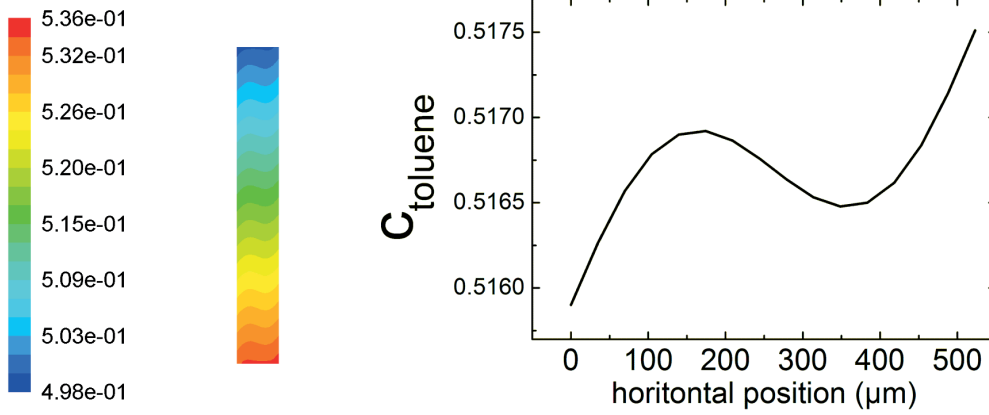


Figure 5.6: Numerical simulation results of the toluene mass fraction profile in the binary mixture TOL/HEX. The left figure shows the profile over the entire height of the micro-column. The right figure is a plot of the concentration profile at a height of 15 mm at the stationary state.

The model covers the Fickian mass, the thermal diffusion and the Navier-Stokes equation, whereas the density changes in the fluid with concentration and temperature are covered by the Boussinesq approximation [104]:

$$\rho = \rho_0(1 - \alpha(T - T_0) + \beta(c - c_0)) \quad (5.8)$$

Where ρ is the local density of the mixture, ρ_0 is the density of the homogenous mixture, T_0 is the mean temperature, $\alpha = -(1/\rho)(\partial\rho/\partial T)_{p,c}$ is the thermal expansion coefficient and $\beta = +(1/\rho)(\partial\rho/\partial c)_{p,T}$ is the mass expansion coefficient. The value of the mass and thermal expansion coefficient are experimentally determined [12]. We used no-slip boundary conditions and applied a constant temperature gradient of 5 K perpendicular to the gravity field.

Table 5.1: Experimental density, ρ_0 , dynamic viscosity, μ , mass expansion coefficient, β , and the thermal diffusion coefficient, D_T , for the mixture TOL/HEX with a mass fraction of 0.5167 at $T=298$ K used in the numerical simulation.

ρ_0 / kg/m ³	μ / Pa · s	α / K ⁻¹	β	D_T / 10 ⁻¹² m ² /sK	D / 10 ⁻⁹ m ² /s
748.19	3.861	1.23	0.275	13.7 [Ref. 160]	2.78 [Ref. 160]
				13.2 [Ref. 14]	2.85 [Ref. 62]
				14.0 [Ref. 62]	

The governing equations are solved using a pressure-based implicit simple velocity-pressure coupling scheme with a double-precision module. The second order numerical discretiza-

tion scheme is used for pressure, density, momentum and mass flux to avoid numerical instabilities. The iterative convergence criteria is set to 10^{-9} for all solution variables. For the preprocessing of the geometry Gambit [2] is used, where the geometry of the gap ($523 \mu\text{m} \times 3 \text{ mm} \times 30 \text{ mm}$) was defined. This 3D computational domain consists of non-uniformly spaced hexahedral mesh cells. A very fine mesh resolution was used with 720000 hexahedral cells to have a realistic representation of the concentration gradients.

Table 5.2: Comparison between experimental and numerical simulation results of the stationary separation under the thermogravitational effect for the new design of the micro-column for the mixture TOL/HEX with a mass fraction of 0.5167. D_T is the average of the individual literature values listed in 5.1.

L_z / mm	$\Delta c_{5.5}$	Δc_{fluent}	dev. / %	$D_{T_{\text{exp}}}$ / $10^{-12} \text{m}^2/\text{sK}$	$D_{T_{\text{fluent}}}$ / $10^{-12} \text{m}^2/\text{sK}$	dev. / %
30	0.0295	0.0297	<1	13.63	13.74	<1
22	0.0216	0.0218	<1	13.63	13.76	<1

5.4.1.1 Simulation results

For the numerical validation of the micro-column, the thermogravitational effect in the steady state is analyzed using a reference mixture TOL/HEX at a mass fraction of 0.5167 and at $T = 298 \text{ K}$. 5.1 lists the parameters for the TOL/HEX mixture. Köhler and Müller measured only at $T = 296 \text{ K}$ and higher temperatures so that D_T and D at $T = 298 \text{ K}$ have been obtained by linear interpolation [62].

For the TOL/HEX mixture with $c_0 = 0.5167$ the steady state temperature, velocity and concentration profiles obtained from numeric simulations are shown in 5.6 and 5.7. 5.7(a) show the temperature profile within the gap which decays linearly from the warm to the cold side. 5.6 and 5.7(b) show the velocity and the toluene concentration profiles inside the gap at the mid-height of the micro-column at 15 mm. The velocity (c.f. 5.7(b)) has a cubical profile while the concentration profile (c.f. 5.6) has to be described by a polynomial of fifth order. 5.7(c) show the distribution of the concentration referring to the densest component (TOL) in the stationary state. Along the micro-column the results show an increase in the concentration of the densest component (TOL) in the lower and of the lightest component (HEX) in the upper parts of the column. The profiles obtained in the micro-column are those predicted by the thermogravitational theory [144] [78].

5.2 summarizes the results of numerical simulation and compares the concentration difference and the thermal diffusion coefficient in the steady state with the experimental values. The

simulation results agree within a few percent with the experimental values and the mean experimental value agrees within 1%. The excellent agreement between the simulation results and the experimental values shows that the design fulfills the conditions of the FJO theory.

Additionally, we analyzed numerically the effect on the concentration difference probably caused by dead volumes at the inlet and outlet. The considered dead volumes are in the order of $3.625 \mu\text{L}$ stemming from two channels with a diameter of $250 \mu\text{m}$ and 14.5 mm in length. 5.5 shows the model used. As shown in 5.3, the obtained concentration difference from the simulation Δc_{fluent} agrees within 1% with the calculated concentration difference $\Delta c_{5.5}$. The determined thermal diffusion coefficients for TOL/HEX, THN/IBB, IBB/DD and THN/DD mixtures at a mass fraction of 50% at $T=298 \text{ K}$ agree also within a few percent with the simulation results obtained for a gap of $523 \mu\text{m}$ including the dead volume effect.

Table 5.3: Experimental and numerical results for the investigated binary mixtures at $T=298 \text{ K}$ and a mass fraction of $c=0.5$. In all simulations the dead volume caused by the inlet and the outlet have been considered.

Mixture	$\Delta c_{5.5}$ $L_z = 22 \text{ mm}$	Δc_{fluent} $L_z = 22 \text{ mm}$	dev. / %	$D_{T_{\text{exp}}}$ / $10^{-12} \text{ m}^2/\text{sK}$	$D_{T_{\text{sim}}}$ / $10^{-12} \text{ m}^2/\text{sK}$	dev. / %
TOL-HEX	0.0213	0.0214	0.47	13.6 [ave]	13.56	-0.29
THN-DD	0.0451	0.0453	0.44	5.90 [Ref. 101]	5.93	0.50
THN-IBB	0.0180	0.0177	-1.66	2.80 [Ref. 101]	2.78	-0.71
IBB-DD	0.0207	0.0206	-0.48	3.70 [Ref. 101]	3.68	-0.54

5.5 Results and discussion

5.8 shows a typical time development of the phase for the system TOL/HEX and THN/DD at an average temperature of $T = 298 \text{ K}$ and a temperature difference of $\Delta T = 6 \text{ K}$ over the gap of the cell. At time $t = 0$ the temperature gradient is applied while at earlier times both sides of the cell are kept at an average mixing temperature, T_{mix} , which leads to a constant phase after some settling time of the order of an hour. Once the temperature gradient is applied, the phase shows an exponential increase until it reaches a plateau value. The phase difference is determined by the difference of the plateau value in the steady state and the phase at the baseline before switching on the temperature gradient. In all our experiments this phase change in the jump was of the order of 0.2π and its origin will be discussed in the appendix. The so determined phase difference is used in 5.6 to calculate the thermal diffusion coefficient, D_T . The obtained values for the four systems are listed in 5.4 and shown

in 5.9 in comparison with literature values. For most of the systems the deviations are below or around 6%. The absolute uncertainty was below $0.6 \cdot 10^{-12} \text{m}^2 \text{s}^{-1} \text{K}^{-1}$. With this new TG micro-column design in combination with the interferometric detection with one wavelength we surrender a strong point of the TGs, namely the investigation of ternary mixtures. In addition we employ very small sample volume of less than $50 \mu\text{L}$, with similar measurement times compared to the conventional TGs of 30 minutes up to 2 hours for the investigated mixtures. Both the design and the measurement system developed in this work for the new TG micro-column installation is well suited for biological systems. The transparent windows of the TG micro-column have several advantages. First, a precise determination of the gap width over the entire height of the TG micro-column is possible. This is especially important, because the thermal diffusion coefficient, D_T depends on the gap width to the power of three (c.f. 5.6) for our optical system.

Table 5.4: Thermal diffusion coefficients determined for four binary mixtures with 50 wt%. All measurements have been performed at 298 K. The error is variance of the mean from five individual measurements.

Mixture	D_T / (this work) $10^{-12} \text{m}^2 \text{s}^{-1} \text{K}^{-1}$	D_T / (literature) $10^{-12} \text{m}^2 \text{s}^{-1} \text{K}^{-1}$	dev./ %
Tol-Hex	13.0 ± 0.35	13.6 [ave]	-0.44
THN-DD	5.87 ± 0.23	5.9 [Ref.101]	-0.50
THN-IBB	2.63 ± 0.01	2.8 [Ref.101]	-6.07
IBB-DD	3.91 ± 0.15	3.7 [Ref.101]	+5.68

So far we have only studied organic mixtures, but the setup should also work for aqueous solutions. Due to the higher surface tension of water, special care needs to be taken in order to avoid air bubbles in the cell. Another nice feature of the TG micro-column is that we can monitor the concentration change as function of time. In principle it should therefore also be possible to determine the diffusion constant D in the same setup. In the present design, however, we were not able to obtain sufficiently accurate values for D . The largest problem is the uncertainty in ΔT , which needs to be obtained at the inside of the sapphire windows. We hope that we can analyze in the near future the time dependence of the concentration to obtain also the Soret coefficient, S_T , but this might also require a more sophisticated model for the data analysis.

Compared to other optical detection methods such as Thermal diffusion forced Rayleigh scattering (TDFRS) [63, 155] or Beam Deflection (BD) [64, 65] the sample volume of $50 \mu\text{L}$ is very small. The equilibration times are comparable with BD, but much slower than in the TDFRS experiments. One drawback of the method is that we are not capable to determine

also the diffusion coefficient D using 5.7, because the experimental data show systematic deviations from a simple exponential function. The operating expenses are much lower than in the case of the TDFRS and comparable with the BD. This method might open up other possibilities by combining it with a microscope and fluorescent detection methods. This new method will also be useful for further benchmark campaigns as a convective method in combination with optical detection.

In conclusion we can state that the TG micro-column is a nice compact device which allows reliable, contactless measurements of the thermal diffusion coefficient, D_T . The typical deviations from the literature values found are in the order of 5% (c.f. 5.4), which is comparable with the deviation found in the benchmark [101].

5.6 Appendix

As mentioned in the results and discussion section we observe always a fast phase jump shortly after switching on the temperature gradient. In the following section we will discuss this issue and will relate it to a slight asymmetry in the formation of the temperature gradient.

5.6.1 Characterization of the temperature switching

Before the measurement starts, we mix the water of the two thermostats, which are kept at different temperatures T_{cold} and T_{warm} . We adjust the flows of the two thermostats so that the temperature of the mixed water corresponds to the average of the two temperatures $T_{\text{mean}} = 0.5 \cdot (T_{\text{cold}} + T_{\text{warm}})$. Practically, small deviation of the order of $\Delta T = 0.1\text{K}$ are detected. This leads to a small temperature difference to the mean temperature, T_{mean} , of the cell prior the temperature gradient and causes a small horizontal asymmetry in the $(\partial n / \partial T)_{p,T}$ -contributions. If the thickness of the gap and the windows between top and bottom are equal, this affects top and bottom in the same way, so that changes in the phases should cancel.

5.10 shows the temperatures on the cold and the warm side as function of time after the temperature gradient has been switched on. The temperatures have been measured with an infrared camera (FLIR T400) at the surface of the sapphire windows, which has been covered with a 100 μm teflon foil to avoid reflections. Due to the insulation of the teflon foil the temperature reading will be a bit lower compared to the temperature at the outside of the

sapphire window, but this will affect both sides in the same way. Also the surrounding metal parts have been taped to prevent reflections at the metal surfaces, which could influence the temperature reading. 5.10 shows the time development of the temperatures on the warm and cold side, which can be described by an exponential increase and decrease, respectively. Typical time constants of an exponential fit to reach the final values T_{cold} and T_{warm} are 27 s and 25 s, respectively, indicating that heating is slightly faster than cooling. This leads as in the upper graph of 5.10 shown to a slight overshoot of the average temperature, T_{mean} . But this effect will also influence the top and the bottom in the same way so that those contributions cancel.

Performing a thermal analysis with the infrared camera, we have seen that during the initial state of applying the temperature gradient the temperature propagates from the bottom to the top, which means that the final temperature at the bottom is reached earlier compared to the top. The lower graph of 5.10 shows the temperature at the top and bottom measured at the metal surface of the cell. Due to the small window of a width of 3 mm we were not able to obtain reliable measurements at two different height positions directly at the sapphire windows. As seen in the figure the time constants between top and bottom differ substantially. Typical exponential time constants at the bottom and at the top of the cell are 16 s and 27 s, respectively. This is indeed a problem of the present setup and leads to phase shift between the bottom and the top present in the beginning of the experimental phase curves. This difficulty can be solved by using a cross-flow in the micro-column similar to the circulating water loops used by Zhang *et al.* [160] or by imaging the phase profile over the entire height.

5.6.2 Stability and response of the interferometer

The precision of the setup depends strongly on the stability of the interferometer. The drift should be very small over the measurement time. A typical measurement time is of the order of 30 minutes to 2 hours depending on the system. A small drift has little influence and can be subtracted from the measured signal. To achieve a very small drift, we have to insulate the laser beam paths from temperature changes by insulating the cell and the tubes. This will reduce the effect but not cancel it out completely. The interferometer mirrors are mounted on vertical pillars. Care needs to be taken to have stable temperature conditions taking into account heat sources and fluctuations.

A typical example for the time dependence of pure THN is shown in 5.11(b). At short

times when no temperature gradient is applied, we observe a constant drift of the phase. After 10 minutes a temperature gradient is applied and the phase changes rapidly within a minute and approaches then a constant drift rate. When the temperature gradient is switched off, we observe the reverse behavior. A similar jump occurs also in the empty cell and during the regular measurements and is always in the order of 0.2π . Therefore, we assume that it is related to an asymmetry in the setup, but the reason is not fully understood. In the last section we discussed a small vertical temperature gradient and the temporal change of the mean temperature in 5.11(b) and 5.10 (top graph), respectively. The maximal temperature difference between top and bottom is of the order of 0.2-0.3 K, with a typical $(\partial n / \partial T)_{p,c} = 5 \cdot 10^{-4} \text{K}^{-1}$ we obtain a phase shift of the order of 0.2π - 0.3π , which corresponds to the typical observed values of 0.2π . On the other hand it is also possible that the two beams are slightly deflected leading to a shift of the interference pattern, which results then into an intensity change. We want to clarify this issue in the future by comparing different micro-columns.

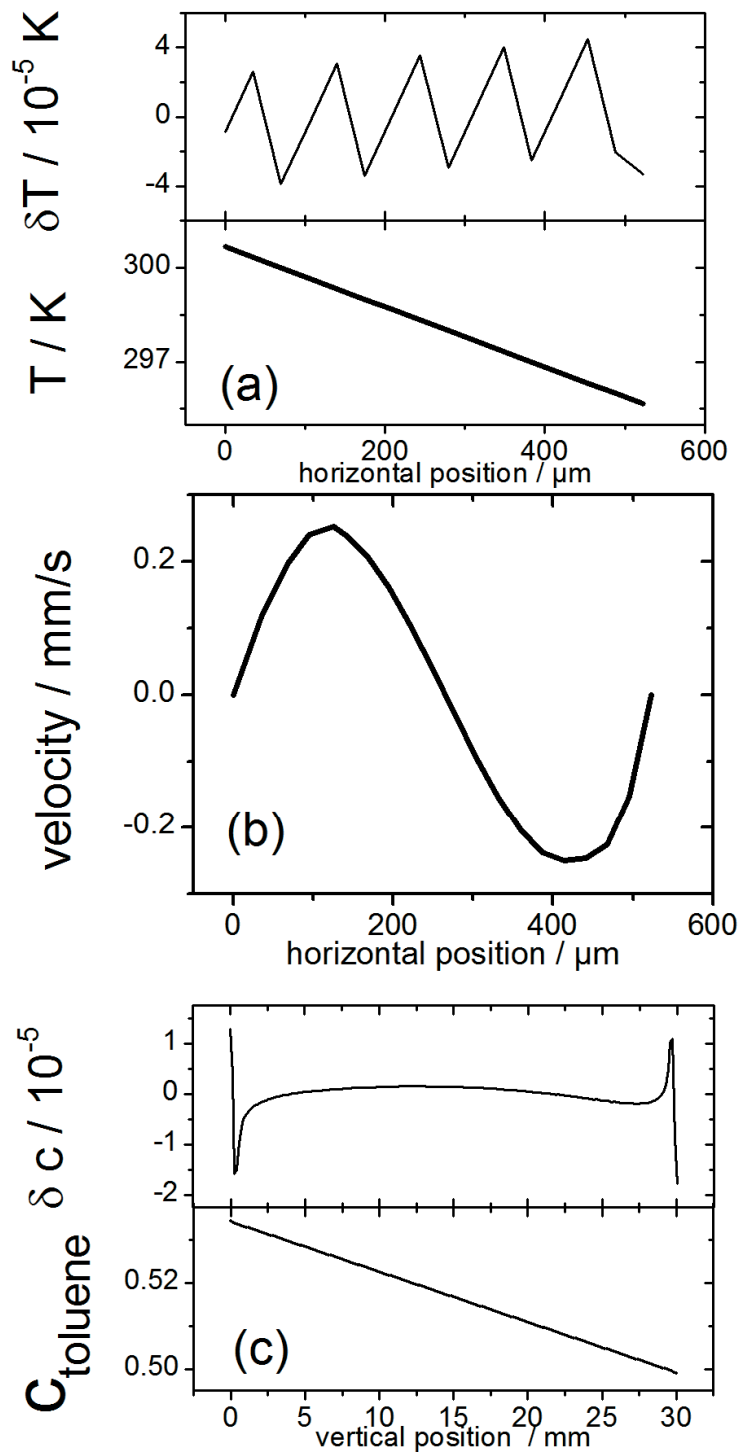


Figure 5.7: Numerical simulation results for the binary mixture TOL/HEX at the stationary state (a) Temperature profile within the micro-column gap. The upper part shows the deviations from a linear fit. (b) Velocity profile within the micro-column gap at a height of 15mm. (c) The vertical concentration distribution profile of the TOL mass fraction in the middle of the gap along the micro-column. The upper part shows again the deviations from a linear fit.

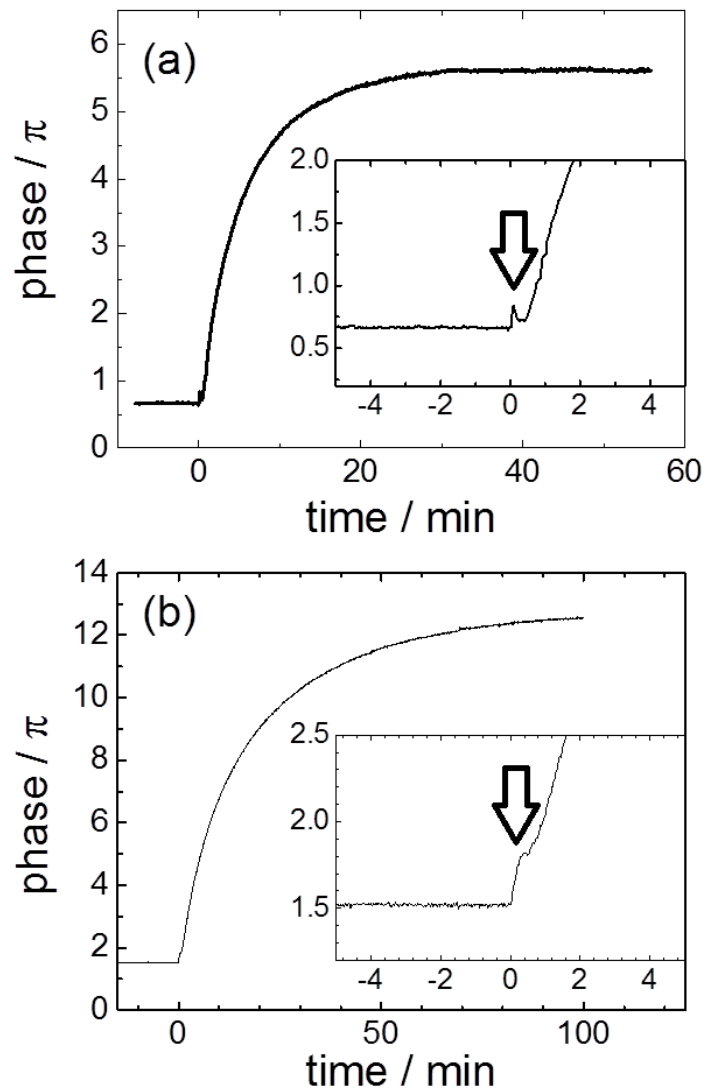


Figure 5.8: (a) Typical experimental results for phase shift between top and bottom for the mixture TOL/HEX and (b) THN/DD with a mass weight fraction of 50% as function of time. The time base has been chosen in such a way that at time zero the temperature gradient has been enabled. The inset shows the phase close to the turn-on time. The origin of the fast jump in the signal will be discussed in detail in the appendix.

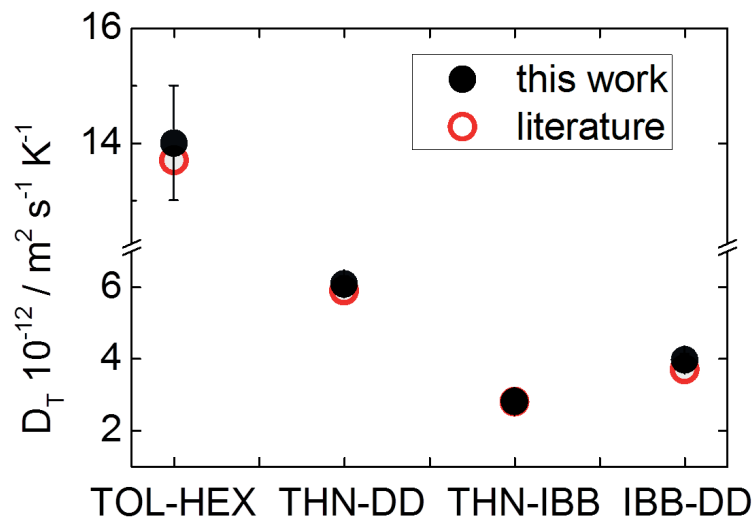


Figure 5.9: The thermal diffusion coefficient, D_T , for the four studied systems in comparison with literature values. The largest absolute deviations are found for the system TOL/HEX, while the largest relative deviation of around 6% is found for the system THN-IBB.

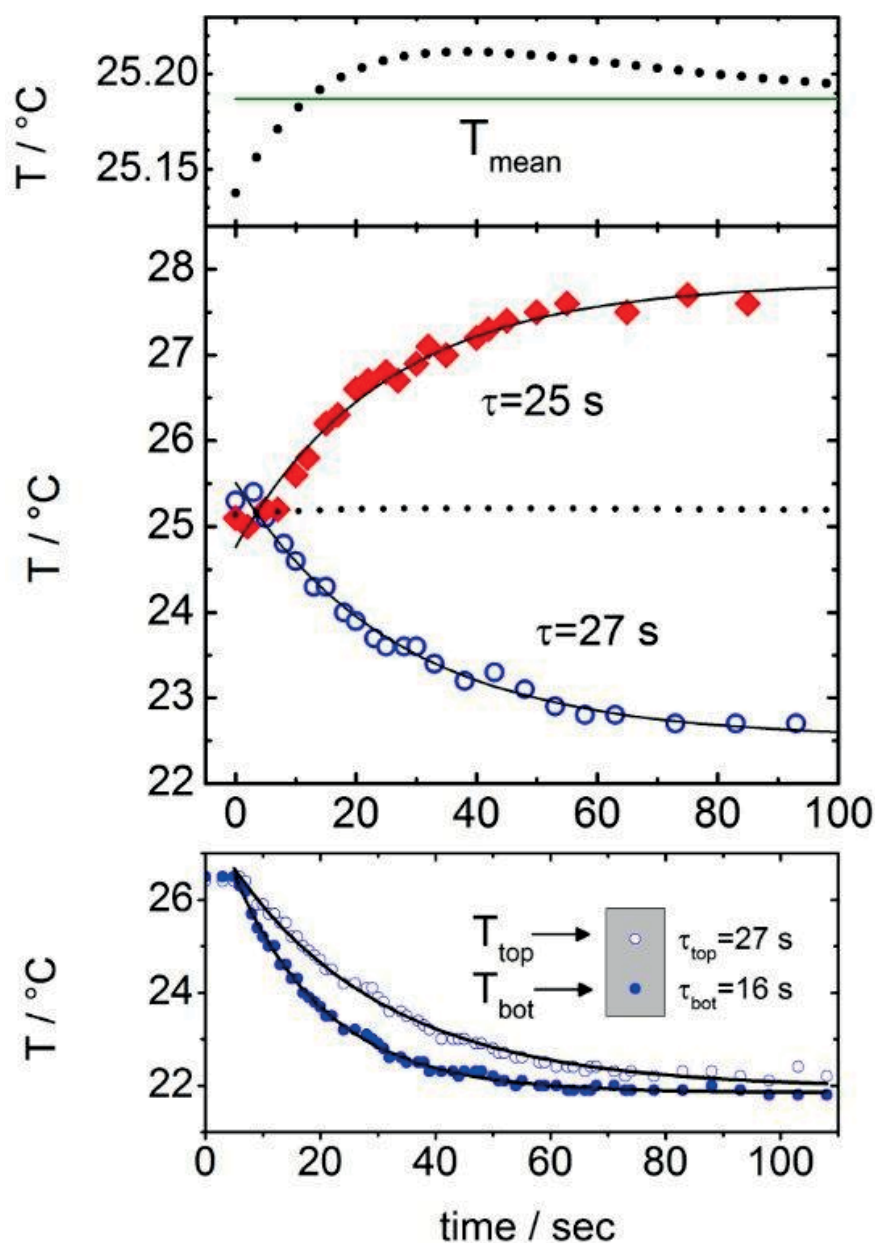


Figure 5.10: Top graph: temperature at the outside of the sapphire windows at the two sides (warm side - filled diamonds; cold side - open circles) of the TG micro-column filled with toluene as function of time measured by means of an infrared camera. The upper graph shows that due to different time constants for the warm and the cold side there is a small overshoot in the mean temperature (small dots) as function of time. Bottom graph: development of the temperature at the bottom and at the top of the cell measured at the covered metal surface. The temperature equilibrates at the bottom of the cell much faster than at the top, so that for a short time a vertical temperature gradient in the order of 0.2-0.3 K is established. The solid lines are exponential fits with time constants given in the graph.

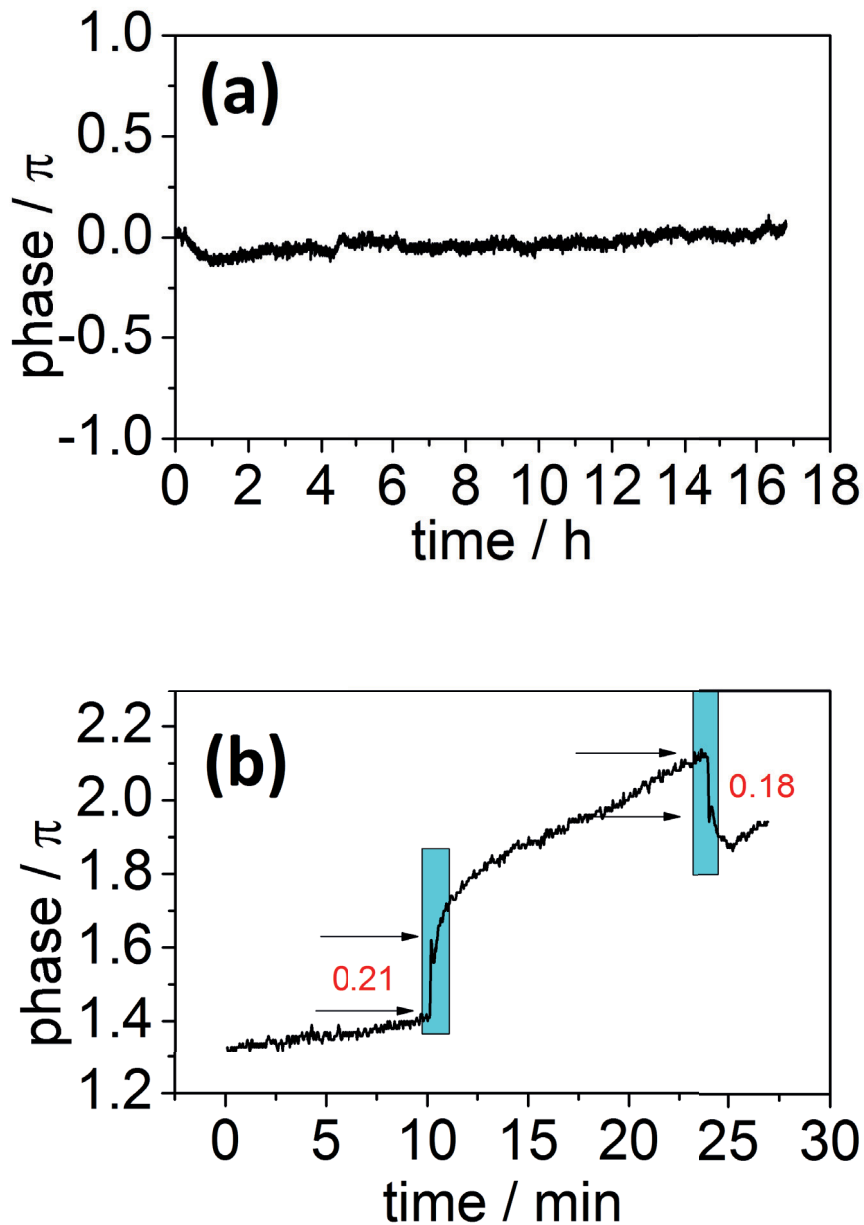


Figure 5.11: (a) Phase drift as function of time. After equilibration within the first hour, the phase drifts with a rate $0.0064 \pi/h$. This corresponds to a drift of less than 0.02π for a measurement time of 3 hours, which results for IBB/THN, the system with the weakest measurement signal, in a relative error of 1%. (b) Phase response in pure THN, when the temperature gradient is switched on and off, respectively.

SORET COEFFICIENT IN NONIONIC MICROEMULSIONS:
CONCENTRATION AND STRUCTURE DEPENDENCE

*Here we investigate the thermal diffusion behavior of the nonionic microemulsion water/*n*-decane/pentaethylene glycol monododecyl ether (C₁₂E₅). We study the dependence of the Soret coefficient on the structure and composition by infrared thermal diffusion Rayleigh scattering. The form and size of the microemulsion structure is characterized by dynamic light scattering and small angle neutron scattering. The system was examined in the one-phase region between the near critical boundary and the emulsification failure boundary, where oil swollen nanostructures stabilized by an amphiphilic surfactant film are dispersed in a continuous water phase. The size and shape of these structures as well as the interfacial properties of microemulsions can be varied by changing temperature and composition, which allows systematic study of their influence on the thermal diffusion properties. In addition, we analyze the relationship between the Soret coefficient and the temperature dependence of the interfacial tension as proposed by A. Parola and R. Piazza [Eur. Phys. J. E 15, 2004, 255-263] and find reasonable agreement for spherical microemulsion droplets. **

*The work described in this chapter is based on J. Chem. Phys. B117, pp. 5614-5622 (2013)

6.1 Introduction

If mixtures or suspensions are exposed to a temperature gradient, thermal diffusion, the migration of the molecules either to the warm or the cold side, occurs. This process results in a concentration gradient that is opposed by ordinary diffusion and reaches a steady state described by:

$$D\nabla c = -D_T c(1-c)\nabla T \quad (6.1)$$

with the ordinary diffusion coefficient D , the thermodiffusion coefficient D_T , the concentration c and temperature T . The Soret coefficient S_T is the ratio D_T/D of the thermal diffusion coefficient D_T and the collective diffusion coefficient D . The separation of different components in a temperature gradient can be exploited in the enrichment and characterization of polymers and colloids, [18, 156] and also plays an important role in many biological systems [152].

Even though this phenomenon has been known for more than 150 years, [30, 72] there exists no microscopic theory to describe thermal diffusion in liquid mixtures. There are some empirical correlations between thermal diffusion and material properties: The Soret coefficient seems to increase for large differences in mass and size, and typically the heavier species migrates to the cold side []. Besides the parameters noted above, the Soret coefficient has been associated with Marangoni forces [3], which show the relationship between the thermal gradient and the asymmetry in the interfacial forces acting on a colloidal droplet or particle. To get a better understanding of the thermal diffusion behavior, it would be desirable to vary parameters such as temperature, concentration, size and mass of the particles systematically and independently from each other. In this work, microemulsions are used as model systems where methodical shape, size and concentration variations of the microemulsion droplets as function of composition and temperature are possible [134]. Microemulsions are thermodynamically stable mixtures that are macroscopically isotropic but structured on the nano-scale. They consist of at least three components: (A) polar (e.g. water), (B) non-polar (e.g. *n*-decane) and amphiphilic (e.g. pentaethylene glycol monododecyl ether ($C_{12}E_5$)) (C). A and B are in general immiscible with each other. The amphiphile will preferentially adsorb at the interface between the polar (A) and non-polar (B) components which leads to the formation of an amphiphilic interfacial film. As a consequence, the solubilization of A in B and vice versa are facilitated by the amphiphile.

Depending upon composition and temperature, aggregates of different size and shape, networks, bicontinuous or lamellar structures are formed [137]. Water-rich microemulsions and

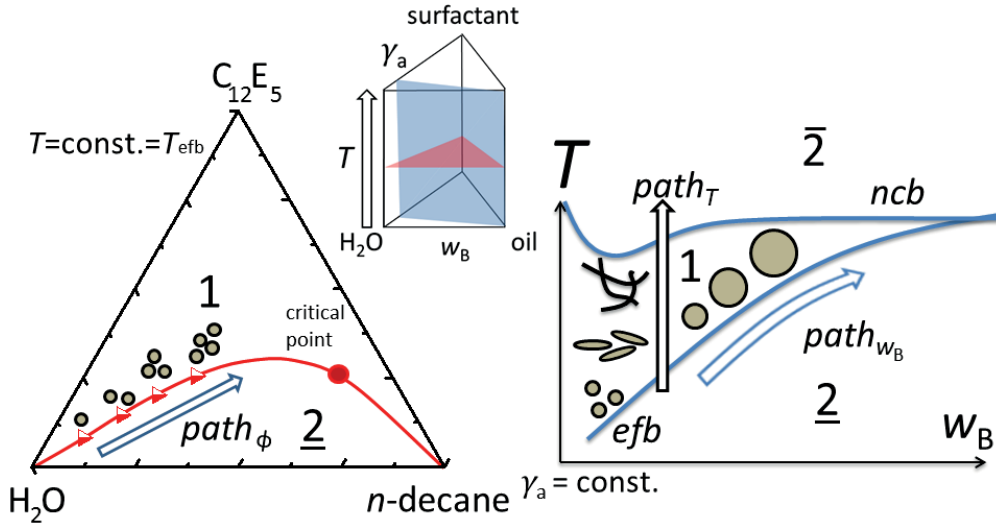


Figure 6.1: Schematic phase behavior of water-rich non-ionic microemulsion systems together with the occurring microstructures. The left figure shows a isothermal cut through the phase prism (red plane). Increasing the amount of oil and surfactant at a constant oil-to-surfactant ratio leads to an increasing number of droplets. The red line indicates the binodal. The right figure shows a vertical cut through the phase prism at constant γ_a (blue plane). The one phase region is limited by the so-called emulsification failure boundary (efb) and the near critical boundary (ncb). Spherical droplets are formed along the efb, which increase in size with increasing oil content. Moving away from the efb leads to an elongation of the aggregates. At temperatures close to the ncb network-like structures are often found.

their temperature dependence are appropriately studied by the stepwise addition of oil to a mixture of water and non-ionic surfactant [82]. The temperature dependent phase behavior of such mixtures is sketched on the right hand side of Figure 6.1 and corresponds to a vertical section (see blue section in inset) through the phase prism at a constant mass fraction $\gamma_a = m_C/(m_C + m_A)$. In general a phase inversion from the $\underline{2}$ (Winsor I) state (oil-in-water microemulsion + excess oil) to the $\bar{2}$ (Winsor II) state (water-in-oil microemulsion + excess water) can be observed in nonionic microemulsions with increasing temperature. As can be seen, a one-phase region is formed at intermediate temperatures, i.e. between the emulsification failure boundary (efb) and the near critical boundary (ncb) which narrows with increasing mass fraction of oil $w_B = m_B/(m_A + m_B + m_C)$.

Temperature and composition exert not only a large influence on the phase behavior, but also on the shape and size of the aggregates formed [10, 47, 58]. Systematic studies in the last two decades revealed that upon increasing the temperature away from the efb, the droplets change from spherical to elongated to network like structures [10, 47, 82, 143]. Following the efb while increasing both temperature and the oil fraction w_B , the radius of the spherical droplets rise.

The concentration dependence of the Soret coefficient can be studied isothermally along the straight line binodal, i.e. keeping the oil-to-surfactant ratio constant (c.f. Figure 6.1 left).

In study of the thermal diffusion behavior of microemulsions contributions by water, microemulsion droplets and free surfactant molecules need to be considered. The influence of the oil can be neglected due to its low solubility. Conceptually, due to the different size of free surfactant and microemulsion droplets, we assume a ten times smaller Soret coefficient for the free surfactant molecules. As the number densities of surfactant molecules and microemulsion droplets are comparable, we would expect a 10% contribution by the free surfactant molecules. Due the fact that the concentration of the free surfactant molecules is in the order of the critical micelle concentration of 0.005 wt% [126], which is three orders of magnitude smaller than the droplet concentration, the contribution of the free surfactant molecules will not be observable in the measurement signal. Therefore we treat the microemulsion in the one-phase region as *pseudo-binary* system consisting of microemulsion droplets in water.

So far, there are only a few experimental studies on the thermal diffusion behavior of microemulsions and surfactant systems. Some studies [5, 122] emphasized the influence of the critical micelle concentration and others [146] focused on the size dependence of the thermal diffusion behavior. For instance Vigolo *et al.* found a linear dependence of the Soret coefficient on the radius which is in agreement with some experimental and theoretical findings [17] but contradicts other findings. [36, 39] So far there have only been concentration dependent measurements for surfactant systems [5] and hard colloids [89], but not for microemulsions. These measurements show a weak dependence of the Soret coefficient on the concentration below 10 vol% and a steep decrease of S_T at higher concentrations. Another interesting aspect is the interplay of the interfacial tension and the thermal diffusion behavior. Based upon an old physical picture by Ruckenstein [118], who argues that the force generated is caused by a gradient in interfacial tension similar to the Marangoni effect. Parola and Piazza [100] proposed a linear dependence of the Soret coefficient on the derivative of the product of the interfacial tension and some characteristic length with respect to temperature, which has been so far not experimentally investigated. Also in this respect it appears that microemulsions are excellent model systems, because they allow the experimental determination of the interfacial tension and a allow comparison with this model.

As mentioned above, a microemulsion is a dynamic system with adjustable properties, which allows study of the influence of various parameters on the thermal diffusion process. In our study we investigated three different experimental paths, which will be introduced briefly in

the following and are sketched schematically in Figure 6.1.

First, we used the $path_T$ to study the influence of structural changes by increasing the temperature starting close to the efb in the one-phase region and finishing close to the ncb at a fixed composition. Here we have to keep in mind that the temperature changes simultaneously. *Second*, along the $path_{w_B}$, i.e. close to the efb , the radius of the spherical microemulsion droplets grows with increasing oil content w_B . Also note that this path is not an isothermal one, i.e. here the temperature increases slightly. Along the *third* path, $path_\phi$, we study the dependence of the thermal diffusion on the volume fraction of droplets at the efb temperature, i.e. at isothermal conditions. Therefore, we increase the amount of oil and surfactant at a constant oil-to-surfactant ratio. Also these measurements are performed close to the efb in order to ensure that the microemulsion droplets are spherical. Furthermore, measurements of the temperature dependence of the interfacial tension allow us to discuss the Soret coefficient in the framework of the model proposed by Parola and Piazza. [95]

6.2 Experimental details and characterization

In this section we introduce the sample preparation and the experimental methods used. Furthermore we present the phase diagram of the chosen microemulsion system and the methods used to characterize their microstructure, i.e. dynamic light scattering (DLS) and small angle neutron scattering (SANS).

6.2.1 Experimental details

6.2.1.1 Sample preparation

The surfactant pentaethylene glycol monododecyl ether ($C_{12}E_5$, purity $\geq 99\%$) and *n*-decane (purity $\geq 99\%$) were both purchased by Sigma-Aldrich and used without further purification. The water was obtained from a Milli-Q[®] dispenser. The samples were prepared by weighting the appropriate amount of water, m_A (usually around 2 g) and then adding the required amount of surfactant (m_C) and afterwards the corresponding amount of oil (m_B). The target composition was achieved within an accuracy of 2 mg. The sample was then inserted into a bath of thermostated water to determine the phase behavior, i.e. the location of the phase boundaries on the temperature scale. In preparation for both DLS and thermal diffusion

measurements, the sample in the one-phase state was filtered with a Pall-Acrodisc[®] syringe filter with pore sizes of 0.8/0.2 μm . For the thermal diffusion measurements, the sample was filled into a quartz cell (Hellma[®]) with a thickness of 0.2 mm which was sealed by Teflon stoppers. Note that during the filling, the sample was in the single phase state and the sample cell was also kept at the sample temperature to avoid phase transitions. Finally, the cell was placed into a thermostated holder inside an infrared-thermal diffusion forced Rayleigh scattering (IR-TDFRS) setup [154].

6.2.1.2 Refractive index increments

To determine the refractive index increment with concentration $(\partial n/\partial c)_{T,p}$, we used an Abbé refractometer. Samples of different concentrations were repeatedly inserted into the refractometer at different temperatures over the necessary temperature range. Each refractive index value was determined at least five times. We measured the increment each in the vicinity around the sample concentration probed in thermal diffusion measurements. Typical values of $(\partial n/\partial c)_{T,p}$ spread from 0.110 to 0.116 with a deviation of $5 \cdot 10^{-5}$. The refractive index increment with temperature $(\partial n/\partial T)_{c,p}$ was obtained in an interferometric setup, upon measurement of the phase shift between the sample and the reference beam while the temperature of the sample was increased or decreased linearly over the typical measurement range. The range of $(\partial n/\partial T)_{c,p}$ goes from $1.20 \cdot 10^{-4}$ to $1.50 \cdot 10^{-4}$ with a typical deviation of $5 \cdot 10^{-6}$. The measurements were only conducted at the concentrations probed in the thermal diffusion measurements.

6.2.1.3 Dynamic light scattering

In dynamic light scattering (DLS) the intensity fluctuations were measured at a detector at a certain scattering angle θ which corresponds to a scattering wave vector $q = (4\pi n/\lambda)\sin(\theta/2)$, with the refractive index, n , and the wavelength, λ and are analyzed by a correlator (ALV-5000). We used a commercially available instrument (ALV/SP-86#059) with a Helium-Neon laser at a wavelength $\lambda = 633$ nm. The sample was prepared in a cylindrical sample tube, which was located in a thermostated toluene bath with $\Delta T \pm 0.05\text{K}$ temperature stability. The scattering intensity $I(q,t)$ was detected with a photomultiplier at angles $30^\circ \leq \theta \leq 150^\circ$ and was analyzed by the correlator card (ALV3000). Further processing was performed using the program package BATCON, which contains as an essential

feature the program package CONTIN [109] in order to extract the intensity autocorrelation function as well as the distribution function $A(\Gamma)$ of the inverse relaxation times Γ .

6.2.1.4 Small angle neutron scattering

SANS measurements were carried out using the instrument *KWS 1* at the *Jülich Centre for Neutron Science (JCNS)*, hosted at the *Research Neutron Source Heinz Maier-Leibnitz (FRM II)* in Garching, Germany. The samples were filled in Hellma[®] Quartz cells with an optical path length of 1 mm which were equilibrated to the desired temperature in a home-built cell holder with an accuracy of ± 0.05 K. The data were collected at wavelengths of $\lambda = 4.8$ and 12.0 \AA with a wavelength distribution of the velocity selector of $\Delta\lambda/\lambda = 0.2$ (full width at half maximum). Measurements were performed at sample-to-detector distances of 2 and 8 m, thereby covering a range of the scattering wave vector $q = (4\pi/\lambda)\sin(\theta/2)$ from 0.0036 to 0.33 \AA^{-1} . The collimation and aperture settings were chosen in order to optimize the neutron flux without exceeding the detector capacity. The raw data were radially averaged and normalized according to standard procedures using the program *QtiKWS*¹¹ provided by the *JCNS*. Plexiglas of 1.5 mm path length was used as absolute calibration standard.

6.2.1.5 Infrared-Thermal Diffusion Forced Rayleigh Scattering

The IR-TDFRS has been described in detail elsewhere [154]. Two infrared laser beams are crossed and create a sinusoidal interference grating. Due to absorption of the IR light by the aqueous sample, the intensity grating is transformed into a temperature grating. Within this grating, thermal diffusion forces the microemulsion droplets towards the cold side. The temperature and concentration changes lead to a modulation of the refractive index, which is probed by an additional readout laser. The alteration in the refractive index grating lead to a change of the intensity of this diffracted beam. The intensity changes as function of time were monitored by an avalanche diode. Note that the local heating of the sample cell due to the IR laser must be taken into account in order to compare the results with DLS, SANS and phase diagram measurements.

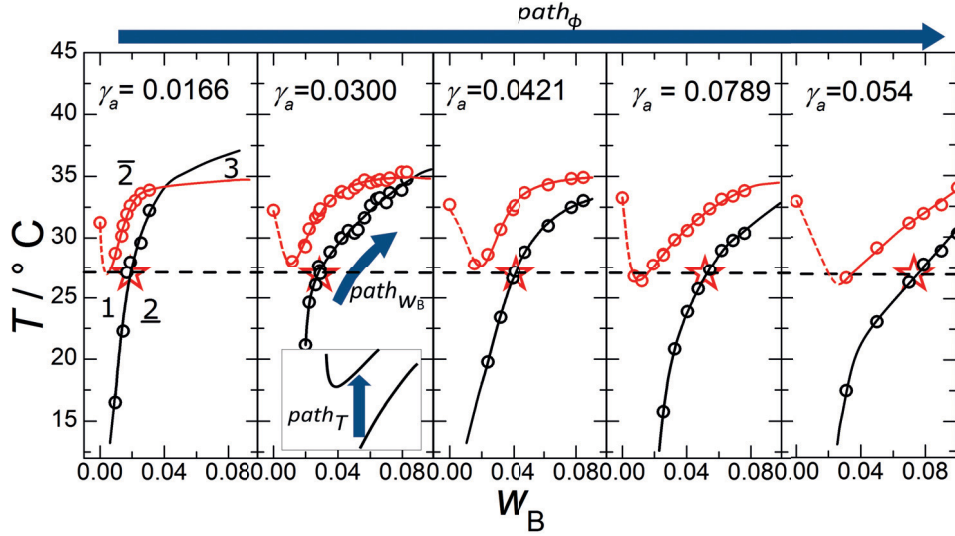


Figure 6.2: Phase diagrams of water/*n*-decane/ $C_{12}E_5$ at different γ_A as function of the oil content w_B . The chosen experimental paths are illustrated by the blue arrows $path_T$, $path_{w_B}$ and $path_\phi$. The inset shows the $path_T$. The $path_{w_B}$ denotes the path along the *efb* and the stars connected by the dashed line mark the isothermal measurement of $path_\phi$.

6.2.2 Characterization of the microemulsion system

6.2.2.1 Phase behavior

Figure 6.2 shows the phase diagram of the microemulsion system water/*n*-decane/ $C_{12}E_5$ for five different surfactant fractions γ_A as function of the oil content w_B . Transition temperatures between the two-phase and the one-phase regions, i.e. the *efb* and *ncb* have been measured for each composition. The number and kind of phases is determined by visual inspection in both transmitted and scattered light at a constant composition as a function of temperature [55]. For illustration purposes, the diagram includes also the experimental paths $path_T$, $path_{w_B}$ and $path_\phi$. The system water/*n*-decane/pentaethylene glycol monododecyl ether ($H_2O/C_{10}/C_{12}E_5$) was chosen to obtain uncharged aggregates, which exist close to room temperature. Note that due to the neutrality of the droplets, no electrostatic interactions need be considered. The size of the aggregates is expected to vary in a range from around five to up to ten nanometer. At low temperatures, a *n*-decane-in-water microemulsion coexists with a *n*-decane excess-phase ($\underline{2}$), while at high temperatures a water-in-*n*-decane microemulsion coexists with a water excess phase ($\bar{2}$). Between these two states, a one phase region (1) is found at intermediate temperatures. At a given temperature the maximum amount of *n*-decane that can be solubilized in the water-surfactant mixture is given by the ($\underline{2} \rightarrow 1$) emulsification failure boundary (*efb*). Upon comparison of the phase diagrams

recorded at different mass fraction γ_a of surfactant in the water/surfactant mixture, it becomes evident that an increase in γ_a allows solubilizing increasing amounts of n -decane w_B . Furthermore, with increasing γ_a , the minimum in the near critical boundary (ncb , $1 \rightarrow \bar{2}$) becomes wider. Note, that this minimum in the ncb is a consequence of an additional two-phase region in the form of a closed lobe appearing at temperatures below the three-phase region in the Gibbs triangle [57, 58, 60, 143]. Furthermore the efb -transition ($1 \rightarrow \underline{2}$) is kinetically hindered i.e. the sample stays in the one phase state for hours or up to days. We will come back to this point in the section describing thermal diffusion measurements below.

6.2.2.2 Microstructure

The microstructure of the system under study has been characterized before in some regions of the phase (diagram) space [10, 47, 82, 143]. For a quantitative correlation of the thermal diffusion behavior and microstructure we characterized the size and shape of the microemulsion structure by DLS and SANS measurements between the efb and ncb .

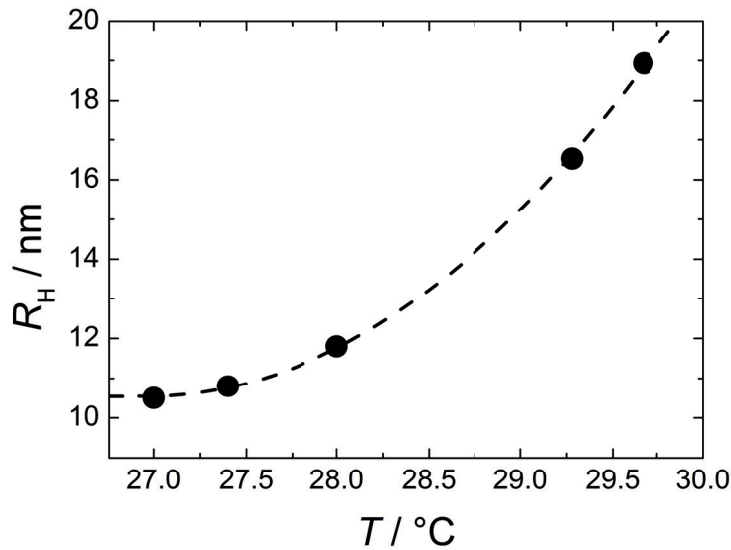


Figure 6.3: The hydrodynamic radius, determined by DLS-measurements, plotted against the temperature for the microemulsion $\text{H}_2\text{O}/n\text{-decane}/\text{C}_{12}\text{E}_5$ with $\gamma_a = 0.03$ and $w_B = 0.029$. The radius decreases with decreasing temperature until it reaches an almost constant value at the efb temperature at around 27°C .

Figure 6.3 shows the hydrodynamic radius R_H , which has been derived from the diffusion coefficient D (with the largest amplitude) using the Stokes-Einstein-relation for the system

$\text{H}_2\text{O}/n\text{-decane}/\text{C}_{12}\text{E}_5$ with $\gamma_a = 0.03$ and $w_B = 0.029$ at different temperatures. It can be seen that R_H increases with increasing temperature i.e. approaching the *ncb*. The analysis of the data using the Stokes-Einstein-relation, however, is only justified close to the *efb*, where the droplets are spherical. At higher temperatures it is known that the droplets elongate and form network-like structures close to the *ncb*.

This trend becomes clear upon consideration of the DLS distribution function $A(\Gamma)$, weighted by the relaxation time Γ as function of Γ in Figure 6.4. $A(\Gamma)$ is shown for 5 different temperatures between $T_{efb} = 27.00$ (a) and 32.00 °C (e) for three scattering angles $\theta = 30$ °(squares), 90 °(circles), and 150 ° (triangles), respectively. It is obvious, that the maximum of $A(\Gamma) \times \Gamma$ shifts to higher relaxation rates Γ with increasing scattering angle, corresponding to a translational mode with $\Gamma = 2q^2D$. Starting from the *efb* at $T = 27.00$ °C (c.f. Figure 6.4 a) and increasing the temperature up to $T = 28.00$ °C (c.f. Figure 6.4 b and c) the shape and position of the peaks remain almost unchanged (the dashed line is shown as guide to the eyes). While increasing the temperature from 28.00 °C to 29.67 °C (c.f. Figure 6.4e), the maximum of all three peaks shifts to smaller inverse relaxation times indicating a slower diffusion, which in turn points to the formation of elongated structures [49]. In the temperature range from 29.67 °C to 32.00 °C, the scattering is a superposition of the scattering from the formation of network structures and that from critical fluctuations, and the distribution function $A(\Gamma)$ broadens and shows additional modes. Hellweg and von Klitzing interpreted those additional modes in terms of the Zimm model used for the dynamics of worm-like polymers in solution [49].

Additionally, we conducted SANS measurements to confirm the spherical shape of the microemulsion droplets at the *efb* temperature. The experiment was performed in almost perfect film contrast for the microemulsion $\text{D}_2\text{O}/n\text{-D-decane}/\text{C}_{12}\text{E}_5$ with the same molecular composition as the DLS sample at $T = 26.09$ °C. The SANS scattering curve obtained after subtraction of the incoherent background scattering intensity is shown in Figure 6.5. The curve resemble the typical scattering pattern of spherical shells [48], i.e. the scattering intensity is almost constant at low values of the scattering vector q . Upon increasing q , the intensity decreases steeply until the first minimum is reached. The position of this minimum, which is followed by a small maximum, is related to the radius of the shells according to $q \sim \pi/R_0$. At large values of q the intensity decreases with a $\exp(-q^2t^2) \cdot q^{-2}$ dependence as a result of the diffuse nature of the amphiphilic film with an interface thickness t [48].

We described the experimental data using the form factor for polydisperse spherical Gaussian shells with diffuse interface and additional coherent scattering from the droplet core,

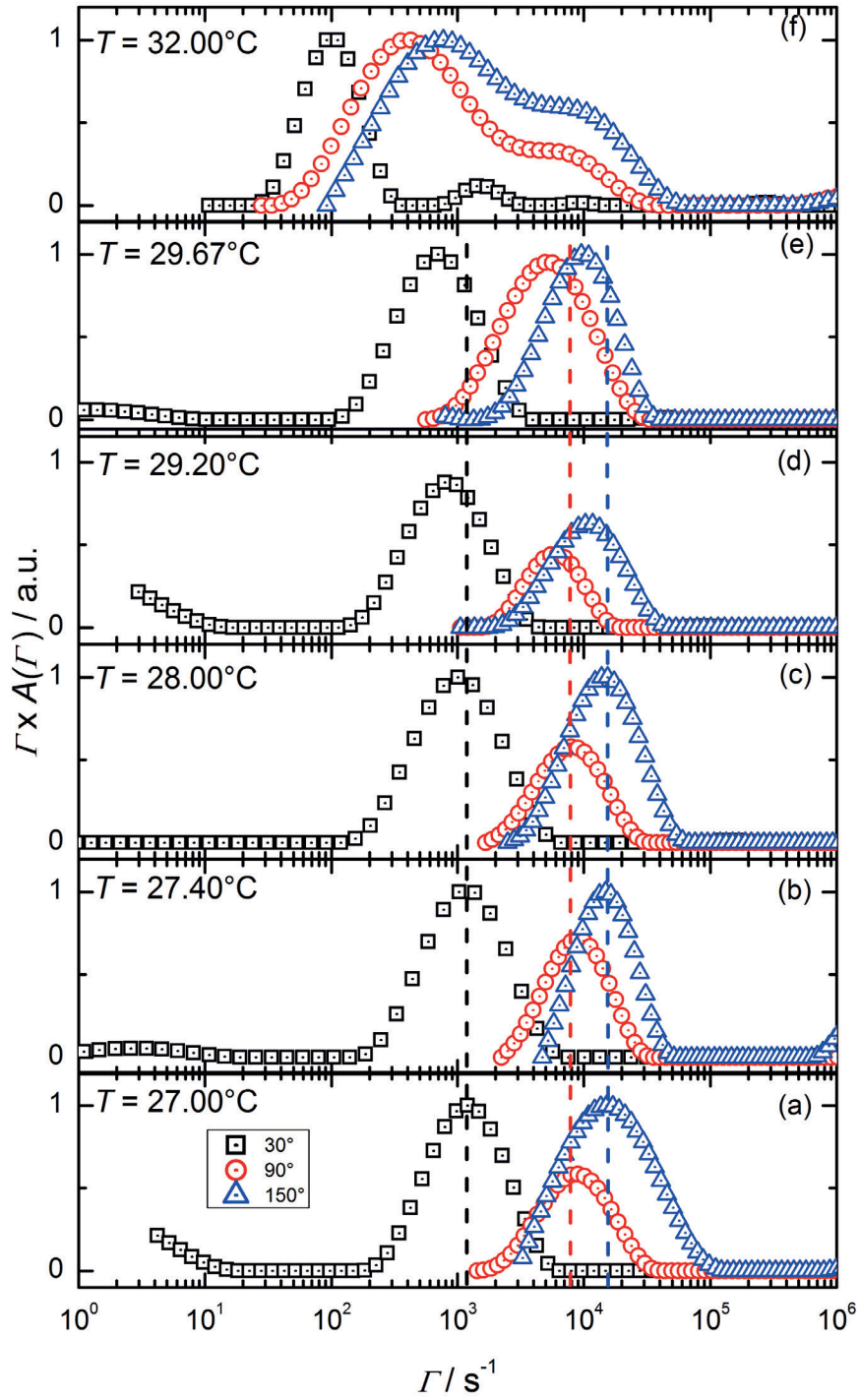


Figure 6.4: The distribution function $A(\Gamma)$ of the inverse relaxation time, weighted by Γ as function of Γ of the system $\text{H}_2\text{O}/\text{n-decane}/\text{C}_{12}\text{E}_5$ with $\gamma_a = 0.03$ and $w_B = 0.029$ at different angles.

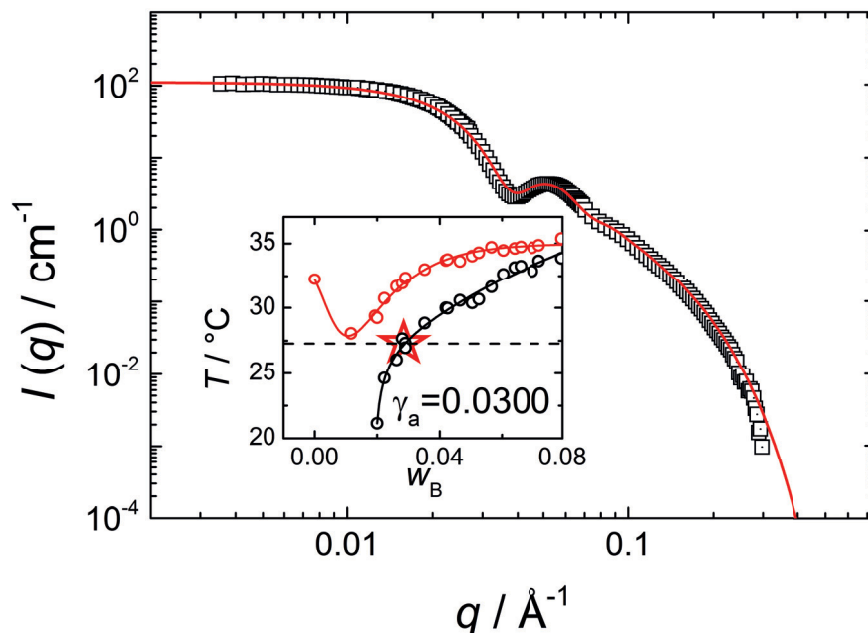


Figure 6.5: SANS curve of the microemulsion $H_2O/n\text{-decane}/C_{12}E_5$ with the same molecular composition as the DLS sample (c.f. Figure 6.3) to determine the size and shape of the microemulsion aggregates at the efb at $T = 26.09^\circ\text{C}$ (marked by the star in the phase diagram shown in the inset). Note, that the phase boundary is shifted to lower temperatures by $\Delta T \approx -1.5\text{ K}$ due to the replacement of H_2O by D_2O and $C_{10}H_{18}$ by $C_{10}D_{18}$. The scattered intensity is plotted versus the scattering vector q on a double-log scale. The almost constant intensity at small values of q indicate the existence of nearly spherical particles. The line represents a fit of a model for polydisperse shells. See text for details.

as derived by Foster et al. [43]. To account for excluded volume interactions we applied the structure factor of hard spheres with surface adhesion (sticky hard spheres) [9, 83]. The resulting curve is plotted in Figure 6.5. It can be seen that this model describes the experimental data almost quantitatively, which confirms that spherical microemulsion droplets exist at the efb. Thereby, a mean radius $R_0 = 8.1 \pm 0.25\text{ nm}$, a polydispersity $\sigma = 1.37\text{ nm}$ and a thickness of the diffuse amphiphilic film $t = 0.65\text{ nm}$ were obtained.

6.3 Results

Having characterized the phase behavior and microstructure of the chosen microemulsion system, the thermal diffusion properties were determined along three different paths using IR-TDFRS.

6.3.1 $path_T$: structure dependence

We obtained the diffusion, thermal diffusion and the Soret coefficient at the *efb* temperature by performing temperature dependent (isoplethal) measurements in the one-phase region, interpolating the determined data to the *efb*-temperature. As already mentioned, the transition from the one-phase region to the lower two-phase region is kinetically hindered, therefore we were also able to measure just within the two-phase region for hours before *n*-decane started to separate out. As a typical example, Figure 6.6 shows the temperature dependence of the diffusion D , the thermal diffusion D_T and the Soret coefficient S_T for a water/*n*-decane/ $C_{12}E_5$ microemulsion with $\gamma_a = 0.0421$ and $w_B = 0.03$, where the emulsification failure boundary (*efb*) is located at $T_{efb} \approx 23.0^\circ\text{C}$. Upon approaching the *efb*, the diffusion coefficient is almost temperature independent, which is in accordance with the DLS measurements (c.f. Figure 6.3). Starting at the *ncb*, the collective diffusion coefficient D increases linearly with decreasing temperature and approaches a constant value at the *efb* temperature. Upon considering the thermal diffusion coefficient, D_T , it first decreases and reaches a minimum at around 27°C . A further decrease of the temperature results in a steep increase of the thermal diffusion coefficient D_T until it reaches almost a plateau at low temperatures. Recall that near the *efb* temperature, the microemulsion droplets were found to be spherical and constant in size. The Soret coefficient S_T , the quotient of the thermal and collective diffusion coefficient, behaves similarly to the thermal diffusion coefficient. The decrease down from the *ncb* is steeper and S_T runs into a plateau already at temperatures somewhat above the *efb* ($T_{efb} \approx 23.0^\circ\text{C}$). The characteristic shape of the temperature dependence of the Soret coefficient S_T is similar for all microemulsions studied: Starting at the *ncb* it decreases steeply, runs through a minimum and reaches a plateau at or somewhat below the *efb* temperature. In the lower part of the one-phase region the elongation of the microemulsion droplets via coagulation indicate a slight weakening of hard sphere interactions, which might be responsible for the decrease of $S_T(T)$ as it has been observed for colloidal hard spheres [89]. At higher temperatures the increasing size of the structures dominates the behavior, so that $S_T(T)$ rises. Future studies must be undertaken to show whether the minimum of $S_T(T)$ and $D_T(T)$ at $T = 27.0^\circ\text{C}$ can be correlated with the elongation of rods or the formation of network structures.

6.3.2 $path_{w_B}$: size dependence

In order to study the dependence of the thermal diffusion properties on the radius of the spherical microemulsion droplets, we varied both the oil content and slightly varied the

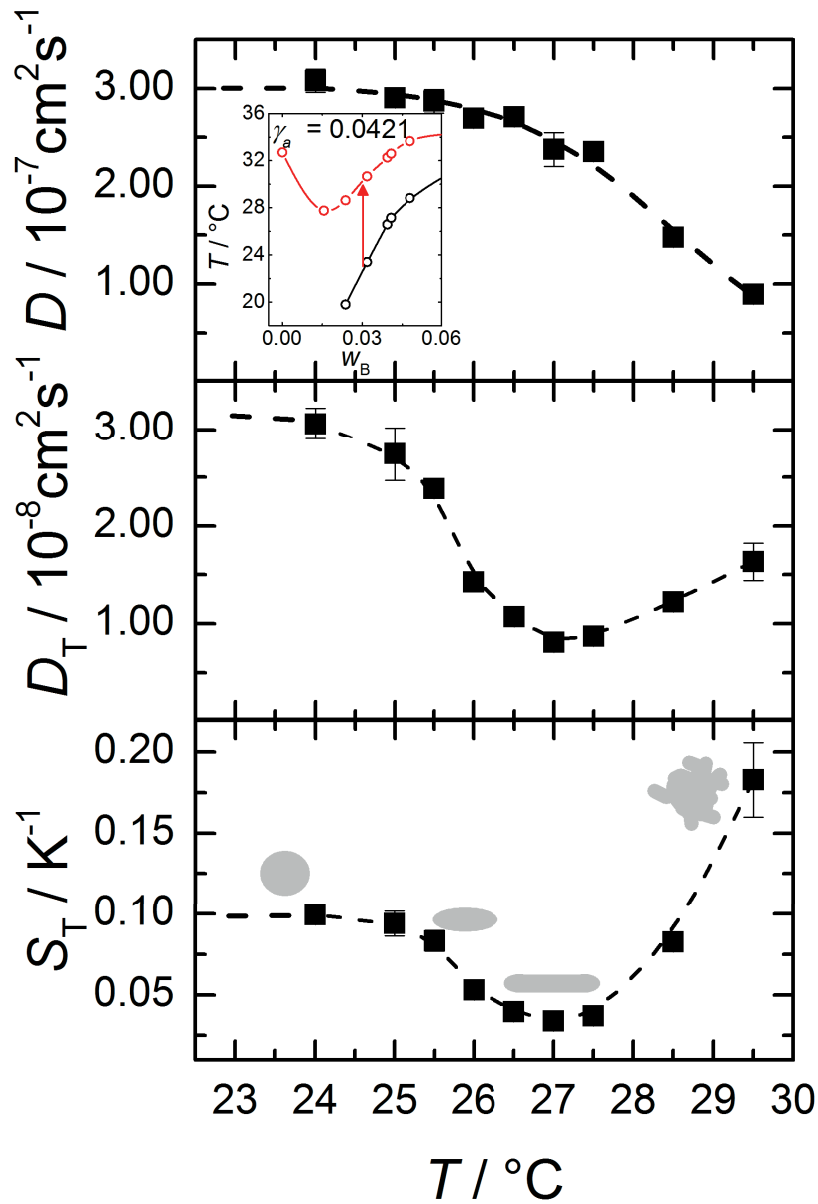


Figure 6.6: The diffusion D , thermal diffusion D_T and Soret coefficient S_T in the one-phase region at different temperatures ($\gamma_a = 0.0421$ and $w_B = 0.03$). The chosen experimental path is illustrated in the inset. The dashed lines are guides to the eye.

temperature, i.e. following the $path_{w_B}$ along the efb . In order to obtain the transport coefficients close to the efb , we measured the coefficients (as done for the $path_T$) at different temperatures and extrapolated the values towards the efb . Figure 6.7 shows D , D_T and S_T values at the efb obtained in this way.

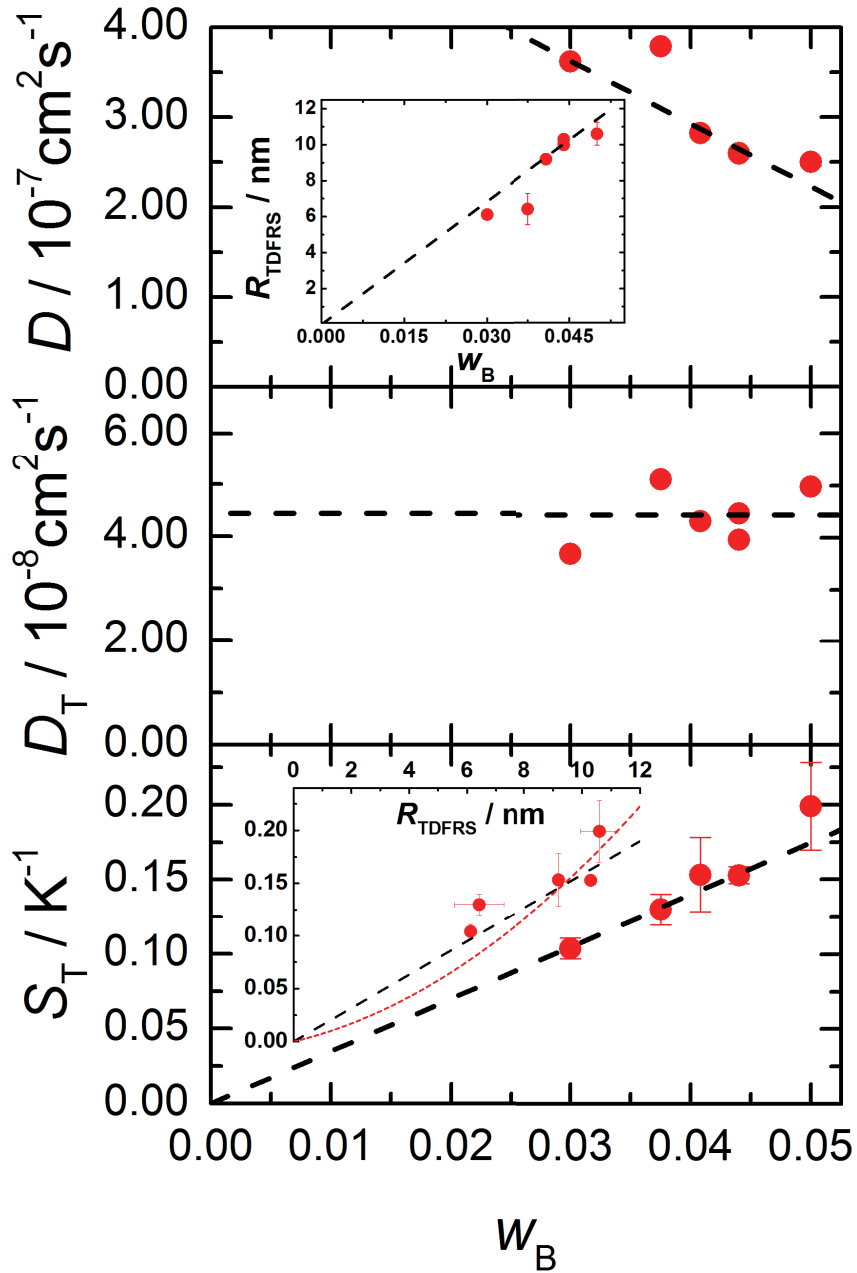


Figure 6.7: Measured diffusion, D , thermal diffusion, D_T and Soret coefficient, S_T at different mass fractions of oil w_B at a fixed $\gamma_a = 0.0421$ measured along the $path_{w_B}$. The upper inset shows the apparent radius, R_{TDFRS} , as function of the oil fraction. The lower inset displays S_T as function of the apparent radius, R_{TDFRS} , calculated from D using the Stokes-Einstein-relation. Linear and quadratic fits were performed by weighting the data points with their uncertainties. The corresponding efb temperatures rise from 23 °C to 28.5 °C with increasing w_B .

The diffusion coefficient, D , decreases with increasing mass fraction of oil, w_B , due to the growth of the microemulsion droplets. The inset illustrates the linear increase of the microemulsion droplets along the *efb*, by plotting the apparent radius R_{TDFRS} as function of w_B , whereas the line corresponds to a linear fit weighted by the uncertainty of the data points. Note, that the Stokes-Einstein-relation was used to determine the radius, R_{TDFRS} , which corresponds to a apparent radius similar to the one obtained by dynamic light scattering (R_H) with a slightly different weighting of TDFRS compared to DLS due to the polydispersity of the microemulsion droplets [59]. The thermal diffusion coefficient, D_T , is independent of the mass fraction of oil, while the Soret coefficient is linearly proportional to the oil fraction. For this rather small size range from 6 to 11 nm, a linear increase of S_T with R_{TDFRS} is observed. As shown in the inset of Figure 6.7, the data points follow a straight or quadratic line (weighted fit), which pass through the origin. The systematic deviations of the linear line are slightly smaller than in the quadratic fit. However, one should keep in mind that the S_T values correspond to different temperatures, i.e. the temperature increases from $T = 23^\circ\text{C}$ to $T = 28.5^\circ\text{C}$ with increasing oil content. Although the variation of the temperature is small, we cannot separate size and temperature effects.

6.3.3 *path* $_\phi$: volume fraction dependence

In order to study the concentration influence on the thermal diffusion behavior we performed a series of TDFRS experiments along *path* $_\phi$. As already mentioned in the introduction we do not expect a strong concentration effect below a volume fraction of 10%. As illustrated in Figure 6.1, we measured the Soret coefficient at the *efb* for different volume fractions of droplets. Along this isothermal path the volume fraction of surfactant and oil is increased keeping the oil/surfactant ratio and thus the radius constant. Figure 6.8 displays the extrapolated D , D_T and S_T values at the *efb* as a function of the volume fraction, ϕ , of microemulsion droplets. D shows a slight increase due to the effect of stronger interactions and thus shorter relaxation times. The thermal diffusion coefficient also increases slightly, but one order of magnitude less than D . The observed decay in the apparent radius (shown in the inset of Figure 6.8) calculated using the Stokes-Einstein-relation is probably related to stronger interactions at higher concentrations and not necessary due to an actual variation of the size of the microemulsion droplets [69], because SANS or static light scattering show that the radius of gyration, R_g , remains constant [8]. The Soret coefficient, S_T , decreases only slightly with the volume fraction, ϕ , of the droplets. This result agrees with results for colloids [89] and polymer solutions [112].

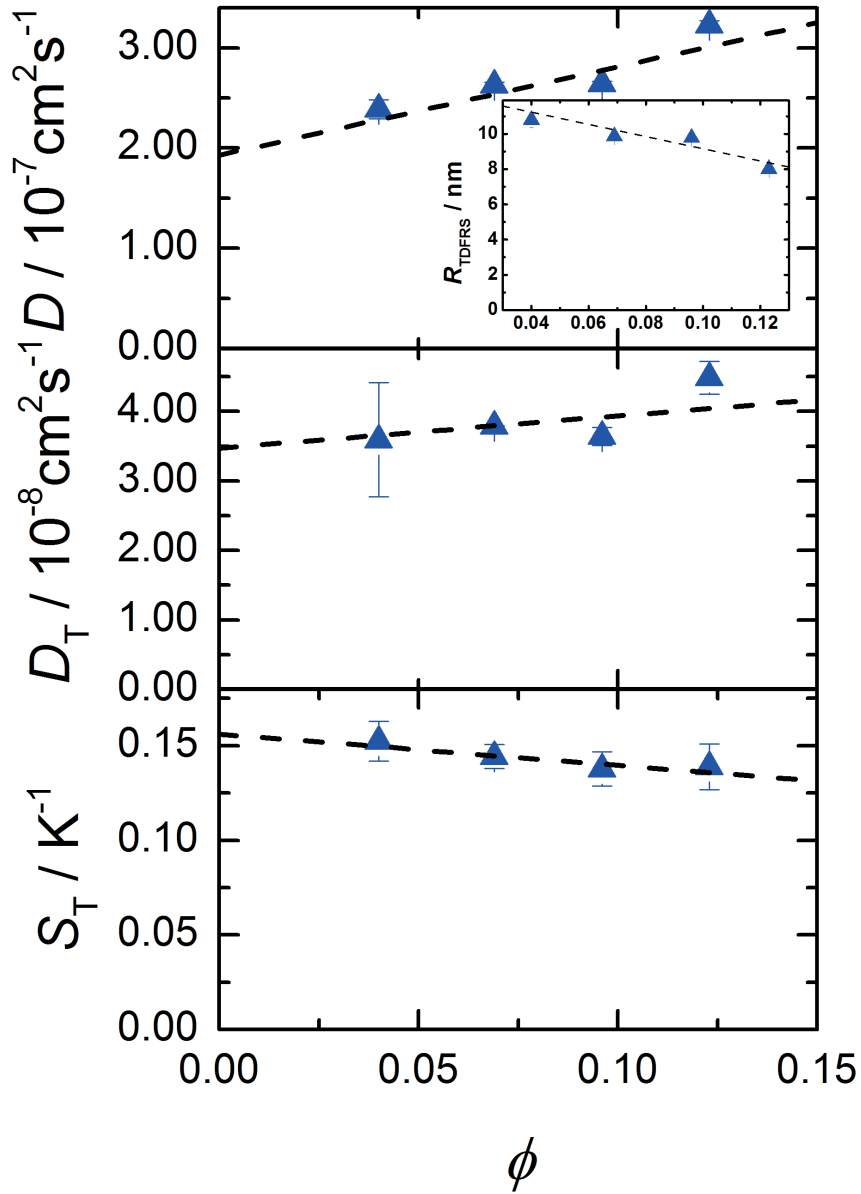


Figure 6.8: Diffusion, D , thermal diffusion, D_T , and Soret coefficients, S_T , measured at $T_{\text{efb}} \approx 27 \text{ }^\circ\text{C}$ for different volume fraction, ϕ , of the microemulsion droplets keeping the oil/surfactant ratio constant at 1/1. S_T decreases slightly with ϕ , which is related to the slightly different slopes of $D(T)$ and $D_T(T)$. The inset shows the apparent radius R_{TDFRS} as function of the volume fraction of the droplets. The dashed lines are linear fits, weighted with the uncertainties of the data points.

6.4 Discussion and Conclusion

Our main motivation for studying the thermal diffusion behavior of microemulsions is the chemical uniformity of the microemulsion droplets compared to colloidal particles. In the latter case, the grafting density of the chains attached to the surface of the colloidal particles for steric stabilization is usually not reproducible for each new synthesis. As a consequence the phase behavior of different batches varies often by ten and more degrees. Therefore, a comparison of the thermal diffusion data of colloids with different sizes becomes ambiguous. This is especially the case because the thermal diffusion responds strongly to interfacial effects [127]. Microemulsions allow a systematic variation of shape and size through temperature and concentration changes. Additionally, a direct measurement of interfacial properties such as the interfacial tension is possible, so that their influence on the thermal diffusion can be studied. A drawback of the microemulsions is that the change of one parameter often influences more than one property. We have chosen three different paths of temperature, oil amount and droplet volume fraction in order to get a meaningful picture for each scenario.

6.4.1 Structure and shape

Following the $path_T$, we monitor changes in the thermal diffusion behavior due to structural changes induced by temperature variation. We saw that the diffusion coefficient, D , reaches a plateau for temperatures at and below the emulsification failure boundary (c.f. Figure 6.3), and shows the typical critical slowing down, when the near critical boundary is approached [73, 153]. Note, that the calculation of the hydrodynamic radius using the Stokes-Einstein-relation is questionable due to network formation. The thermal diffusion coefficient D_T shows a minimum between the efb and ncb and increases towards the two boundaries. It has been theoretically predicted [73] and experimentally observed [46] that D_T remains constant upon approaching a critical point.

Similar to D_T , S_T also shows a minimum, but close to the efb S_T reaches a plateau, while the increase towards the ncb is rather steep. Theoretically [73] we expect that S_T diverges at the critical point. In the vicinity of the efb , the behavior of S_T coincides with the size of the droplets, which also becomes constant upon approaching the efb . Although the temperature changes by 2 K the Soret coefficient remains constant, which is an indication that S_T is mainly determined by the structure and not affected by temperature changes.

In order to investigate the size dependence we followed the $path_{w_B}$. In the investigated range, the radius changes only by a factor two. In this limited range the linear radial correlation

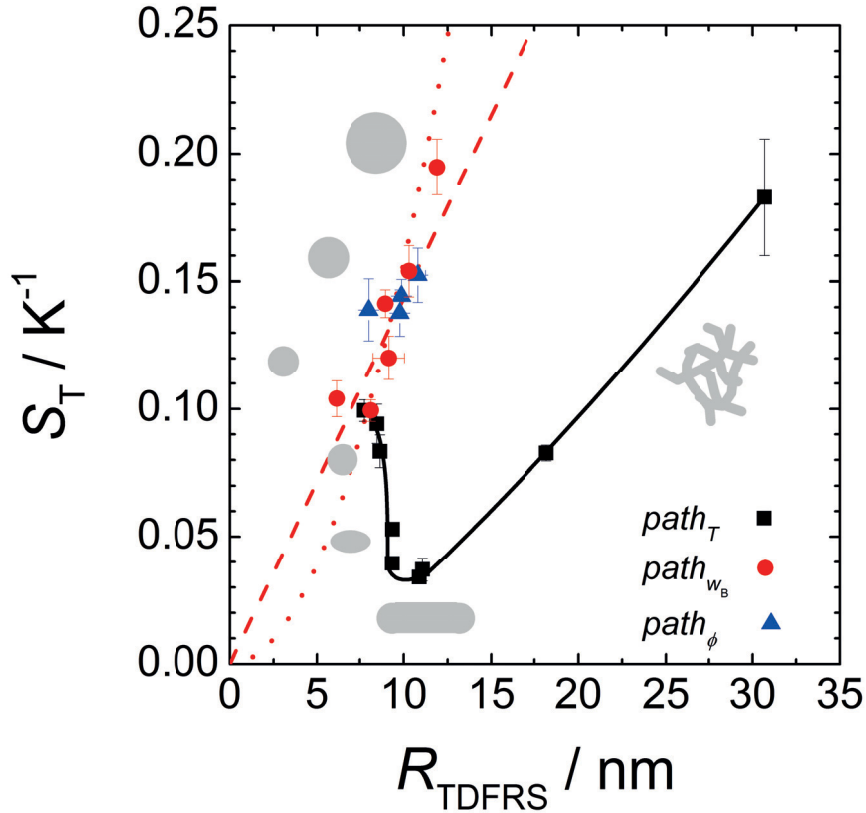


Figure 6.9: Soret coefficient as function of the apparent radius, R_{TDFRS} , measured along the path_T , path_{w_B} and path_ϕ . The path_T -line is a guides to the eye, while the path_{w_B} -data are fitted by a straight line (dashed) and a quadratic function (dotted) through the origin. Note, that R_{TDFRS} is calculated using the Stokes-Einstein-relation which assumes spherical aggregates, while it is known from DLS and SANS that the shape of the structure changes along path_T as illustrated by the grey pictograms.

of S_T is slightly better than the quadratic radial dependence (c.f. Figure 6.7). Conceptually the microemulsion droplets can be softer than colloidal particles. The exchange rate of the surfactant molecules between amphiphilic film and bulk is high. In such a case the interface of the microemulsion droplet could become permeable, so that a tangential velocity flow field intrudes in the microemulsion droplet [158]. This effect would lead to a quadratic radial dependence of S_T . To the best of our knowledge there are no experiments in the literature which measure the exchange kinetics of surfactant molecules for microemulsion droplets. Only the kinetics of the droplet exchange with typical relaxation times on the order of milliseconds, have been studied [42]. Also in micellar systems, a slow process has been observed with similar relaxation times on the order of milliseconds [142]. Additionally, the fast exchange of single surfactant molecules between micelles and water on the order of

microseconds has been resolved. However due to the large enthalpy penalty, direct water/oil contact is prevented by an amphiphilic film (characterized by a surfactant concentration at the interface, which is constant over time). Thus microemulsion droplets are expected to be fairly rigid. This picture is also supported by the linear radial dependence of the Soret coefficient found. Nevertheless, we have to keep in mind that the experimental range is quite small compared to other studies [17, 39, 111]. An expansion of the radial range might be possible by adding amphiphilic blockcopolymers, which leads to microemulsion droplets of about 100 nm in diameter [44].

Along $path_\phi$, the number density and temperature stay constant, but the volume fraction increases. The Soret coefficient decays by only 10% in the investigated concentration range, thus we can conclude that the increasing volume fraction along the $path_{w_B}$ will not influence the radial dependence of S_T . For higher volume fractions (above 10%) we expect a much steeper decay of S_T as it has been observed for micellar systems [5], colloidal suspensions [89] and polymer solutions [113].

Figure 6.9 summarizes the radial dependence of S_T measured along $path_T$, $path_{w_B}$ and $path_\phi$. While the data obtained along $path_{w_B}$ and $path_\phi$ scatter around a linear line, the data from $path_T$ deviate from the general trend. In this case the structural changes dominate the behavior. Especially in the regime, where the shape of the microemulsion droplets changes from spherical to elongated, we observe a decay of S_T with the apparent radius, R_{TDFRS} .

6.4.2 Interfacial tension

Our approach to understanding the S_T dependence is that of Piazza and Parola [95]. They relate the Soret coefficient of a colloid of radius R to the temperature derivative of the product of the oil/water interfacial tension σ_{ab} and a characteristic length l [95], which is related to the width of a fluid layer, where the pressure tensor is asymmetric [100], in the following way

$$S_T = \frac{4\pi R}{k_B T} \frac{\partial(l\sigma_{ab})}{\partial T}. \quad (6.2)$$

The physical picture behind this relationship dates back to Ruckenstein [118], who argues that a force is generated due to an interfacial tension gradient similar to the Marangoni effect. For the microemulsions under investigation the interfacial tension has been measured by Sottmann and Strey [133] by the so-called spinning drop method [148]. Figure 7.8 shows the interfacial tension as function of the temperature on a logarithmic scale. Below T_1

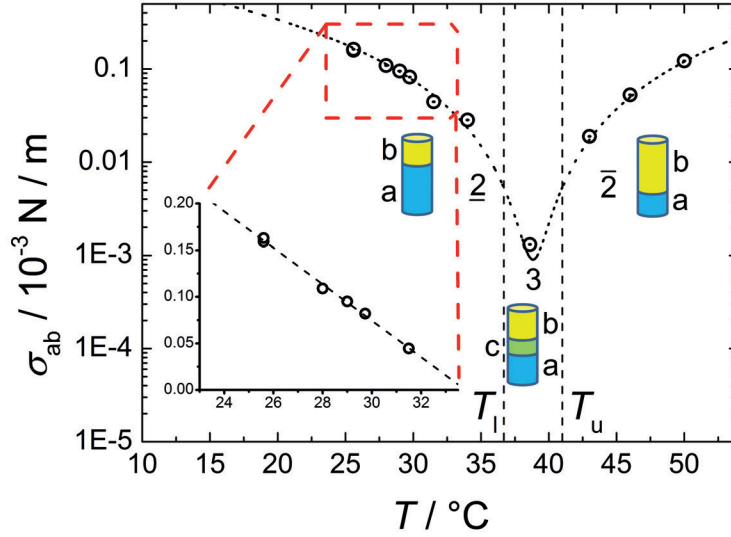


Figure 6.10: The oil/water-interfacial tension of the system water / *n*-decane / $C_{12}E_5$ as a logarithmic function of temperature. The inset shows the interfacial tension over the temperature range used in the thermal diffusion measurements. In this regions it shows an almost linear dependence.

the system phase separates into a o/w-microemulsion and an excess oil phase, while at temperatures above T_u w/o-microemulsions coexist with an excess water phase. Between T_l and T_u , where the oil/water-interfacial tension runs through a pronounced minimum three phases are formed [132].

The inset of Figure 7.8 shows the relevant interfacial tension data in the investigated temperature range on a linear scale. Over the entire temperature range a parabolic temperature dependence is expected [57, 70, 137], but in this limited range the temperature derivative is almost constant and equals to $\partial\sigma/\partial T = -0.0195 \cdot 10^{-3} \text{N K}^{-1} \text{m}^{-1}$. Due to the negative slope we also expect, according to Equation 7.12 a negative Soret coefficient, which is not found experimentally. For the moment we will use the absolute value of the derivative.

If we assume that the characteristic length l does not depend on temperature, we can determine l from the slope of a S_T versus $R \cdot (\partial\sigma_{ab}/\partial T)$ plot. The Soret coefficients and radii applied have been measured along the $path_{w_B}$ at the efb , which corresponds to the interfacial tension data. The data lie on a straight line (c.f. inset of Figure 6.11, top) and a short characteristic length of only $l = 0.3 \text{ nm}$ can be extracted. Using Equation 7.12 and the radial temperature dependence ($R_{TDFRS}(T) = -340 \text{ nm} + 1.16 \cdot T \text{ nm/K}$) as well as the interfacial tension derivative along the $path_{w_B}$ we can calculate S_T in dependence of T , which is plotted

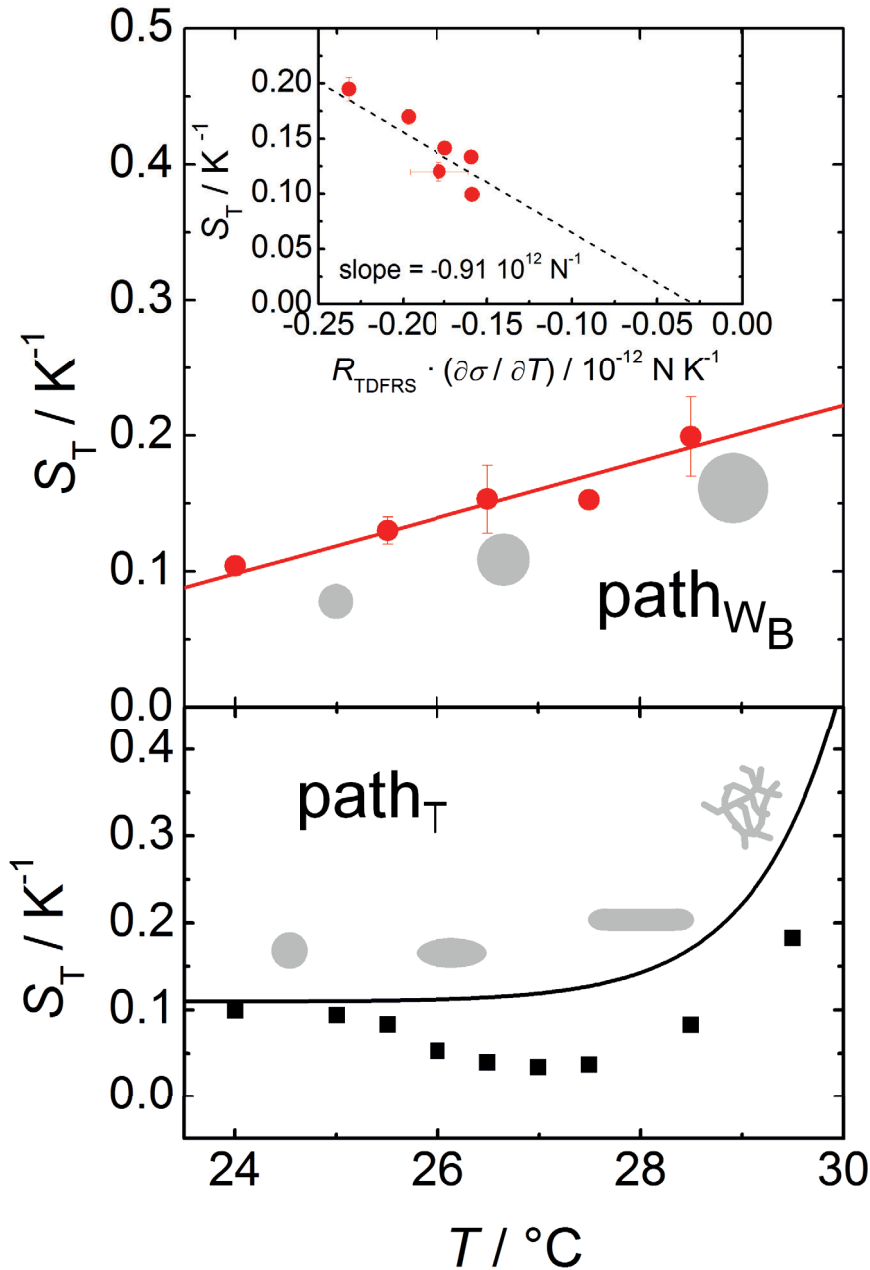


Figure 6.11: The inset in the upper part shows S_T as function of the product of the apparent radius, R_{TDFRS} and the temperature derivative of interfacial tension, which allows determination of the characteristic length from the slope of the plot. S_T , and R_{TDFRS} have been measured along the path_{WB} . The solid line represents the calculated Soret coefficient, S_T , according to Eq. 7.12 with temperature. The lower part shows the corresponding S_T -values calculated along path_T .

(line) in Figure 6.11, top. In this limited regime with spherical microemulsion structures we find a reasonable agreement. Additionally, we investigated whether this approach also works

along the $path_T$. Analyzing the temperature dependence of the hydrodynamic radius displayed in Figure 6.3 ($R_H(T) = 10.2\text{nm} + 0.7 \cdot e^{(1.2(T-27.5^\circ\text{C}))}\text{nm}$) in Equation 7.12 we can also predict the dependence of S_T with T along the $path_T$, which is plotted in Figure 6.11, bottom over the entire temperature range investigated. At high temperatures, the divergence of S_T is in qualitative agreement with the experimental data. However, only a shallow plateau is reached at lower temperatures. That the model does not provide the minimum (c.f. Figure 6.6) is not surprising upon taking into account that the relationship has been derived for isolated spherical colloidal particles, while here the structure of the microemulsion changes from droplets to network-like structures, which are not considered in the model. This shows that a more sophisticated model is required to follow structural changes in microemulsions.

ISOTHERMAL BEHAVIOR OF THE SORLET EFFECT IN
NONIONIC MICROEMULSIONS: SIZE VARIATION BY USING
DIFFERENT N-ALKANES

In this work we investigate the thermodiffusion behavior of microemulsion droplets of the type $\text{H}_2\text{O}/n - \text{alkane}/\text{C}_{12}\text{E}_5$ (pentaethylene glycol monododecyl ether) using the n -alkanes: n -octane, n -decane, n -dodecane and n -tetradecane. In order to determine the thermodiffusion behavior of these microemulsion droplets, we apply the infrared thermal diffusion forced Rayleigh scattering (IR-TDFRS) technique. We measure the Soret coefficient (S_T) as function of the structure upon approaching the emulsification failure boundary (efb) and as a function of the radius of the spherical o/w-microemulsion droplets close to the efb. By varying the chain length of the n -alkanes we are able to study the thermodiffusion behavior of droplets of different sizes at the same temperature. In the investigated range a linear dependence of the Soret coefficient as function of the radius was found. Using a proposed relationship between the Soret coefficient and the temperature dependence of the interfacial tension, the transition layer l could be determined for the first time. Additionally, small angle neutron scattering (SANS) experiments are performed to determine the size and to examine in

detail the shape of the microemulsion droplets, as the droplets are known to elongate with increasing temperature. Close to the efb the scattering curves could be quantitatively described by a combination of a spherical core-shell form factor and sticky hard sphere structure factor. *

7.1 Introduction

7.1.1 Thermodiffusion

Recently it has been demonstrated that thermal fields can be used to direct colloids and bio molecules to specific regions without requiring the use of lithographic structuring [152]. The underlying phenomenon is referred to as Soret effect. Thermodiffusion, akin to thermophoresis in colloidal dispersions, describes the mass transport in a mixture in the presence of a thermal gradient. A comprehensive microscopic description of the Soret coefficient S_T and the thermodiffusion coefficient, D_T , which can be expressed as the product of the mass diffusion coefficient, D , and, S_T , for liquids and colloidal dispersions is still not available. Many aspects such as the charge, mass, moment of inertia, size dependence have been investigated experimentally and theoretically, and empirical correlations or agreement with theoretical models have been found for specific systems such as alkanes [12] or charged colloids [91] [149] but a general microscopic understanding has not been reached yet. One of the open questions is the size dependence of S_T , whether it is linear or quadratic [100]. While Duhr and Braun [38] observed an unambiguous quadratic dependence of S_T for carboxyl modified polystyrene (PS) beads in 1 mM TRIS buffer of different radii in the range from 20 nm to 1000 nm using a microscopic fluorescence technique, studies by Putnam and Cahill of carboxyl functionalized PS spheres in a size range from 26 nm to 92 nm (PS) gave some indication that the behavior could also be linear. Later Vigolo et al. [146] obtained a linear dependence investigating bis(2-ethylhexyl)sulfosuccinate (AOT) / isooctane / water microemulsion droplets with a radius between 1.8 nm to 16 nm. Unfortunately the shape of the microemulsion droplets was not properly characterized, and thus it is not certain that the microemulsion droplets are spherical in the range of study. Simultaneously the decreasing surface charge density of the AOT system with increasing radius will change the electrostatic contribution to the thermodiffusion properties. Recently, Braibanti et al. [17] repeated the experiment of Duhr and Braun [38] and studied the thermodiffusive behavior

*The work described in this chapter is based on J. Chem. Phys. **118**, pp. 3451-3460 (2014)

of highly diluted carboxyl modified PS spheres under the same conditions except that they used a 1:1 mixture of $\text{H}_2\text{O}+\text{D}_2\text{O}$ to minimize sedimentation effects which can occur for the larger colloids. In the investigated radial range between 11 nm and 253 nm they found a linear size dependence for S_T . Also in theory the radial dependence is still controversially discussed. While Würger [158] expects a linear dependence for charged and uncharged solid colloids and only for soft colloids a quadratic size dependence of S_T , Dhont *et al.* [36] predict also for charged solid colloids a quadratic dependence.

Very recently we studied the thermodiffusion behavior of $\text{H}_2\text{O}/n\text{-decane}/\text{C}_{12}\text{E}_5$ following three different paths by changing the temperature, the oil content and the volume fraction of the microemulsion droplets and investigated the relation between the interfacial tension and the Soret coefficient [86]. Adjusting the appropriate concentration and temperature, a microemulsion forms discrete w/o- or o/w-aggregates, which are thermodynamically stable and can be used as colloidal model systems. Contrarily to synthesized colloidal particles, radius and interfacial tension can be easily varied by temperature or composition [137]. We found only very small concentration effects on the thermodiffusion behavior below a volume fraction of 10 %. By varying the oil content at a constant surfactant to water ratio we were able to change the size of the microemulsion droplets at the *efb*, but simultaneously we also had to vary the temperature slightly, so that the change in the Soret coefficient was not solely determined by size but also a temperature effect. In order to obtain microemulsions of different radius at isothermal conditions, in this work we studied the thermodiffusion behavior of microemulsion droplets by using different *n*-alkanes: *n*-tetradecane (*n*-C14), *n*-dodecane (*n*-C12), *n*-decane (*n*-C10), *n*-octane (*n*-C8) and a mixture (1:1) of *n*-octane/*n*-decane (*n*-C8/*n*-C10). Due to the fact that only the chain length of the *n*-alkane which is located in the inside of the (o/w)-droplets is changed, the surface properties are assumed to remain unchanged. Furthermore, we have chosen a nonionic surfactant to avoid charge effects.

We carefully characterized the phase behavior and studied the microstructure of the o/w-microemulsions by SANS to eliminate perturbing effects which comprise results from earlier publications. The typical phase behavior of the investigated microemulsion systems is sketched in Figure 7.1. At low temperatures a coexistence of an oil-in-water microemulsion and an oil excess phase (2) is found. With increasing temperature the so-called emulsification failure boundary (*efb*) is traversed and a thermodynamically stable, single phase microemulsion is formed. This one-phase region (1) closes like a funnel, when the *efb*, i.e. the capability of the surfactant to solubilize oil, intersects with the upper phase boundary (1-2̄). This phase boundary originates from the cloud point curve of the binary system $\text{H}_2\text{O}/\text{C}_{12}\text{E}_5$ and is therefore often denoted as a near critical boundary (*ncb*) [58].

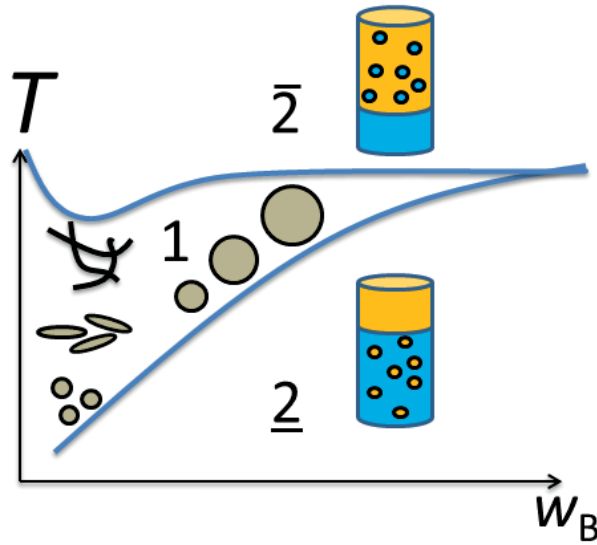


Figure 7.1: Schematic phase behavior of a water-rich microemulsion stabilized by a nonionic surfactant [58]. The phase boundaries are shown as a function of temperature and mass fraction w_B of the oil at a constant mass fraction γ_a of the surfactant in the mixture of water and surfactant. Between the lower emulsification failure boundary (efb) and the near critical boundary (ncb) a thermodynamically stable microemulsion is formed. Increasing the temperature results in a structural transformation from spherical droplets at the efb over elongated droplets to finally network like structures at the ncb before demixing occurs [10, 47, 82, 143]. Increasing the mass fraction of oil and temperature staying at the efb will yield larger microemulsion droplets.

In contrast to colloidal dispersions containing hard spheres, microemulsions form a soft interface between water and oil established by the surfactant layer. The interfacial tension is strongly dependent on the curvature of the amphiphilic film which is temperature dependent. Thermodiffusion has already been associated with the so called Marangoni effect [3]. In this work we are going to investigate the behavior compared to interfacial effects to find to which extent the interfacial tension influences the thermodiffusive behavior.

7.2 Experimental details and characterization

In this section we introduce the sample preparation and the experimental methods used. Furthermore we present the methods used to characterize the microstructure, i.e. dynamic light scattering (DLS) and small angle neutron scattering (SANS).

7.2.1 Experimental details

7.2.1.1 Sample preparation

The surfactant pentaethylene glycol monododecyl ether ($C_{12}E_5$, purity $\geq 99\%$) and the various n -alkanes (purity $\geq 99\%$) were each purchased by Sigma-Aldrich and used without further purification. The water was obtained from a Milli-Q dispenser. D_2O (purity $\geq 99\%$) and deuterated n -alkanes were acquired from Euriso-top. The samples were prepared by weighting the appropriate amount of water, m_A (usually around 2 g) and then adding the required amount of surfactant (m_C) and afterwards the corresponding amount of oil (m_B). The target composition was achieved within an accuracy of 2 mg. Identical compositions of protonated samples (phase behavior, DLS, TDFRS) and deuterated samples (SANS) were prepared with respect to molar fractions, i.e. volume fractions which are summarized in Table 7.1 and were calculated using the respective densities. The sample was then inserted into a bath of thermostated water to determine the phase behavior, i.e. the location of the phase boundaries. Both DLS and thermodiffusion samples were filtered in the one-phase state by a Pall-Acrodisc syringe filter with a pore size of $0.8 / 0.2 \mu\text{m}$. For the SANS measurements we used Hellma Quartz cells with an optical path length of 1 mm. For the IR-TDFRS measurements, the sample was filled into Hellma quartz cells with a thickness of 0.2 mm which was sealed with Teflon stoppers. Note that during the filling, the sample was in the single phase state and the measurement cell was also kept at the same temperature to avoid phase separation. Finally, the cell was placed into a thermostated holder inside an infrared-thermal diffusion forced Rayleigh scattering (IR-TDFRS) setup [154].

7.2.1.2 Refractive index increments

To determine the refractive index increment with concentration $(\partial n / \partial c)_{T,p}$, we used an Abbe refractometer by Anton Paar [150]. Samples of different concentrations were repeatedly inserted into the refractometer at different temperatures over the necessary temperature range. Each refractive index value was determined at least five times. We measured the increment each in the vicinity around the sample concentration probed in thermodiffusion measurements. Typical values of $(\partial n / \partial c)_{T,p}$ spread from 0.110 to 0.116 with an accuracy of $5 \cdot 10^{-5}$. The refractive index increment with temperature $(\partial n / \partial T)_{c,p}$ was obtained in an interferometric setup [157], upon measurement of the phase shift between the sample and the reference beam while the temperature of the sample was increased or decreased linearly over the typical measurement range. The value of $(\partial n / \partial T)_{c,p}$ varies between $1.20 \cdot 10^{-4}$ and

Table 7.1: Composition of the studied microemulsions. Given are the volume fractions of the surfactant Φ_C , the surfactant in the internal interface $\Phi_{C,i}$ and the oil Φ_B .

<i>n</i> -alkane	Φ_C	$\Phi_{C,i}$	Φ_B
<i>n</i> -C8	0.028	0.027	0.084
<i>n</i> -C8/ <i>n</i> -C10			
(1:1)	0.029	0.028	0.060
<i>n</i> -C10	0.029	0.029	0.040
<i>n</i> -C12	0.030	0.029	0.026
<i>n</i> -C14	0.030	0.030	0.017

$1.50 \cdot 10^{-4}$ with a typical accuracy of $5 \cdot 10^{-6}$. The measurements were only conducted at the concentrations probed in the thermodiffusion measurements.

7.2.1.3 Small angle neutron scattering

SANS measurements were carried out using the instrument *KWS 1* at the *Jülich Centre for Neutron Science (JCNS)*, hosted at the *Research Neutron Source Heinz Maier-Leibnitz (FRM II)* in Garching, Germany. Samples were filled in the Quartz cells which were equilibrated to the desired temperature in a home-built cell holder with an accuracy of ± 0.05 K. Data were collected at wavelengths of $\lambda = 4.8$ and 12.0 \AA with a wavelength distribution of the velocity selector of $\Delta\lambda/\lambda = 0.20$ (full width at half maximum). Measurements were performed at sample-to-detector distances of 2 and 8 m, thereby covering a wide range of the scattering wave vector $q = (4\pi/\lambda)\sin(\theta/2)$ with scattering angle θ . Collimation and aperture settings were chosen in order to optimize the neutron flux without exceeding the detector capacity. The raw data were radially averaged and normalized according to standard procedures using the program *QtiKWS* provided by the *JCNS*. Plexiglas of 1.5 mm path length was used as absolute calibration standard.

The experimental scattering curves was analyzed assuming a collection of spherical particles in solution. Applying the *decoupling approximation* [66] the scattering intensity $I(q)$ as function of the scattering vector q can be written as

$$I(q) = n P(q)S(q) + I_{Incoh}. \quad (7.1)$$

Therein the form factor $P(q) = [A(q)]^2$ is the square of the scattering amplitude A of the scattering particles and $S(q)$ is the structure factor describing the interaction of the particles.

n is the number density of the particles. Polydispersity is taken into account by convoluting the form factor with a *Gaussian* size distribution $W(R, R_0, \sigma)$ with the mean radius R_0 and the standard deviation σ . The scattering intensity is then given by

$$I(q) = n S(q) \int_0^\infty P(q, R) W(R, R_0, \sigma) dR + I_{incoh}. \quad (7.2)$$

In order to describe the experimental scattering data we used the form factor of a Gaussian shell with diffuse interface and core scattering [43], given by

$$P(q) = [A(q)]^2 = \Delta\rho_{core}^2 V_{core}^2 A_{core}^2(q) + \Delta\rho_{film}^2 V_{film}^2 A_{film}^2(q) + 2 \Delta\rho_{core} \Delta\rho_{film} V_{core} V_{film} A_{core}(q) A_{film}(q). \quad (7.3)$$

Hereby the scattering amplitude of the core is the well-known (normalized) amplitude of a homogeneous sphere [115]

$$A_{core}(q) = \frac{4\pi}{q^3 V_{core}} \{ \sin(qR) - qR \cos(qR) \}, \quad (7.4)$$

with V_{core} being simply the volume of a sphere with radius R . The scattering amplitude of the surfactant film was given by Gradzielski et al. [48]

$$A_{film}(q) = \frac{4\pi l_c}{q V_{film}} \cdot \exp\left\{ \frac{-q^2 t^2}{2} \right\} \cdot \{ q t^2 \cos(qR) - R \sin(qR) \} \quad (7.5)$$

with $V_{film} = 2\pi(4Rt^2 + l_c(t^2 + R^2))$ being the volume of the surfactant film. Thereby t is a measure for the thickness of the diffuse amphiphilic film and $l_c \approx v_c/a_c$ is the length of a surfactant molecule, given by the ratio of the volume v_c and the head group area a_c of the surfactant molecule. The contrasts are considered by the scattering length density differences $\Delta\rho_{core} = \rho_{bulk} - \rho_{core}$ and $\Delta\rho_{film} = \rho_{bulk} - \rho_{film}$, respectively. Including the polydispersity according to eq 7.2, the scattering intensity of the non interacting droplets ($S(q) = 1$) is expressed by

$$I(q) = I_{core}(q) + I_{film}(q) + I_{cross}(q). \quad (7.6)$$

The three contributions are given in large detail in reference 43. The free parameters of this model are the mean radius R_0 , the thickness of the diffuse amphiphilic film t and the standard deviation of the polydispersity distribution σ .

7.2.1.4 Dynamic light scattering

In dynamic light scattering (DLS) experiments the intensity fluctuations are measured at a detector at a certain scattering angle θ which corresponds to a scattering wave vector $q = (4\pi n/\lambda)\sin(\theta/2)$, with the refractive index, n , and the wavelength, λ . We used a commercially available instrument (ALV/SP-86#059) with a Helium-Neon laser at a wavelength $\lambda = 633$ nm. Cylindrical sample cells were chosen, which were placed in a thermostated toluene bath with a temperature stability of $\Delta T = \pm 0.05K$. The scattering intensity $I(q,t)$ was detected with a photomultiplier at angles $30^\circ \leq \theta \leq 150^\circ$ and was analyzed by the correlator card (ALV3000). Further processing was performed using the program package BATCON, which contains as an essential feature the program package CONTIN [109] in order to extract the intensity autocorrelation function as well as the distribution function $A(\Gamma)$ of the inverse relaxation times Γ .

7.2.1.5 Infrared-Thermal Diffusion Forced Rayleigh Scattering

The infrared-thermal diffusion forced Rayleigh scattering (IR-TDFRS) is optimized for aqueous systems and utilizes a weak absorption band of water in the infrared to create a temperature gradient. Details can be found elsewhere [13, 154]. Two infrared laser beams are crossed and create a sinusoidal interference grating. Due to absorption of the IR light by the aqueous sample, the intensity grating is transformed into a temperature grating. For all investigated microemulsions in this work thermodiffusion forced the microemulsion droplets towards the cold side. The temperature and concentration changes lead to a modulation of the refractive index, which is probed by an additional readout laser. The alteration in the refractive index grating leads to a change of the intensity of this diffracted beam. The intensity change as function of time were monitored by an avalanche diode. Note that the local heating of the sample cell due to the IR laser must be taken into account in order to compare the results with DLS, SANS and phase diagram measurements.

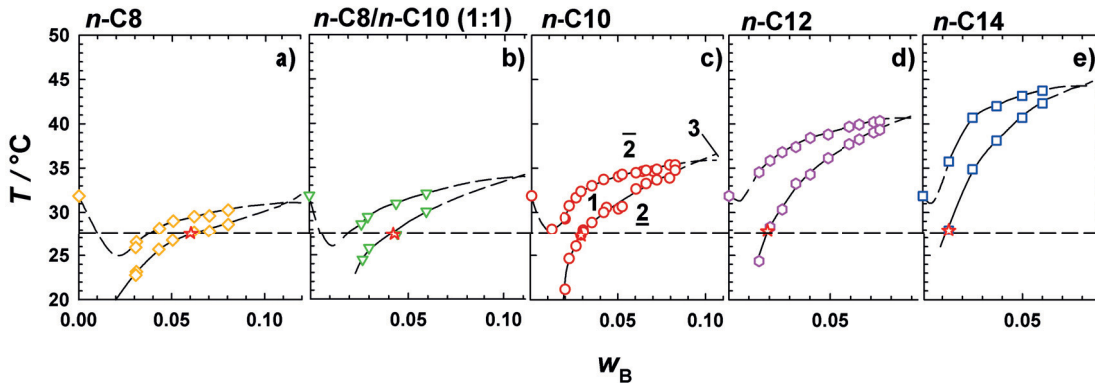


Figure 7.2: Phase behavior of water-rich microemulsion systems of the type H_2O/n -alkane/ $C_{12}E_5$ at a constant mass fraction of $C_{12}E_5$ in the $H_2O/C_{12}E_5$ -mixture $\gamma_a = 0.03$. The microstructure and the thermal diffusion behavior has been studied near the efb at $T_{efb} = 27.0 \pm 0.5$ °C (stars, connected by the dashed dotted line). Increasing the chain length of the n -alkane the one phase region shifts to higher temperatures. Concomitantly, the maximum amount of oil which can be solubilized at $T = 27.0 \pm 0.5$ °C decreases strongly.

7.3 Results

7.3.1 Phase behavior

The phase behavior of water-rich microemulsions of the type H_2O/n -alkane/pentaethylene glycol monododecyl ether ($C_{12}E_5$) is studied as a function of temperature and the overall weight fraction w_B of n -alkane at a constant ratio of $\gamma_a = m_C/(m_C + m_A) = 0.03$. Figure 7.2 shows the $T(w_B)$ -sections obtained using n -C8, n -C8/ n -C10 (1:1), n -C10, n -C12 and n -C14, respectively as n -alkanes. In all cases a sequence of phases is found that is typical for nonionic-microemulsion systems [58]. As can be seen, by decreasing the chain length of the n -alkane, the intersection point of the *efb* and *ncb* shifts to lower temperatures and larger weight fractions w_B . Comparing the maximum amount of n -alkane which can be solubilized at a constant temperature of $T_{efb} = 27.0 \pm 0.5$ °C, an increase by more than a factor of four is found as the chain length decreases (c.f. stars in Figure 7.2). Accordingly also the size of the droplets will increase, when the chain length of the oil is reduced.

7.3.2 Microstructure

The variation of the microstructure in the one-phase region of water-rich microemulsions has been both experimentally and theoretically studied [10, 47, 82, 143]. In order to ensure

the spherical shape of the o/w-microemulsion droplets and to determine their radius, small angle neutron scattering experiments were performed in close vicinity to the efb for each system at $26.1 \pm 0.4^\circ\text{C}$. Thereby film contrast conditions were tried to be adjusted by using adequate mixtures of protonated and deuterated n -alkanes in order to match the scattering length density of the droplet core with scattering length density of the surrounding D_2O ($\rho_{\text{bulk}} = \rho_{\text{core}}$). However, the quantitative analysis of the scattering data (see below) showed that $\rho_{\text{bulk}} \neq \rho_{\text{core}}$, i.e. that the scattering from the droplet core had to be taken into account. Obvious reasons for this mismatch are the fact that we did not include the monomeric solubility of the protonated surfactant in the n -alkanes [21] as well as undeuterated impurities in the deuterated species in the calculation of the scattering length densities ρ . The inset in Figure 7.3(a) shows the radial scattering length density profile exemplary by means of the n -octane microemulsion. As can be seen the scattering length densities of core and bulk are only slightly different. Furthermore, the parameter t (measure of the thickness of the diffusive amphiphilic film) which will be later on compared to the thickness l of the transition layer is schematically depicted. Note that the efb is shifted to $T_{efb} = 26.1 \pm 0.4^\circ\text{C}$ i.e. by 0.9 K to lower temperatures using deuterated instead of protonated solvents which is in agreement with literature [139]. The scattering curves obtained are shown in Figure 7.3 after subtraction of the incoherent background scattering intensity. All curves resemble the typical scattering pattern of spherical shells and a small fraction of core scattering [43], i.e. the scattering intensity is almost constant at low values of the scattering vector q . By increasing q the intensity decreases steeply until the first minimum is reached. At large values of q the intensity decreases with an $\exp(-q^2 t^2) \cdot q^{-2}$ dependence as a result of the diffuse nature of the amphiphilic film [48]. Comparing the scattering curves shown in Figure 7.3(b), it is evident that the position of the minimum, which is related to the radius of the shells ($R \sim \pi/q$) shifts systematically to lower values of q if the chain length of the solubilized n -alkane is decreased.

In Figure 7.3(a) the scattering curve of the microemulsion containing n -octane (n -C8) is exemplary shown. As can be seen, the description of the scattering data solely by the form factor given by eq 7.6 (represented by the dashed line), which neglects the contribution of any interaction (i.e. assuming $S(q) = 1$), led to higher scattering intensities at low values of q , which indicates the presence of inter-droplet interactions. These interactions are the largest for the n -C8 system, and become less significant for the microemulsions containing longer n -alkanes, i.e. with decreasing droplet volume fraction. In order to account for these interactions we used the structure factor of hard spheres with surface adhesion (sticky hard spheres) [9, 83]. Note, that the Percus-Yevick model for hard spheres could not describe

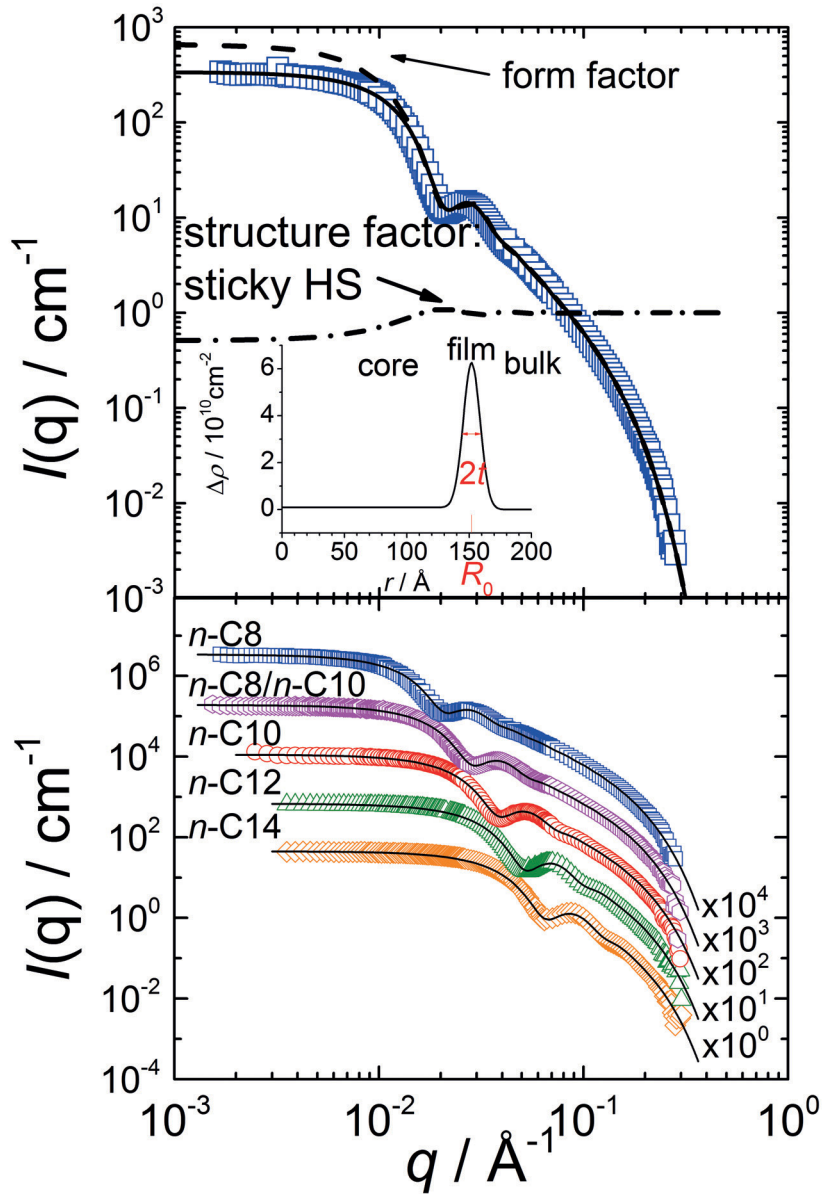


Figure 7.3: SANS measurement performed in film contrast to determine the size and shape of the microemulsion aggregates at the corresponding efb temperature. The scattered intensity is plotted versus the scattering vector q . The data are described by an appropriate combination of form- and structure factor. The inset in part (a) shows the radial scattering length density profile of the system *n*-octane. See text for details.

the scattering intensity quantitatively. The structure factor for hard spheres with surface adhesion (sticky hard spheres) [9] as given by Menon et al. [83] writes

$$S(x) = A^{-2}(x) + B^{-2}(x), \quad (7.7)$$

Where $x = aq$ with $a = \delta + \Delta$. δ represents the inner hard core diameter of the particle and Δ is the thickness of the attractive well of the potential of depth u_0 . Using this structure factor together with the core-shell form factor model (c.f. eq 7.6) Δ was set equal to t and a was set to $a = 2(R_0 + t)$ in order to reduce the number of free parameters. With the relative thickness of the attractive well $\varepsilon = \Delta/a$ the so called stickiness parameter τ of the potential is defined by

$$\tau = (12\varepsilon)^{-1} \exp(u_0/kT). \quad (7.8)$$

The terms $A(x)$ and $B(x)$ are given by

$$A(x) = 1 + 12\eta \left\{ \alpha \left[\frac{\sin(x) - x\cos(x)}{x^3} \right] + \beta \left[\frac{1 - \cos(x)}{x^2} \right] - \frac{\lambda}{12} \frac{\sin(x)}{x} \right\} \quad (7.9)$$

$$B(x) = 12\eta \left\{ \alpha \left[\frac{1}{2x} - \frac{\sin(x)}{x^2} + \frac{1 - \cos(x)}{x^3} \right] + \beta \left[\frac{1}{x} - \frac{\sin(x)}{x^2} \right] - \frac{\lambda}{12} \frac{1 - \cos(x)}{x} \right\}$$

with

$$\alpha = \frac{(1 + 2\eta - \mu)}{(1 - \eta)^2}, \beta = \frac{(-3\eta + \mu)}{2(1 - \eta)^2}. \quad (7.10)$$

and $\mu = \lambda\eta(1 - \eta)$.

$\eta = \phi_{\text{disp}} a^3/\delta^3$ is the effective volume fraction of the spheres and λ the smaller solution of quadratic equation

$$\lambda^2 - 12\left(\frac{\tau}{\eta} + \frac{1}{1 - \eta}\right)\lambda + \frac{12 + 6\eta}{\eta(1 - \eta)^2} = 0. \quad (7.11)$$

Accordingly the only free parameter of this model is the depth of the attractive potential well u_0 . Using the combination of both, form factor (dashed line) and structure factor (dashed-dotted line), the experimental scattering intensities could quantitatively be described for all systems. The parameters obtained are compiled in Table 7.2. As can be seen the radius R_0 of the microemulsion droplets increases from $R_0 = 4.7$ to $R_0 = 15.2$ nm if the chain length of the n -alkane is reduced. At the same time the polydispersity index $p = \sigma/R_0$ increases slightly from 0.15 to 0.18. The thickness t of the diffuse amphiphilic film was found to $t = 6$ Å for all microemulsion systems under study, i.e. independent of the chain length of the solubilized n -alkane. A somewhat smaller value of $t = 5$ Å was found for water-in-cyclohexane microemulsions stabilized by $C_{12}E_6$ [44]. Furthermore the depth of the attractive potential well u_0 becomes deeper, indicating that the effect of surface adhesion increases in case the chain length of the alkane decreases, i.e. the droplet radius is enlarged, via a weakening of the hydrogen bonds.

In order to monitor the size of the microemulsion droplets as a function of temperature we performed DLS measurements at different temperatures between the *ncb* and the *efb*. Figure 7.4 shows the hydrodynamic radius R_H , which has been derived from the diffusion coefficient D using the Stokes-Einstein relation for different temperatures. It can be seen that R_H increases with temperature approaching the *ncb* and for all temperatures the diffusion of the microemulsions aggregates becomes faster with increasing chain length of the n -alkanes. The analysis of the data using the Stokes-Einstein relation, however, is only justified close to the *efb*, where the droplets are spherical [49]. At higher temperatures it is known that the droplets elongate and form network-like structures close to the *ncb* [10, 47, 82, 143].

<i>n</i> -alkane	R_0 nm	σ nm	t nm	ε	η	$-u_0$ kT
<i>n</i> -C8	15.2 ± 0.3	2.8	0.6	0.021	0.117	1.52
<i>n</i> -C8/ <i>n</i> -C10 (1:1)	11.0 ± 0.3	1.9	0.6	0.029	0.095	1.23
<i>n</i> -C10	8.1 ± 0.2	1.3	0.6	0.037	0.077	0.91
<i>n</i> -C12	6.0 ± 0.1	0.9	0.6	0.049	0.064	0.76
<i>n</i> -C14	4.7 ± 0.1	0.7	0.6	0.061	0.057	0.67

Table 7.2: Fit parameters of the form and structure factor applied to describe the SANS curves of the water-rich microemulsions D_2O/n -alkane/ $C_{12}E_5$ with the composition given in Table 7.1 at $T_{efb} = 26.1 \pm 0.4^\circ C$ (Note that the temperature in SANS experiments was slightly lower due to the deuterated solvents). The mean droplet radius R_0 , standard deviation of the polydispersity distribution σ , thickness of the diffuse amphiphilic film t , rel. thickness of the attractive potential well $\varepsilon = \Delta/a = t/(2R_0 + t)$, effective droplet volume fraction $\eta = \Phi_{disp} a^3/\delta^3 = \Phi_{disp} ((2R_0)/2(R_0 + t))^3$ and potential depth u_0 .

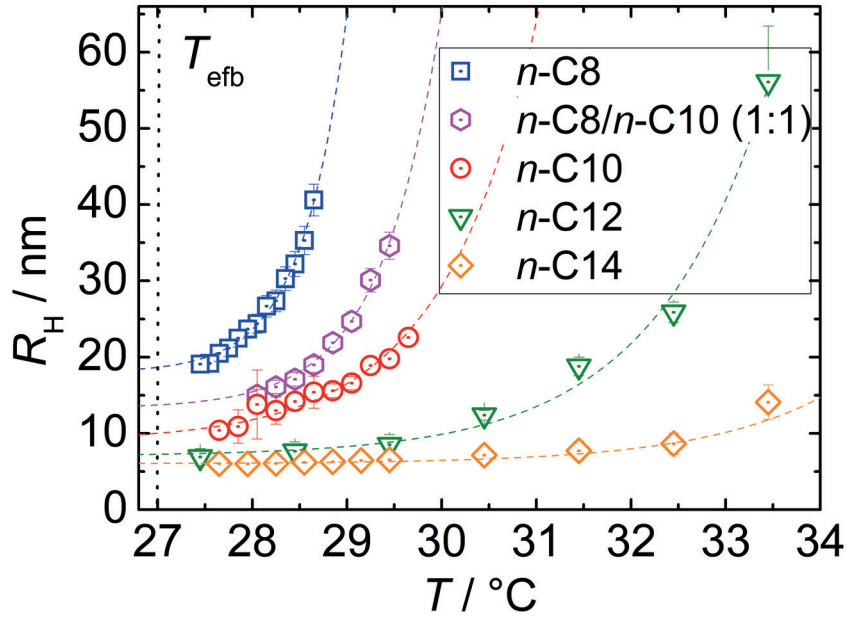


Figure 7.4: Hydrodynamic radius, R_H , as function of temperature for microemulsion with various *n*-alkanes and *n*-alkane mixtures determined by DLS. The composition of the samples is given in Table 7.1.

7.3.3 Thermodiffusion behavior

We studied the thermodiffusion behavior of the microemulsions with n -C8, n -C8/ n -C10 (1:1), n -C10, n -C12 and n -C14 as function of the temperature in the one-phase region and as function of w_B by changing the oil component at constant temperature. As illustrated in Figure 7.2 we can compare the measurements for different n -alkane microemulsions at the same efb temperature, which ensures, as shown by SANS, spherical droplets with different sizes depending on the chain length of the n -alkane. At this point we assume that the interactions between the microemulsion droplets are dominated by the surfactant molecules.

7.3.3.1 Temperature dependence

In order to study the temperature dependence we performed measurements within the one-phase region, above the efb and below the ncb [86]. The transition from the one-phase region to the lower $\underline{2}$ -phase region is kinetically hindered, so that measurements in the $\underline{2}$ -phase region were possible before the phase separation sets in. Figure 7.5 shows the collective diffusion D , thermodiffusion D_T and Soret coefficient S_T in the one-phase region for the five microemulsions under study as function of temperature. The diffusion coefficient D shows two linear regimes with different slopes. It increases significantly, when the temperature is lowered, because the droplets become smaller and almost spherical in shape. For n -tetradecane the thermodiffusion coefficient D_T first reduces with cooling down from the ncb and reaches a minimum. Further decrease of temperature results in a steep increase of the thermodiffusion coefficient D_T until it becomes almost constant for temperatures close to the efb . To be remembered, in this temperature range, the microemulsion droplets are spherical and constant in size. The Soret coefficient S_T , the quotient of the thermal and collective diffusion coefficient, behaves almost like the thermodiffusion coefficient. Decreasing the temperature from the ncb , S_T decreases steeply going through a minimum and a plateau value is reached just below or in the vicinity of the efb temperature. Also for the shorter n -alkanes we would expect a minimum as it was observed for n -C14, but due to the smaller width of the one-phase region it was difficult to detect. Especially for the microemulsion containing tetradecane it is obvious that the value of S_T is constant for a rather wide temperature range of 3-4 Kelvin, because the particle radius does not change. It seems to be likely that the transition from a network structure to individual droplets corresponds to a minimum in the thermodiffusion properties.

The measurements of the n -C8 system were complicated due to a very narrow one-phase region, so that the range in which spherical droplets exist was rather small and additionally

the volume fraction of the droplet concentration was already 11.7 %. But in the earlier work we have shown, that interaction effects can still be neglected [86] and the thermodiffusive behavior is mainly determined by size effects and not by interactions.

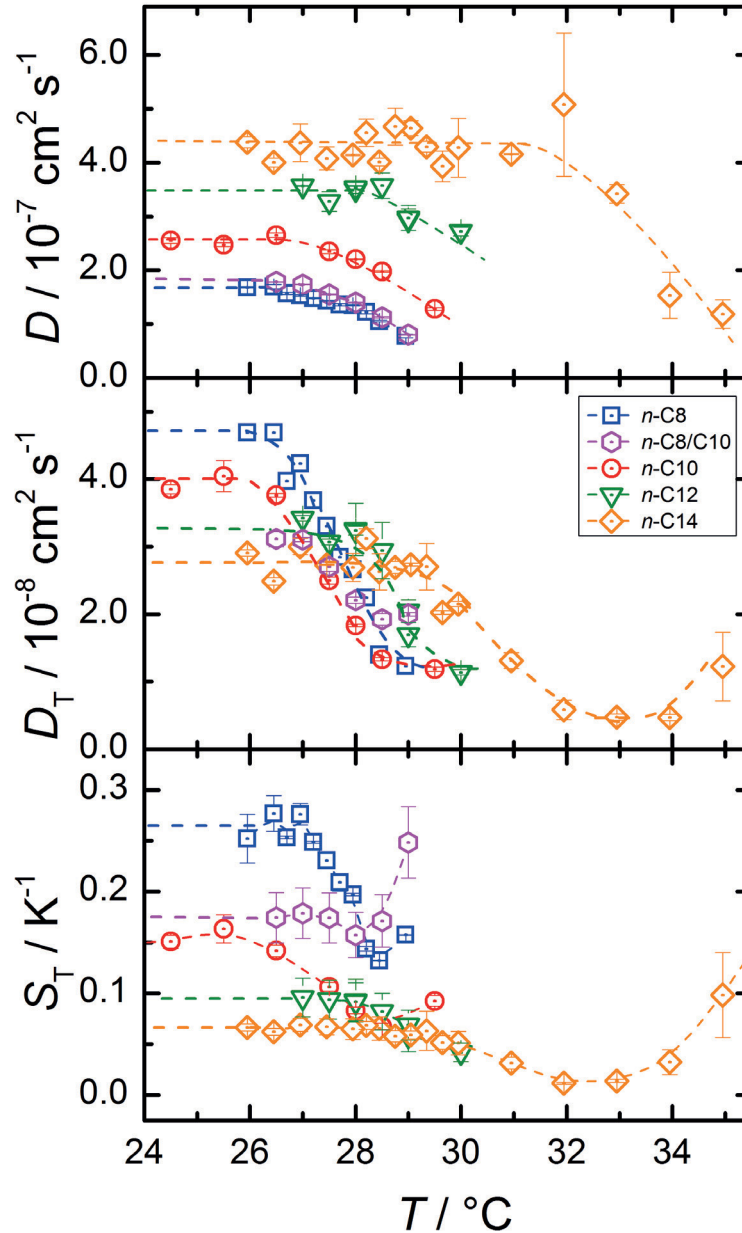


Figure 7.5: The diffusion D , thermodiffusion D_T and Soret coefficient S_T as function of temperature. The five microemulsion systems (compositions are given in Table 7.1) are studied in the one-phase region. We used the same symbols as in Figure 7.2, 7.3 and 7.4 and the dashed lines are guides to the eye.

7.3.3.2 Size dependence

As mentioned above in this work we study the radial dependence of the thermodiffusion properties of microemulsion droplets at a constant temperature of $T = 27.0^\circ\text{C}$ by varying the n -alkane chain length from n -tetradecane down to n -octane. To obtain the transport coefficients close to the *efb*, we extrapolated the values measured as function of temperature towards the *efb*. Figure 7.6 shows the extrapolated D , D_T and S_T -values for the five microemulsions with different oil components as function of $R_{\text{SANS}} = R_0 + t$ which corresponds to an apparent smaller radius compared to the one obtained by dynamic light scattering (R_H).

The diffusion coefficient, D , decreases with increasing radius of the microemulsion droplets. The thermodiffusion coefficient, D_T , seems independent of the droplet radius, while the Soret coefficient is proportional to the radius. For this size range from around 5 to 16 nm, a linear increase of S_T with R_{SANS} with a slope of $0.016 \text{ K}^{-1}\text{nm}^{-1}$ is observed.

Compared to the approach we used for the n -decane system [86] we could avoid a simultaneous change of the temperature, while the radius is varied. As seen in Figure 7.2, we increase the oil fraction and thus the radius but keeping the *efb* temperature constant. On the other hand the drawback of this scenario is different oil components, which modify the core of the microemulsion droplets. But due to the fact that we use only linear n -alkanes, which vary rather regularly [12] and have similar interactions with the surfactant molecules we do not expect an influence on the thermodiffusion. This would probably be different if we would use branched alkane isomers, because for those systems a clear dependence of the thermodiffusive behavior on the structure has been reported [105].

7.3.4 Interfacial tension

Already from the early works by the Giddings group [71] it is known that the surface groups of colloidal particles change the thermodiffusion behavior substantially, indicating that the interface between the solute particle and the solvent is an important factor. Later Piazza and Parola [95] related the Soret coefficient of a colloid with radius R to the temperature derivative of the product of the interfacial tension σ_{ab} and a characteristic length l [95], which has been initially related to the interaction range between the colloid and the solvent and later to the width of a fluid layer, where the pressure tensor is asymmetric [100], in the following way

$$S_T = \frac{4\pi R}{k_B T} \frac{\partial(l\sigma_{\text{ab}})}{\partial T}. \quad (7.12)$$

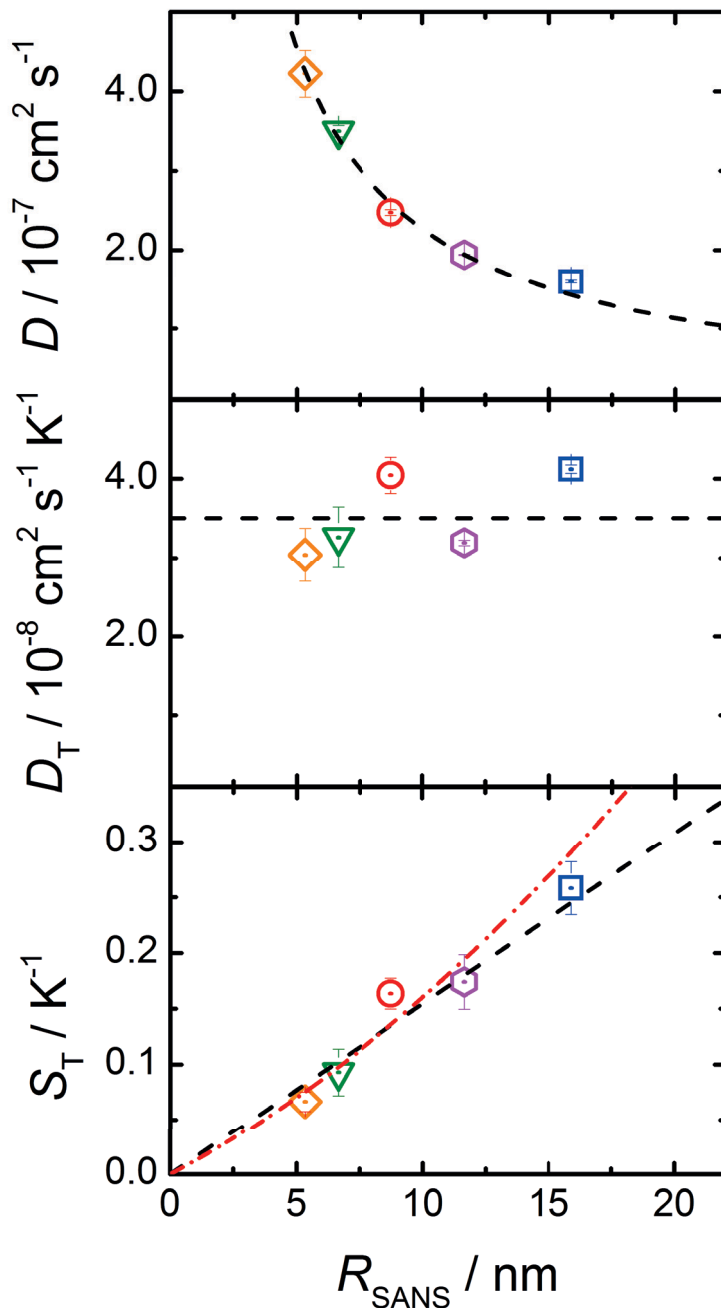


Figure 7.6: The diffusion D , thermodiffusion D_T and Soret coefficient S_T for the five microemulsions under study extrapolated to the efb-temperature of 27.0°C as function of $R_{\text{SANS}} = R_0 + t$ with the core radius R_0 and the thickness of the diffuse amphiphilic film t . We used the same symbols as before. For D the black line is a $1/R_0$ fit, for D_T it is a constant and for S_T the black line is a linear fit and the red dash dot line is a parabolic fit.

Applied to the systems under study this equation might be understood intuitively with the help of Figure 7.7, which schematically shows the microemulsion droplet in a temperature

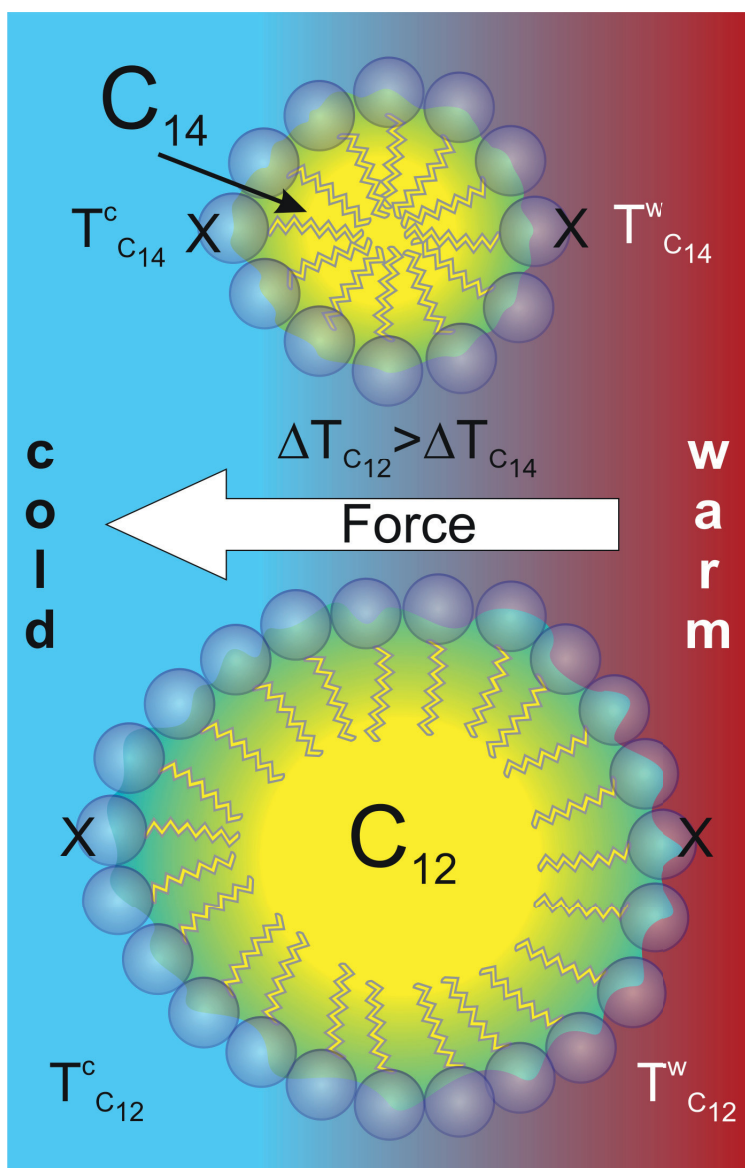


Figure 7.7: A qualitative illustration of eq 7.12. Exemplarily we show schematically two microemulsion droplets solubilizing *n*-tetradecane and *n*-dodecane, respectively. The blue circles represent the hydrophilic headgroups. Due to the larger droplet size for the shorter oil the temperature difference between both sides of the droplet marked by "x" is also larger. Further details see in the text.

gradient. Inside it contains the oil and the interface between water and the oil is formed by a surfactant layer, which is partially penetrated by oil and water from the in- and outside, respectively. The force acting on the soft colloid depends on the distance $2R$ between the two points marked by "x" lying in the warm and cold region. According to eq 7.12 we expect a larger S_T in the case of *n*-octane due to its larger droplet size, which is confirmed in

Figure 7.6 (bottom). Additionally, the thermophoretic force depends also on the temperature dependence of the interfacial tension σ_{ab} and the thickness l . The change of the interfacial tension with temperature is indicated in Figure 7.7 by a slight asymmetry of the droplet (c.f. droplet with n -dodecane). The increasing interfacial tension σ_{ab} with decreasing temperature leads to a higher curvature equal to a smaller radius on the cold side. As already mentioned the definition of l is ambiguous, sometimes [95] it is interpreted as a measure of the range of the colloid-solvent interaction and otherwise [100] as the width of the fluid layer with an anisotropic pressure tensor also denoted as transition layer. Regarding the range of interactions and considering only short range van der Waals interactions we expect l in a range of 1-2 Å. If we follow the fluid layer argument it might be possible to identify l with the thickness of the diffuse amphiphilic film t in the order of 6 Å.

Accordingly, we expect a larger S_T with a growing particle radius, R , and an increasing temperature sensitivity of the interfacial tension σ_{ab} and the thickness l . Due to the almost linear dependence of S_T on the radius both dependencies almost cancel out.

Based on this approach we compared in a recent study the interfacial tension data of the n -decane microemulsion with the measured Soret coefficients [86] and found some consistency with this approach. Now we can extend our comparison to microemulsions containing different n -alkanes. Most of the interfacial tension data have been measured by Sottmann and Strey [133] by the so-called spinning drop technique [148]. In this study we measured the interfacial tension of the system n -C8/ n -C10 (1:1) in the relevant temperature regime between 25.49°C and 29.55°C. To validate our data we additionally repeated some of their data points. Figure 7.8 shows the interfacial tension as function of the temperature on a logarithmic scale and in the inset on a linear scale. The oil/water-interfacial tension is known to run through a pronounced minimum at the phase inversion temperature of the respective system [132].

While over the entire temperature range a parabolic temperature dependence is found [57, 70, 137], the temperature derivative stays almost constant in the investigated range. In the inset it becomes obvious that the temperature derivative of the interfacial tension is negative and varies with the chain length of the n -alkanes. The absolute value increases with the chain length of the n -alkane, so that forces generated due to the difference in the interfacial tension become larger, but simultaneously also the radius of the droplet decreases (c.f. Table 7.3 and 7.2). According to eq 7.12 we expect a negative Soret coefficient, which is not found experimentally, so that we consider in the following only the absolute value of $(\partial\sigma_{ab}/\partial T)$.

If we assume that the thickness of the transition layer l does not depend on temperature, we

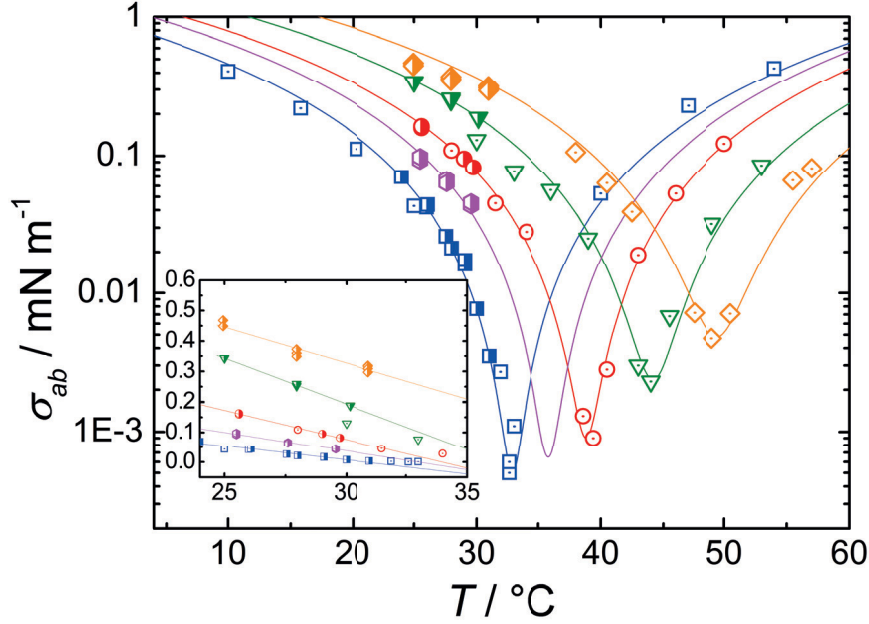


Figure 7.8: The oil/water-interfacial tension of the system $\text{H}_2\text{O} / n\text{-alkane} / \text{C}_{12}\text{E}_5$ as function of temperature. The inset shows σ_{ab} on a linear scale in the investigated temperature range. The open symbols refer to Sottmann et al. [133] and the semi-double symbols have been measured in this work. The shape of the symbols characterizes the system and is identical with the previous figures.

can determine $l = (k_{\text{B}}T / (4\pi R_{\text{SANS}})) \cdot S_{\text{T}} / (\partial(\sigma_{ab}) / \partial T)$ from eq 7.12 using the Soret coefficient S_{T} and the radius R_{SANS} measured at the *efb*. This leads to the l -values listed in Table 7.3. Note that l is in the same order of magnitude as the thickness of diffuse interfaces in microemulsion systems for the microemulsions containing n -octane [48, 139]. Additionally, we observe that l decreases with increasing length of the n -alkane chain length while the

Table 7.3: Interfacial tension derivatives with respect to temperature for microemulsions containing n -alkanes, the thickness of the transition layer l (neglecting its temperature dependence) derived from eq 7.12 and $R_{\text{SANS}} = R_0 + t$ at the *efb*.

n -alkane	$ \partial\sigma_{ab}/\partial T $ / 10^{-3} N/K m	l / nm	R_{SANS} / nm
n -C8	0.0093	0.56	15.9
n -C8/ n -C10 (1:1)	0.0125	0.31	11.7
n -C10	0.0214	0.29	8.8
n -C12	0.0313	0.15	6.7
n -C14	0.0421	0.10	5.3

Table 7.4: Thickness of the transition layer l and $(\partial l/\partial T)$ according to eq 7.13, which includes the temperature dependence of l .

n -alkane	$l^{n\text{-alkane}}$ / nm	$(\partial l/\partial T)^{n\text{-alkane}}$ / 10^{-13}m K^{-1}
n -C8	0.14 ± 0.06	1.87 ± 0.20
n -C8/ n -C10 (1:1)	0.19 ± 0.05	1.20 ± 0.13
n -C10	0.16 ± 0.04	0.52 ± 0.06
n -C12	0.17 ± 0.03	0.35 ± 0.04
n -C14	0.11 ± 0.02	0.18 ± 0.02

thickness of the diffusive interface t determined in the SANS experiments (c.f. Table 7.2) stays constant.

If we use the data summarized in Table 7.3 and look at the results of the microemulsions with different n -alkanes and analyze the dependence of $S_{\text{T}}^{n\text{-alkane}}$ versus the product of $R_{\text{SANS}}^{n\text{-alkane}}$ and $|(\partial\sigma_{\text{ab}}/\partial T)|$ we can in principle determine an averaged thickness of the transition layer l using eq 7.12, which describes all microemulsions. Although we find a linear dependence between $S_{\text{T}}^{n\text{-alkane}}$ and the product the line does not go through the origin as expected from eq 7.12. The inconsistent picture is probably a shortcoming of our original assumption that l is temperature independent.

Therefore, we included the temperature dependence of l , which leads to

$$\frac{k_{\text{B}}T}{4\pi R_{\text{SANS}}(T)} S_{\text{T}}(T) = \underbrace{l \left(\frac{\partial\sigma_{\text{ab}}}{\partial T} \right)}_{\text{intercept}} + \left(\frac{\partial l}{\partial T} \right) \times \sigma_{\text{ab}}(T) \quad (7.13)$$

In Figure 7.9 we plot the left side of eq 7.13 versus the temperature dependent interfacial tension $\sigma^{n\text{-alkane}}(T)$ for the different microemulsions. Note that we use the values of S_{T} and R_{H} measured along the $path_{\text{T}}$. We find a linear dependence for all systems. From the slope we can determine $(\partial l/\partial T)^{n\text{-alkane}}$ and $l^{n\text{-alkane}}$ can be obtained from the intercept after dividing by $(\partial\sigma_{\text{ab}}/\partial T)^{n\text{-alkane}}$. Following this procedure we determine l to be in the Angström range. Note that the uncertainty of l is quite high in the range of 20-50%. The variation of l with temperature is in the "per thousand" range and shrinks with the droplet size, which is quite reasonable (c.f. Table 7.4).

We can conclude that for the system under investigation an increase of l from 0.1 nm to

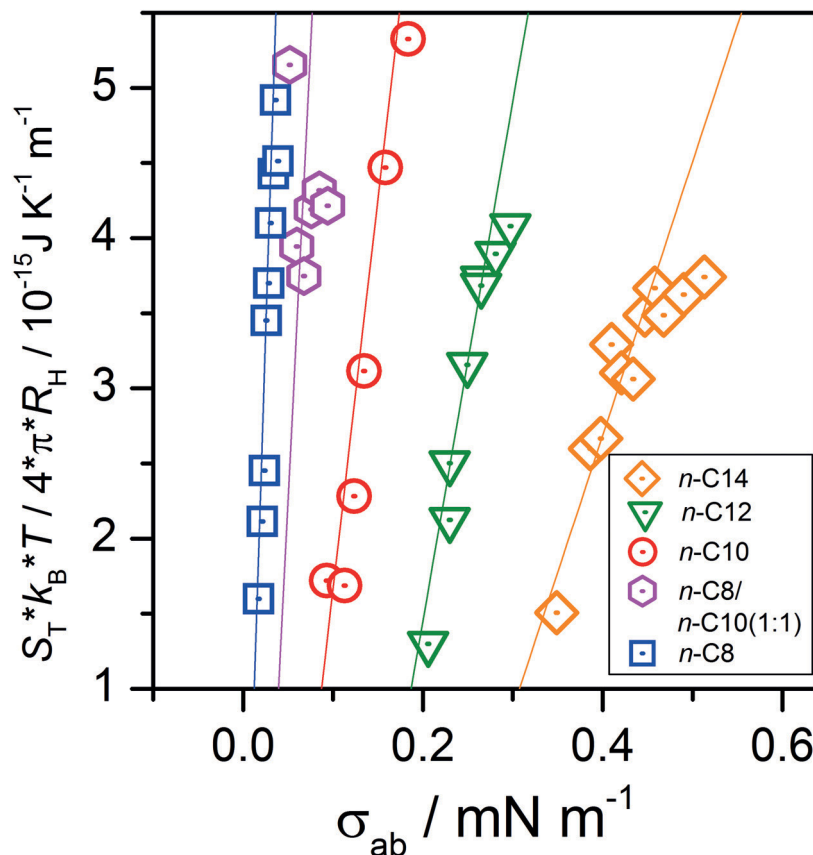


Figure 7.9: Plot of the left side of eq 7.13 versus the interfacial tension $\sigma_{ab}^{n\text{-alkane}}$ of the microemulsions with the different *n*-alkanes.

0.6 nm with decreasing chain length of the oil is found applying the model neglecting the temperature dependence of l (c.f. Table 7.3). On the other hand including the temperature dependence of l leads to a constant value between 0.1 and 0.2 nm. Although the physical origin of the l -parameter is not very well defined, we find in the present analysis rather small values for l , which correspond to typical Van der Waals radii and are too small to be identified with a surfactant film. Further research and other experimental methods are required to elucidate both the physical meaning as well as the value of l with greater accuracy.

7.4 Discussion and Conclusion

The goal of this work was the systematic investigation of the size dependence of S_T under isothermal conditions. We avoided electrostatic contributions to the thermodiffusion behavior by using the nonionic surfactant $C_{12}E_5$ and performed measurements close to the *efb* to

ensure spherical microemulsion droplets. In order to enable isothermal conditions, we varied the n -alkane from n -octane to n -tetradecane.

Due to the fact that the efb of the respective systems shifts to higher n -alkane concentrations with decreasing n -alkane chain length, the particle size can be increased while the temperature can be kept constant.

This allows a systematic variation of the radius keeping the chemistry of the microemulsion droplet interface the same. Neutron scattering experiments showed clearly that the radius of the droplets increases with decreasing n -alkane chain length and that the droplets have a spherical shape close to the efb . The Soret coefficient of the microemulsions with the different n -alkanes as function of the radius can be described by a straight line, but with slightly larger deviations the data are also compatible with a quadratic dependence on the radius.

Furthermore, we studied the relation between the interfacial tension and the Soret coefficient (c.f. eq 7.12). Assuming, that the thickness of the transition layer l is temperature independent, l decreases from 5.6 to 1.0 Å by increasing the chain length of the n -alkane from 8 to 14. Considering that l is temperature dependent (c.f. eq 7.13 and Figure 7.9) l lies between 1-2 Å and $(\partial l/\partial T)^{n\text{-alkane}}$ is in the order of a per mill relative to l decreasing with increasing chain length of the n -alkane. The decrease is reasonable, because also the size of the droplets shrinks. Summarizing we conclude that eq 7.12 is compatible with the thermodiffusion data of nonionic microemulsions and l is smaller than the diffuse amphiphilic film determined by SANS.

7.5 Acknowledgments

The authors thank Reinhard Strey for his inspiring idea and Jan Dhont for his constant interest in this work and his support. Financial support due to the Deutsche Forschungsgemeinschaft grants So 913 and Wi 1684 is gratefully acknowledged.

CONCLUSION

This work is splitted in two parts, first the development of a new technique for the measurement of thermodiffusion properties and second the systematic investigation of the thermodiffusion behavior in complex systems, microemulsions in particular.

We developed a new type of thermogravitational column, a so called thermogravitational μ -column due to its very small dimensions and a gap width of around 500 μm . This designed column has transparent sapphire windows so that the concentration difference between top and bottom can be determined interferometrically. The refractive index change with concentration causes a phase shift between two laser beams passing the column at different heights. This phase shift is determined by an active phase control measurement. Thereby the influence of vibration and random intensity fluctuations could be reduced in comparison with a pure intensity measurement. We showed the reliability of this new design by measuring three binary benchmark systems of equal mass fraction mixtures containing 1,2,3,4-tetrahydronaphtalene, isobutylbenzene and dodecane. Additionally we investigated the system toluene and *n*-hexane. The results agreed well (deviations around 5%) with the proposed literature values. The device is compact and robust and has a high precision. Due to the small sample volume of 50 μl , the investigation of rare, expensive materials is feasible. One very important benefit of this new design in comparison to the conventional thermogravitational column is the possibility to analyze the concentration change as a function of time. The optical detection allows a continuous, contact free measurement of the concentration difference at two points of variable height so that the separation process

can be analyzed in more detail.

In the second part we used microemulsions as model systems to investigate the thermodiffusive response. While for hard colloid model systems a size variation requires a new synthesis, the size, shape and interfacial tension of microemulsion droplets can be varied systematically depending on temperature and concentration. The first investigated system consisted of water, *n*-decane and the nonionic surfactant pentaethylene glycol monododecyl ether. The size and shape has been characterized by DLS and SANS measurements. Close to the emulsification failure boundary (*efb*) in the one-phase region we obtain spherical droplets with very low polydispersity. The size of these droplets could be tuned by variation of the amount of oil used in the sample preparation. We used this effect to compare the Soret coefficient with the radius and found a linear trend. However, due to the small accessible range, we were not able to unambiguously exclude a parabolic behavior. For all investigated concentrations, the Soret and thermodiffusion coefficient show a similar behavior in the one-phase region as function of temperature. Close to the *efb*, both coefficients reach a plateau value, whereas the two coefficients decrease for higher temperatures corresponding to elongated structures. Approaching the near critical boundary, the Soret coefficient diverges while the thermodiffusion coefficient increases only slightly when the network structures are formed. Thermodiffusion measurements of different droplet concentrations of the same size showed only a very small change which lead to the assumption that below a volume fraction of around 10%, the concentration effect can be neglected. The interfacial tension of the microemulsion droplets could be measured. Therefore we could analyze the Soret coefficient within the framework of an interfacial model, which accounts for the force generated by the interfacial difference between the warm and the cold side. We determined the characteristic length l , which is the width of the fluid layer where the pressure tensor is asymmetric, to be 0.3 nm for microemulsion droplets containing *n*-decane of a size around 8 nm. In order to perform the analysis we had to assume that l is temperature independent. The study of the *n*-decane microemulsion was limited by the small accessible parameter space in size and interfacial tension. Furthermore the *efb* temperature changed with the amount of oil solved in the microemulsion droplets, leading to non isothermal measurement conditions.

In the third approach, we varied the oil solved in the microemulsion droplets with *n*-alkanes of different length. This allowed us to produce microemulsions with droplets of different sizes at similar emulsification failure temperatures and this made it possible to study the size dependence of the Soret coefficient isothermally, in contrast to the measurements of the

microemulsions only containing *n*-decane. The sample compositions for each *n*-alkane have been chosen in such a way to achieve the same *efb* temperature with altering the droplets radius from around 5 nm to 15 nm. As in the case of the *n*-decane system, the size and shape of the microemulsion systems were again carefully characterized by DLS and SANS measurements, confirming spherical droplets at the *efb*. We conducted measurements of the mass diffusion, thermal diffusion and the Soret coefficient in the one-phase temperature region and found the same characteristic behavior as already mentioned for the *n*-decane system. We found a linear size dependence for the Soret coefficients which have been extrapolated to the *efb*, theoretical models for soft particles predicting a quadratic or even higher order size dependence are not applicable. Additionally, we investigated the interfacial tension of the microemulsions with different *n*-alkanes. The measurements show an almost linear temperature dependence in the investigated range. We used the radii of the different droplets, their interfacial tension derivatives with temperature and the Soret coefficients to determine the length *l*. The determined *l* lies between 1-2 Å and therefore one order of magnitude smaller than the thickness of the diffusive layer obtained from the SANS experiments. Generally, we determined *l* in the sub nanometer range.

With this work we developed a thermogravitational column with contact-free detection which measures continuously the concentration change as a function of time. Additionally we investigated the thermodiffusion behavior of nonionic microemulsions in a temperature gradient and analyzed the data within a model relating the Soret coefficient with the temperature dependence of the interfacial tension. With the measurement it was for the first time possible to determine the thickness of the interfacial layer *l*.

8.1 Outlook

The new thermogravitational column is able to detect very small relative concentration changes (down to $5 \cdot 10^{-4}$). Thereby it is possible to investigate low molecular/weight fractions in order to study diluted biological systems and expand the measurement range of other sample systems into the very diluted regime. Especially studies of biological systems are suited for this new type of measurement method in view of the origin of life theories regarding thin capillaries in temperature gradients to be the factory of life building molecules. In order to be able to investigate ternary mixtures, the interferometric setup can be expanded with a second laser at a different wavelength to determine the concentration profiles using

the dispersion relation. Thereby the advantage of thermogravitational columns in the field of ternary systems can be carried on in this new contactless method.

The role of the interfacial tension for thermodiffusion is still an open field. The use of microemulsions as model system gave access to measure the interfacial tension and to study the thermodiffusion behavior. Other microemulsion systems can be used to systematically study the influence of the interfacial tension to diffusion properties. To systematically investigate the thermal diffusion behavior compared to the interfacial tension, measurements with different isomers of the same alkane species can be performed. Thereby it is possible to achieve similar mass and size of the microemulsion droplets at similar temperatures and we expect different interfacial tensions for the isomers.

In this work we changed the amount of oil dissolved in the microemulsion droplets to change the size and the phase transition temperatures. Another way to tune the phase behavior, the interaction strength and the droplet size at constant temperature is to apply high pressures. The first step should be to build a sealed high pressure cell to conduct DLS measurements of known microemulsion to investigate the phase and diffusion behavior under pressure. The next step should be to use shorter n -alkanes than n -octane which would evaporate too fast under atmospheric conditions and to compare the behavior with the known n -alkanes. The radial change of the microemulsion droplets with the n -alkanes chain length implies even larger droplets for these shorter n -alkanes. Thereby the radial investigation of the Soret coefficient can be expanded if a proper high pressure cell is constructed which fits into the TDFRS setup. This would result in an even more sophisticated answer to the question of the size effect on thermal diffusion. Finally, high pressure experiments of microemulsions containing alkanes could enhance the understanding of processes in crude oil fields which usually are exerted to very high pressures.

Danksagung

Mein aufrichtiger Dank gilt Frau Dr. Simone Wiegand für die interessante Themenstellung, für die vielen Ideen die diese Arbeit beflügelt haben und ihre durchgehende Unterstützung. Ich bedanke mich herzlich bei Herrn Prof. Jan Dhont für das durchgehend hervorragende Umfeld im von ihm geführten Institut am Forschungszentrum Jülich. Ganz besonders möchte ich mich bei Frau Marie Göcking für die große Hilfe in vielen Belangen bedanken, ebenso bei Herrn Dr. Hartmut Kriegs, Herrn Dieter Tiefenbach und Herrn Hans Jürgen Hoffmann bedanke ich mich für die durchgehende Unterstützung. Ich danke Herrn Prof. Stefan Egelhaaf für seine Tätigkeit als Zweitgutachter meiner Arbeit.

Die Kooperation mit Prof. M.M. Bou-Ali Alain Martin hat meine Arbeit sehr bereichert und auch auf persönlicher Ebene für sehr positive Erlebnisse gesorgt. Auch möchte ich mich für die hervorragende Zusammenarbeit mit Herrn Dr. Thomas Sottmann und Nils Becker bedanken, ohne deren Hilfe ich das Feld der Mikroemulsionen kaum hätte betreten können.

Die Arbeitsgruppe am ICS-3 hat mich sehr offen empfangen. Insbesondere möchte ich mich bei Herrn Dr. Gerd Meier für viele sehr interessante Diskussionen bedanken und für die große Hilfe im Bezug auf Hochdruckanlagen. Herr Donald Guu war mir ein besonders geschätzter Kollege und Freund der mir immer aufs Neue mit Ansporn, Ideen und einem offenen Ohr zur Seite stand. Auch meiner Kollegin Zilin Wang danke ich für die gute Zusammenarbeit und Hilfe bei Problemen.

Zum Abschluss möchte ich meiner Familie und meinen Freunden meinen Dank aussprechen, die mir immer als fester Rückhalt zur Seite gestanden haben.

LIST OF FIGURES

2.1	A cut through the phase prism along a fixed surfactant concentration γ_a . The two lines represent the phase transition temperatures along the axis of oil content w_B . With increasing temperature, the aggregates change from spherical droplets at the <i>efb</i> to elongated structures for intermediate temperatures and end up in network like structures at the <i>ncb</i> before phase separation occurs. The numbers indicate the phase regions with the upper and lower two phase regions marked with over and underlined numbers.	13
3.1	Different basic principles of thermodiffusion measurements. Type a) is the basis of a beam deflection or also called Soret-cell. It is heated from above to avoid convection. The concentration gradient (grey arrow marked with <i>c</i>) due to thermodiffusion occurs parallel to the temperature gradients (colored arrow marked <i>T</i>) axis. Type b) shows the principle of a thermal lens. This temperature profile is created by irradiating a thin transparent cell with a gaussian laser beam being absorbed by the sample. Due to the gaussian intensity profile of the beam, the center is heated stronger than the outer regions, leading to a radial temperature gradient which is followed by a radial concentration gradient. This concentration gradient can be probed by investigating the strength of refraction similar to a thin or thick glass lens. Type c) shows the principle where thermodiffusion is coupled with convection. The horizontal temperature gradient causes a mixture to separate horizontally. The buoyancy due to thermal expansion at the warm/cold side causes the individual species to ascend/descend, respectively. This principle relies on the lighter species going to the warm side. For the opposite case, instabilities are generated leading to complex separation profiles. This type is used in thermogravitational columns	16
3.2	This picture shows a sketch of the (IR)TDFRS setup used in this work. The dotted line represents a thermally insulating box to reduce thermal fluctuations of the optical parts.	20

3.3	The normalized heterodyne intensity signal in the IR-TDFRS setup versus time. The sample is C_7G_1/H_2O with $w = 0.069$ wt at $20^\circ C$ (circles) and $60^\circ C$ (squares). The horizontal dotted line is a guide to the eyes and marks the normalized thermal plateau. The excitation function (solid line) reaches the plateau after 8 ms (vertical dotted line). (Picture taken from B. Arlt.)	23
3.4	Working principle of the Abbe refractometer. The sample volume is applied onto the prism, leading to a change in the angle of total internal reflection. The light source and the lenses are adjusted to find the maximum intensity measured at the detector which also records the position of the detected light. This change of position is used to calculate the refractive index of the sample on top of the prism.	25
3.5	Schematic setup of the interferometer used to determine the refractive index increment by temperature. A laser beam is passing a beam splitter, where the reflected light is blocked by a wall. The passing light hits the sample cell, where part of the light is reflected at the front window and part is penetrating the sample volume and being reflected by the rear window. The light passing through the window is again blocked by a wall. The two reflections hit the beam splitter and are guided onto a pinhole. Due to interference of the two reflected beams, a fringe pattern can be observed. By adjusting the pinholes size to one fringe spacing, the detector achieves a large contrast. The temperature of the sample is ramped linearly, leading to a change in refractive index of the sample which causes a phase shift of the beam penetrating the sample. This phase shift can be recorded by analyzing the time dependent interference pattern.	26
5.1	A sketch of the composed micro-column with a cut in the upper part.	33
5.2	Schematic sketch of the interferometer probing the concentration difference at two different heights of the TG micro-column with a horizontal temperature gradient. The concentration difference results in a phase shift $\Delta\phi$ of the intensity signal determined by a 2π scan of the prism mounted on the piezo stack.	35
5.3	Sketch of the active phase control mechanism. Two intensity scans recorded at two different times t_0 and t_1 (squares and circles) and the fitted sinusoidal curves. The phase shift $\Delta\phi$ is caused by concentration changes.	37
5.4	Optical tweezers setup to determine the position of the sapphire surfaces. The cell can be moved in x- and z-direction on a micrometer stage. (b) Position of the different surfaces along the cell. (c) The calculated gap width and the width of the (d) sapphire windows as function of the cell height.	38
5.5	A sketch of the cell volume including the considered dead volumes, which are used for filling the micro-column.	40
5.6	Numerical simulation results of the toluene mass fraction profile in the binary mixture TOL/HEX. The left figure shows the profile over the entire height of the micro-column. The right figure is a plot of the concentration profile at a height of 15 mm at the stationary state.	41

- 5.7 Numerical simulation results for the binary mixture TOL/HEX at the stationary state (a) Temperature profile within the micro-column gap. The upper part shows the deviations from a linear fit. (b) Velocity profile within de micro-column gap at a height of 15mm. (c) The vertical concentration distribution profile of the TOL mass fraction in the middle of the gap along the micro-column. The upper part shows again the deviations from a linear fit. 48
- 5.8 (a) Typical experimental results for phase shift between top and bottom for the mixture TOL/HEX and (b) THN/DD with a mass weight fraction of 50% as function of time. The time base has been chosen in such a way that at time zero the temperature gradient has been enabled. The inset shows the phase close to the turn-on time. The origin of the fast jump in the signal will be discussed in detail in the appendix. 49
- 5.9 The thermal diffusion coefficient, D_T , for the four studied systems in comparison with literature values. The largest absolute deviations are found for the system TOL/HEX, while the largest relative deviation of around 6% is found for the system THN-IBB. 50
- 5.10 Top graph: temperature at the outside of the sapphire windows at the two sides (warm side - filled diamonds; cold side - open circles) of the TG micro-column filled with toluene as function of time measured by means of an infrared camera. The upper graph shows that due to different time constants for the warm and the cold side there is a small overshoot in the mean temperature (small dots) as function of time. Bottom graph: development of the temperature at the bottom and at the top of the cell measured at the covered metal surface. The temperature equilibrates at the bottom of the cell much faster than at the top, so that for a short time a vertical temperature gradient in the order of 0.2-0.3 K is established. The solid lines are exponential fits with time constants given in the graph. 51
- 5.11 (a) Phase drift as function of time. After equilibration within the first hour, the phase drifts with a rate $0.0064 \pi/h$. This corresponds to a drift of less than 0.02π for a measurement time of 3 hours, which results for IBB/THN, the system with the weakest measurement signal, in a relative error of 1%. (b) Phase response in pure THN, when the temperature gradient is switched on and off, respectively. 52

-
- 6.1 Schematic phase behavior of water-rich non-ionic microemulsion systems together with the occurring microstructures. The left figure shows a isothermal cut through the phase prism (red plane). Increasing the amount of oil and surfactant at a constant oil-to-surfactant ratio leads to an increasing number of droplets. The red line indicates the binodal. The right figure shows a vertical cut through the phase prism at constant γ_a (blue plane). The one phase region is limited by the so-called emulsification failure boundary (*efb*) and the near critical boundary (*ncb*). Spherical droplets are formed along the *efb*, which increase in size with increasing oil content. Moving away from the *efb* leads to an elongation of the aggregates. At temperatures close to the *ncb* network-like structures are often found. 55
- 6.2 Phase diagrams of water/*n*-decane/ $C_{12}E_5$ at different γ_A as function of the oil content w_B . The chosen experimental paths are illustrated by the blue arrows *path_T*, *path_{w_B}* and *path_φ*. The inset shows the *path_T*. The *path_{w_B}* denotes the path along the *efb* and the stars connected by the dashed line mark the isothermal measurement of *path_φ*. 60
- 6.3 The hydrodynamic radius, determined by DLS-measurements, plotted against the temperature for the microemulsion H_2O/n -decane/ $C_{12}E_5$ with $\gamma_a = 0.03$ and $w_B = 0.029$. The radius decreases with decreasing temperature until it reaches an almost constant value at the *efb* temperature at around $27^\circ C$. . . 61
- 6.4 The distribution function $A(\Gamma)$ of the inverse relaxation time, weighted by Γ as function of Γ of the system H_2O/n -decane/ $C_{12}E_5$ with $\gamma_a = 0.03$ and $w_B = 0.029$ at different angles. 63
- 6.5 SANS curve of the microemulsion H_2O/n -decane/ $C_{12}E_5$ with the same molecular composition as the DLS sample (c.f. Figure 6.3) to determine the size and shape of the microemulsion aggregates at the *efb* at $T = 26.09^\circ C$ (marked by the star in the phase diagram shown in the inset). Note, that the phase boundary is shifted to lower temperatures by $\Delta T \approx -1.5$ K due to the replacement of H_2O by D_2O and $C_{10}H_{18}$ by $C_{10}D_{18}$. The scattered intensity is plotted versus the scattering vector q on a double-log scale. The almost constant intensity at small values of q indicate the existence of nearly spherical particles. The line represents a fit of a model for polydisperse shells. See text for details. 64
- 6.6 The diffusion D , thermal diffusion D_T and Soret coefficient S_T in the one-phase region at different temperatures ($\gamma_a = 0.0421$ and $w_B = 0.03$). The chosen experimental path is illustrated in the inset. The dashed lines are guides to the eye. 66

- 6.7 Measured diffusion, D , thermal diffusion, D_T and Soret coefficient, S_T at different mass fractions of oil w_B at a fixed $\gamma_a = 0.0421$ measured along the $path_{w_B}$. The upper inset shows the apparent radius, R_{TDFRS} , as function of the oil fraction. The lower inset displays S_T as function of the apparent radius, R_{TDFRS} , calculated from D using the Stokes-Einstein-relation. Linear and quadratic fits were performed by weighting the data points with their uncertainties. The corresponding efb temperatures rise from 23 °C to 28.5 °C with increasing w_B 67
- 6.8 Diffusion, D , thermal diffusion, D_T , and Soret coefficients, S_T , measured at $T_{efb} \approx 27$ °C for different volume fraction, ϕ , of the microemulsion droplets keeping the oil/surfactant ratio constant at 1/1. S_T decreases slightly with ϕ , which is related to the slightly different slopes of $D(T)$ and $D_T(T)$. The inset shows the apparent radius R_{TDFRS} as function of the volume fraction of the droplets. The dashed lines are linear fits, weighted with the uncertainties of the data points. 69
- 6.9 Soret coefficient as function of the apparent radius, R_{TDFRS} , measured along the $path_T$, $path_{w_B}$ and $path_\phi$. The $path_T$ -line is a guides to the eye, while the $path_{w_B}$ -data are fitted by a straight line (dashed) and a quadratic function (dotted) through the origin. Note, that R_{TDFRS} is calculated using the Stokes-Einstein-relation which assumes spherical aggregates, while it is known from DLS and SANS that the shape of the structure changes along $path_T$ as illustrated by the grey pictograms. 71
- 6.10 The oil/water-interfacial tension of the system water / n -decane / $C_{12}E_5$ as a logarithmic function of temperature. The inset shows the interfacial tension over the temperature range used in the thermal diffusion measurements. In this regions it shows an almost linear dependence. 73
- 6.11 The inset in the upper part shows S_T as function of the product of the apparent radius, R_{TDFRS} and the temperature derivative of interfacial tension, which allows determination of the characteristic length from the slope of the plot. S_T , and R_{TDFRS} have been measured along the $path_{w_B}$. The solid line represents the calculated Soret coefficient, S_T , according to Eq. 7.12 with temperature. The lower part shows the corresponding S_T -values calculated along $path_T$ 74
- 7.1 Schematic phase behavior of a water-rich microemulsion stabilized by a non-ionic surfactant [58]. The phase boundaries are shown as a function of temperature and mass fraction w_B of the oil at a constant mass fraction γ_a of the surfactant in the mixture of water and surfactant. Between the lower emulsification failure boundary (efb) and the near critical boundary (ncb) a thermodynamically stable microemulsion is formed. Increasing the temperature results in a structural transformation from spherical droplets at the efb over elongated droplets to finally network like structures at the ncb before demixing occurs [10, 47, 82, 143] . Increasing the mass fraction of oil and temperature staying at the efb will yield larger microemulsion droplets. 80

7.2	Phase behavior of water-rich microemulsion systems of the type $\text{H}_2\text{O}/n$ -alkane/ C_{12}E_5 at a constant mass fraction of C_{12}E_5 in the $\text{H}_2\text{O}/\text{C}_{12}\text{E}_5$ -mixture $\gamma_a = 0.03$. The microstructure and the thermal diffusion behavior has been studied near the <i>efb</i> at $T_{efb} = 27.0 \pm 0.5$ °C (stars, connected by the dashed dotted line). Increasing the chain length of the n -alkane the one phase region shifts to higher temperatures. Concomitantly, the maximum amount of oil which can be solubilized at $T = 27.0 \pm 0.5$ °C decreases strongly.	85
7.3	SANS measurement performed in film contrast to determine the size and shape of the microemulsion aggregates at the corresponding <i>efb</i> temperature. The scattered intensity is plotted versus the scattering vector q . The data are described by an appropriate combination of form- and structure factor. The inset in part (a) shows the radial scattering length density profile of the system n -octane. See text for details.	87
7.4	Hydrodynamic radius, R_H , as function of temperature for microemulsion with various n -alkanes and n -alkane mixtures determined by DLS. The composition of the samples is given in Table 7.1.	90
7.5	The diffusion D , thermodiffusion D_T and Soret coefficient S_T as function of temperature. The five microemulsion systems (compositions are given in Table 7.1) are studied in the one-phase region. We used the same symbols as in Figure 7.2,7.3 and 7.4 and the dashed lines are guides to the eye.	92
7.6	The diffusion D , thermodiffusion D_T and Soret coefficient S_T for the five microemulsions under study extrapolated to the <i>efb</i> -temperature of 27.0°C as function of $R_{\text{SANS}} = R_0 + t$ with the core radius R_0 and the thickness of the diffuse amphiphilic film t . We used the same symbols as before. For D the black line is a $1/R_0$ fit, for D_T it is a constant and for S_T the black line is a linear fit and the red dash dot line is a parabolic fit.	94
7.7	A qualitative illustration of eq 7.12. Exemplarily we show schematically two microemulsion droplets solubilizing n -tetradecane and n -dodecane, respectively. The blue circles represent the hydrophilic headgroups. Due to the larger droplet size for the shorter oil the temperature difference between both sides of the droplet marked by "x" is also larger. Further details see in the text.	95
7.8	The oil/water-interfacial tension of the system $\text{H}_2\text{O} / n$ -alkane / C_{12}E_5 as function of temperature. The inset shows σ_{ab} on a linear scale in the investigated temperature range. The open symbols refer to Sottmann et al. [133] and the semi-double symbols have been measured in this work. The shape of the symbols characterizes the system and is identical with the previous figures.	97
7.9	Plot of the left side of eq 7.13 versus the interfacial tension $\sigma_{ab}^{n\text{-alkane}}$ of the microemulsions with the different n -alkanes.	99

LIST OF TABLES

3.1	Overview of different measurement setups used in thermal diffusion studies .	19
5.1	Experimental density, ρ_0 , dynamic viscosity, μ , mass expansion coefficient, β , and the thermal diffusion coefficient, D_T , for the mixture TOL/HEX with a mass fraction of 0.5167 at T=298 K used in the numerical simulation.	41
5.2	Comparison between experimental and numerical simulation results of the stationary separation under the thermogravitational effect for the new design of the micro-column for the mixture TOL/HEX with a mass fraction of 0.5167. D_T is the average of the individual literature values listed in 5.1.	42
5.3	Experimental and numerical results for the investigated binary mixtures at T=298 K and a mass fraction of c=0.5. In all simulations the dead volume caused by the inlet and the outlet have been considered.	43
5.4	Thermal diffusion coefficients determined for four binary mixtures with 50 wt%. All measurements have been performed at 298 K. The error is variance of the mean from five individual measurements.	44
7.1	Composition of the studied microemulsions. Given are the volume fractions of the surfactant Φ_C , the surfactant in the internal interface $\Phi_{C,i}$ and the oil Φ_B	82
7.2	Fit parameters of the form and structure factor applied to describe the SANS curves of the water-rich microemulsions D ₂ O/ <i>n</i> -alkane/C ₁₂ E ₅ with the composition given in Table 7.1 at $T_{efb} = 26.1 \pm 0.4^\circ\text{C}$ (Note that the temperature in SANS experiments was slightly lower due to the deuterated solvents). The mean droplet radius R_0 , standard deviation of the polydispersity distribution σ , thickness of the diffuse amphiphilic film t , rel. thickness of the attractive potential well $\varepsilon = \Delta/a = t/(2R_0 + t)$, effective droplet volume fraction $\eta = \Phi_{disp} a^3/\delta^3 = \Phi_{disp} ((2R_0)/2(R_0 + t))^3$ and potential depth u_0	90
7.3	Interfacial tension derivatives with respect to temperature for microemulsions containing <i>n</i> -alkanes, the thickness of the transition layer l (neglecting its temperature dependence) derived from eq 7.12 and $R_{SANS} = R_0 + t$ at the <i>efb</i>	97
7.4	Thickness of the transition layer l and $(\partial l/\partial T)$ according to eq 7.13, which includes the temperature dependence of l	98

BIBLIOGRAPHY

- [1] Ansys Inc, (2010), Ansys-Fluent 13.0, Lebanon, USA.
- [2] Ansys Inc, (2010), Gambit 2.4.6, Lebanon, USA.
- [3] J.L. Anderson. Colloid transport by interfacial forces. *Annu. Rev. Fluid Mech.*, 21:61–99, 1989.
- [4] J. Andrews and A. Akbarzadeh. Enhancing the thermal efficiency of solar ponds by extracting heat from the gradient layer. *Solar Energy*, 78(6):704–716. 945BA.
- [5] B. Arlt, S. Datta, T. Sottmann, and S. Wiegand. Soret effect of n-octyl β -d-glucopyranoside water around the critical micelle concentration. *J. Phys. Chem. B*, 114(6):2118–2123, 2010.
- [6] P. Baaske, F. M. Weinert, S. Duhr, K. H. Lemke, M. J. Russell, and D. Braun. Extreme accumulation of nucleotides in simulated hydrothermal pore systems. *P. Natl. Acad. Sci. USA*, 104(22):9346–9351.
- [7] P. Baaske, C. J. Wienken, P. Reineck, S. Duhr, and D. Braun. Optical thermophoresis for quantifying the buffer dependence of aptamer binding. *Angewandte Chemie-International Edition*, 49(12):2238–2241.
- [8] U. Bagger-Jorgensen, Olsson and K. Mortensen. Microstructure in a ternary microemulsion studied by small angle neutron scattering. *Langmuir*, 13(6):1413–1421, 1997.
- [9] R. J. Baxter. Percus-yevick equation for hard spheres with surface adhesion. *J. Chem. Phys.*, 49(6):2770–2774, 1968.
- [10] A. Bernheim-Groswasser, T. Tlusty, S. A. Safran, and Y. Talmon. Direct observation of phase separation in microemulsion networks. *Langmuir*, 15(17):5448–5453, 1999.
- [11] P. Blanco, M. M. Bou-Ali, J. K. Platten, D. A. de Mezquia, J. A. Madariaga, and C. Santamaria. Thermodiffusion coefficients of binary and ternary hydrocarbon mixtures. *J. Chem. Phys.*, 132(11):114506 1–6, 2010.
- [12] P. Blanco, M. M. Bou-Ali, J. K. Platten, P. Urteaga, J. A. Madariaga, and C. Santa-

- maria. Determination of thermal diffusion coefficient in equimolar *n*-alkane mixtures: Empirical correlations. *J. Chem. Phys.*, 129(17):174504–1 – 174504–6, 2008.
- [13] P. Blanco, H. Kriegs, M. P. Lettinga, P. Holmqvist, and S. Wiegand. Thermal diffusion of a stiff rod-like mutant y21m-fd-virus. *Biomacromolecules*, 12:1602–1609, 2011.
- [14] M. M. Bou-Ali, O. Ecenarro, J. A. Madariaga, C. M. Santamaria, and J. J. Valencia. Thermogravitational measurement of the soret coefficient of liquid mixtures. *J. Phys.: Condens. Matter*, 10(15):3321–3331, 1998.
- [15] M. M. Bou-Ali, J. J. Valencia, J. A. Madariaga, C. Santamaria, O. Ecenarro, and J. F. Dutrieux. Determination of the thermodiffusion coefficient in three binary organic liquid mixtures by the thermogravitational method (contribution of the universidad del pais vasco, bilbao, to the benchmark test). *Philos. Mag.*, 83(17-18):2011–2015, 2003.
- [16] M.M. Bou-Ali and J. K. Platten. Metrology of the thermodiffusion coefficients in a ternary system. *J Non-Equil Thermody*, 30(4):385–399, 2005.
- [17] M. Braibanti, D. Vigolo, and R. Piazza. Does thermophoretic mobility depend on particle size? *Phys. Rev. Lett.*, 100(10):108303–1–108303–4, 2008.
- [18] D. Braun and A. Libchaber. Trapping of dns by thermophoretic depletion and convection. *Phys. Rev. Lett.*, 89(18):188103–1–188103–4, 2002.
- [19] P. G. Brewer, T. R. S. Wilson, J. W. Murray, R. G. Munns, and C. D. Densmore. Hydrographic observations on red-sea brines indicate a marked increase in temperature. *Nature*, 231(5297):37–8. J1983.
- [20] I. Budin, R. J. Bruckner, and J. W. Szostak. Formation of protocell-like vesicles in a thermal diffusion column. *J. Am. Chem. Soc.*, 131(28):9628–9629, 2009.
- [21] S. Burauer, T. Sachert, T. Sottmann, and R. Strey. On microemulsion phase behavior and the monomeric solubility of surfactant. *Phys. Chem. Chem. Phys.*, 1(18):4299–4306, 1999.
- [22] S. Burghartz and B. Schulz. Thermophysical properties of sapphire, aln and mgal2o4 down to 70-k. *J. Nucl. Mater.*, 212:1065–1068, 1994.
- [23] D. R. Caldwell and S. A. Eide. Separation of seawater by soret diffusion. *Deep-Sea Research Part a-Oceanographic Research Papers*, 32(8):965–982. Awd71.
- [24] J. Chan, J. J. Popov, S. Kolisnek-Kehl, and D. G. Leaist. Soret coefficients for aqueous polyethylene glycol solutions and some tests of the segmental model of polymer thermal diffusion. *J. Solution Chem.*, 32(3):197–214, 2003.
- [25] S. Chapman. The kinetic theory of simple and composite monatomic gases: viscosity, thermal conduction and diffusion. *Proc. Roy. Soc. A*, 93:1–20, 1916.
- [26] C. L. Choy, K. W. Kwok, W. P. Leung, and F. P. Lau. Thermal-conductivity of poly(ether ether ketone) and its short-fiber composites. *J. Polym. Sci., Part B: Polym. Phys.*, 32(8):1389–1397, 1994.

- [27] C. L. Choy and W. P. Leung. Thermal-expansion of poly(etheretherketone) (peek). *J. Polym. Sci., Part B: Polym. Phys.*, 28(11):1965–1977, 1990.
- [28] H. Cölfen and M. Antonietti. *Field-flow fractionation techniques for polymer and colloid analysis*, volume 150 of *Advances in Polymer Science*, pages 67–187.
- [29] K. Clusius and G. Dickel. *Naturwissenschaften*, 26:546, 1938.
- [30] K. Clusius and G. Dickel. Zur trennung der chlorisotope. *Naturwissenschaften*, 27:148–149, 1939.
- [31] P. Costeseque and J. C. Loubet. Measuring the soret coefficient of binary hydrocarbon mixtures in packed thermogravitational columns (contribution of toulouse university to the benchmark test). *Philos. Mag.*, 83(17-18):2017–2022, 2003.
- [32] B. J. de Gans, R. Kita, S. Wiegand, and J. Luettmmer-Strathmann. Unusual thermal diffusion in polymer solutions. *Phys. Rev. Lett.*, 91(24):245501, 2003.
- [33] C. Debuschewitz and W. Köhler. Molecular origin of thermal diffusion in benzene plus cyclohexane mixtures. *Phys. Rev. Lett.*, 87(5):055901, 2001.
- [34] J. K. G. Dhont. Thermodiffusion of interacting colloids. ii. a microscopic approach. *J. Chem. Phys.*, 120(3):1642–1653, 2004.
- [35] J. K. G. Dhont and W. J. Briels. Single-particle thermal diffusion of charged colloids: Double-layer theory in a temperature gradient. *Eur. Phys. J. E*, 25(1):61–76, 2008.
- [36] J. K. G. Dhont, S. Wiegand, S. Duhr, and D. Braun. Thermodiffusion of charged colloids: Single-particle diffusion. *Langmuir*, 23:1674–1683, 2007.
- [37] T. D. Du and W. L. Luo. Intensity dependent transmission dynamics in magnetic fluids. *J. Appl. Phys.*, 85(8):5953–5955, 1999.
- [38] S. Duhr and D. Braun. Thermophoretic depletion follows boltzmann distribution. *Phys. Rev. Lett.*, 96(16):168301–1 – 168301–4, 2006.
- [39] S. Duhr and D. Braun. Why molecules move along a temperature gradient. *P. Natl. Acad. Sci.*, 103(52):19678–19682, 2006.
- [40] J. F. Dutrieux, J. K. Platten, G. Chavepeyer, and M. M. Bou-Ali. On the measurement of positive soret coefficients. *J. Phys. Chem. B*, 106(23):6104–6114, 2002.
- [41] D. Enskog. Bemerkung zu einer fundamentalgleichung in der kinetischen gastheorie. *Phys. Z.*, 12:533–539, 1911.
- [42] P. D. I. Fletcher and J. F. Holzwarth. Aggregation kinetics of oil-in-water microemulsion droplets stabilized by c12e5. *J. Phys. Chem.*, 95(6):2550–2555, 1991.
- [43] T. Foster, T. Sottmann, R. Schweins, and R. Strey. Small-angle neutron scattering from giant water-in-oil microemulsion droplets. i. ternary system. *J. Chem. Phys.*, 128(5):54502, 2008.
- [44] T. Foster, T. Sottmann, R. Schweins, and R. Strey. Small-angle neutron scattering

- from giant water-in-oil microemulsion droplets. i. ternary system. *J. Chem. Phys.*, 128(5):054502–1 – 054502–13, 2008.
- [45] W. H. Furry, R. C. Jones, and L. Onsager. On the theory of isotope separation by thermal diffusion. *Physical Review*, 55(11):1083–1095, 1939.
- [46] M. Giglio and A. Vendramini. Thermal-diffusion measurements near a consolute critical-point. *Phys. Rev. Lett.*, 34(10):561–564, 1975.
- [47] O. Glatter, R. Strey, K. V. Schubert, and E. W. Kaler. Small angle scattering applied to microemulsions. *Ber. Bunsen-Ges. Phys. Chem. Chem. Phys.*, 100(3):323–335, 1996.
- [48] Michael Gradzielski, Dominique Langevin, L. Magid, and Reinhard Strey. Small-angle neutron scattering from diffuse interfaces. polydisperse shells in water-oil-c10e4 systems. *J. Phys. Chem.*, 99:13232–13238, 1995.
- [49] T. Hellweg and R. von Klitzing. Evidence for polymer-like structures in the single phase region of a dodecane/c12e5/water microemulsion: a dynamic light scattering study. *Physica A*, 283(3-4):349–358, 2000.
- [50] F. Huang, P. Chakraborty, C. C. Lundstrom, C. Holmden, J. J. G. Glessner, S. W. Kieffer, and C. E. Lesher. Isotope fractionation in silicate melts by thermal diffusion. *Nature*, 464(7287):396–U89, 2010. 570FG.
- [51] S. Iacopini and R. Piazza. Thermophoresis in protein solutions. *Europhysics Letters*, 63(2):247–253, 2003.
- [52] S. Iacopini, R. Rusconi, and R. Piazza. The "macromolecular tourist": Universal temperature dependence of thermal diffusion in aqueous colloidal suspensions. *Eur. Phys. J. E*, 19:59–67, 2006.
- [53] J. N Israelachvili. *Intermolecular \mathcal{E} and surface forces*. Academic press, Amsterdam, 1991.
- [54] J.N. Israelachvili. *Intermolecular and Surface Forces*. Academic Press, London, 3rd ed. edition, 2010.
- [55] B. Jakobs, T. Sottmann, and R. Strey. Efficiency boosting with amphiphilic block copolymers - a new approach to microemulsion formulation. *Tenside Surfactants Detergents*, 37(6):357–364, 2000.
- [56] M. Kahlweit and R. Strey. Phase-behavior of ternary-systems of the type h2o-oil-nonionic amphiphile (microemulsions). *Angew. Chem. Int. Ed.*, 24(8):654–668, 1985.
- [57] Manfred Kahlweit, Reinhard Strey, and Gerhard Busse. Microemulsions - a qualitative thermodynamic approach. *J. Phys. Chem.*, 94:3881–3894, 1990.
- [58] Manfred Kahlweit, Reinhard Strey, and Gerhard Busse. Weakly to strongly structured mixtures. *Phys. Rev. E*, 47(6):4197–4209, 1993.
- [59] W. Köhler and R. Schäfer. *Polymer analysis by thermal-diffusion forced Rayleigh scattering*, volume 151 of *Advances in Polymer Science*, pages 1–59. 2000.

- [60] P. K. Kilpatrick, C. A. Gorman, H. T. Davis, L. E. Scriven, and W. G. Miller. Patterns of phase-behavior in ternary ethoxylated alcohol normal-alkane - water mixtures. *J. Phys. Chem.*, 90(21):5292–5299, 1986.
- [61] Y. Kishikawa, S. Wiegand, and R. Kita. Temperature dependence of soret coefficient in aqueous and nonaqueous solutions of pullulan. *Biomacromolecules*, 11(3):740–747, 2010.
- [62] W. Köhler and B. Müller. Soret and mass diffusion-coefficients of toluene n-hexane mixtures. *J. Chem. Phys.*, 103(10):4367–4370, 1995.
- [63] W. Köhler and P. Rossmanith. Aspects of thermal-diffusion forced rayleigh-scattering - heterodyne-detection, active phase tracking, and experimental constraints. *J. Phys. Chem.*, 99(16):5838–5847, 1995.
- [64] P. Kolodner, H. Williams, and C. Moe. Optical measurement of the soret coefficient of ethanol water solutions. *J. Chem. Phys.*, 88(10):6512–6524, 1988.
- [65] A. Königer, B. Meier, and W. Köhler. Measurement of the soret, diffusion, and thermal diffusion coefficients of three binary organic benchmark mixtures and of ethanol-water mixtures using a beam deflection technique. *Philos. Mag.*, 89(10):907–923, 2009.
- [66] M. Kotlarchyk and S. H. Chen. Analysis of small-angle neutron-scattering spectra from polydisperse interacting colloids. *J. Chem. Phys.*, 79(5):2461–2469, 1983.
- [67] A. Leahy-Dios, M. M. Bou-Ali, J. K. Platten, and A. Firoozabadi. Measurements of molecular and thermal diffusion coefficients in ternary mixtures. *J. Chem. Phys.*, 122(23):234502 1–12, 2005.
- [68] D. G. Leaist and L. Hui. Unusual thermal-diffusion of ionic surfactants near the critical micelle concentration. *J. Phys. Chem.*, 93:7547–7549, 1989.
- [69] M. S. Leaver, U. Olsson, H. Wennerstrom, and R. Strey. Emulsification failure in a ternary microemulsion. *J. Phys. II*, 4(3):515–531, 1994.
- [70] H. Leitao, A. M. Somoza, M. M. T. daGama, T. Sottmann, and R. Strey. Scaling of the interfacial tension of microemulsions: A phenomenological description. *J. Chem. Phys.*, 105(7):2875–2883, 1996.
- [71] G. Liu and J. C. Giddings. Separation of particles in aqueous suspensions by thermal field-flow fractionation - measurement of thermal-diffusion coefficients. *Chromatographia*, 34(9-10):483–492, 1992.
- [72] C. Ludwig. Diffusion zwischen ungleich erwärmten orten gleich zusammengesetzter lösungen. *Sitz. Ber. Akad. Wiss. Wien Math.-naturw. Kl*, 20:539, 1856.
- [73] J. Luettmer-Strathmann. Thermodiffusion in the critical region. In W. Köhler and S. Wiegand, editors, *Thermal nonequilibrium phenomena in fluid mixtures*, volume 584 of *Lecture Notes Physics*, pages 24–37. Springer, Berlin, 2002.
- [74] J. Luettmer-Strathmann. Two-chamber lattice model for thermodiffusion in polymer solutions. *J. Chem. Phys.*, 119(5):2892–2902, 2003.

- [75] J. Luettmer-Strathmann. Lattice model for thermodiffusion in polymer solutions. *Int. J. Thermophys.*, 26:1693–1707, 2005.
- [76] C. Lundstrom. Hypothesis for the origin of convergent margin granitoids and earth’s continental crust by thermal migration zone refining. *Geochimica Et Cosmochimica Acta*, 73(19):5709–5729, 2009. 541LE.
- [77] D. Macgowan and D. J. Evans. Heat and matter transport in binary-liquid mixtures. *Phys. Rev. A*, 34(3):2133–2142, 1986.
- [78] J. A. Madariaga, C. Santamaria, H. Barrutia, M. M. Bou-Ali, O. Ecenarro, and J. J. Valencia. Validity limits of the fjo thermogravitational column theory: Experimental and numerical analysis. *Cr Mecanique*, 339(5):292–296, 2011.
- [79] S. D. Majumdar. The theory of the separation of isotopes by thermal diffusion. *Phys. Rev.*, 81(5):844–848, 1951.
- [80] A. Martin, M. M. Bou-Ali, E. Gandarias, P. Aristimuño, and S. Wiegand. Ep12382015, europe, 2012.
- [81] C. B. Mast and D. Braun. Thermal trap for dna replication. *Phys. Rev. Lett.*, 104(18):188102, 2010. 592YI.
- [82] U. Menge, P. Lang, G. H. Findenegg, and P. Strunz. Structural transition of oil-swollen cylindrical micelles of $C_{12}E_5$ in water studied by sans. *J. Phys. Chem. B*, 107(6):1316–1320, 2003.
- [83] S. V. G. Menon, C. Manohar, and K. S. Rao. A new interpretation of the sticky hard-sphere model. *J. Chem. Phys.*, 95(12):9186–9190, 1991.
- [84] A. Mialduna and V. Shevtsova. Measurement of the soret and diffusion coefficients for benchmark binary mixtures by means of digital interferometry. *J. Chem. Phys.*, 134(4):044524 1–12, 2011.
- [85] K. I. Morozov. Soret effect in molecular mixtures. *Phys. Rev. E*, 79(3):031204. Part 1.
- [86] P. Naumann, N. Becker, S. Datta, T. Sottmann, and S. Wiegand. Soret coefficient in nonionic microemulsions: Concentration and structure dependence. *J. Chem. Phys. B*, 117(18):5614–5622, 2013.
- [87] P. Naumann, A. Martin, H. Kriegs, M. Larrañaga, M. Bou-Ali, and S. Wiegand. Development of a thermogravitational microcolumn with an interferometric contactless detection system. *J. Phys. Chem. B*, 116(47):13889–13897, 2012.
- [88] C. Nieto-Draghi, J. B. Avalos, and B. Rousseau. Computing the soret coefficient in aqueous mixtures using boundary driven nonequilibrium molecular dynamics. *J. Chem. Phys.*, 122:114503, 2005.
- [89] H. Ning, J. Buitenhuis, J. K. G. Dhont, and S. Wiegand. Thermal diffusion behavior of hard sphere suspensions. *J. Chem. Phys.*, 125:204911, 2006.
- [90] H. Ning, S. Datta, T. Sottmann, and S. Wiegand. Soret effect of nonionic surfactants in

- water studied by different transient grating setups. *J. Phys. Chem. B*, 112(35):10927–10934, 2008.
- [91] H. Ning, J. K. G. Dhont, and S. Wiegand. Thermal-diffusive behavior of a dilute solution of charged colloids. *Langmuir*, 24(6):2426–2432, 2008.
- [92] H. Ning, R. Kita, H. Kriegs, J. Luettmer-Strathmann, and S. Wiegand. Thermal diffusion behavior of nonionic surfactants in water. *J. Phys. Chem. B*, 110:10746–10756, 2006.
- [93] H. Ning, R. Kita, and S. Wiegand. Soret effect in a nonionic surfactant system. *Progr. Colloid Polym. Sci.*, 133:111–115, 2006.
- [94] G. V. Paolini and G. Ciccotti. Cross thermotransport in liquid-mixtures by nonequilibrium molecular-dynamics. *Phys. Rev. A*, 35(12):5156–5166, 1987.
- [95] A Parola and R. Piazza. Particle thermophoresis in liquids. *Eur. Phys. J. E.*, 15:255–263, 2004.
- [96] A. Perronace, G. Ciccotti, F. Leroy, A. H. Fuchs, and B. Rousseau. Soret coefficient for liquid argon-krypton mixtures via equilibrium and nonequilibrium molecular dynamics: A comparison with experiments. *Phys. Rev. E*, 66(3):art. no.–031201, 2002.
- [97] A. Perronace, C. Leppla, F. Leroy, B. Rousseau, and S. Wiegand. Soret and mass diffusion measurements and molecular dynamics simulations of n-pentane-n-decane mixtures. *J. Chem. Phys.*, 116(9):3718–3729, 2002.
- [98] R. Piazza. Thermal diffusion in ionic micellar solutions. *Phil. Mag.*, 83(17-18):2067–2085, 2003.
- [99] R. Piazza and A. Guarino. Soret effect in interacting micellar solutions. *Phys. Rev. Lett.*, 88(20):208302, 2002.
- [100] R. Piazza and A. Parola. Thermophoresis in colloidal suspensions. *J. Phys.: Condens. Mat.*, 20(15):153102–153120, 2008.
- [101] J. K. Platten, M. M. Bou-Ali, P. Costesque, J. F. Dutrieux, W. Köhler, C. Leppla, S. Wiegand, and G. Wittko. Benchmark values for the soret, thermal diffusion and diffusion coefficients of three binary organic liquid mixtures. *Phil. Mag.*, 83(17-18):1965–1971, 2003.
- [102] J. K. Platten, M. M. Bou-Ali, and J. F. Dutrieux. Enhanced molecular separation in inclined thermogravitational columns. *J. Phys. Chem. B*, 107(42):11763–11767, 2003.
- [103] J. K. Platten, M. M. Bou-Ali, and J. F. Dutrieux. Precise determination of the soret, thermodiffusion and isothermal diffusion coefficients of binary mixtures of dodecane, isobutylbenzene and 1,2,3,4-tetrahydronaphthalene (contribution of the university of mons to the benchmark test). *Phil. Mag.*, 83(17-18):2001–2010, 2003.
- [104] J. K. Platten and G. Chavepeyer. Instability and heat-flow in 2-constituent benard problem with positive soret coefficients. *Int. J. Heat Mass Transf.*, 19(1):27–32, 1976.

- [105] P. Polyakov, J. Luettmmer-Strathmann, and S. Wiegand. Study of the thermal diffusion behavior of alkane/benzene mixtures by thermal diffusion forced rayleigh scattering experiments and lattice model calculations. *J. Phys. Chem. B*, 110(51):26215–26224, 2006.
- [106] P Polyakov and S. Wiegand. Investigation of the soret effect in aqueous and non-aqueous mixtures by the thermal lens technique. *Phys. Chem. Chem. Phys.*, 11:864–871, 2009.
- [107] P. Polyakov, M. Zhang, F. Müller-Plathe, and S. Wiegand. Thermal diffusion measurements and simulations of binary mixtures of spherical molecules. *J. Chem. Phys.*, 127(1):014502, 2007.
- [108] J.E. Powers. Thermal diffusion. In H.M. Schoen, editor, *New Chemical Engineering Separation Techniques*, pages 1–98. Interscience Publishers, New York, 1962.
- [109] S. W. Provencher. Contin - a general-purpose constrained regularization program for inverting noisy linear algebraic and integral-equations. *Comp.r Phys. Commun.*, 27(3):229–242, 1982.
- [110] S. A. Putnam and D. G. Cahill. Transport of nanoscale latex spheres in a temperature gradient. *Langmuir*, 21(12):5317–5323, 2005.
- [111] S. A. Putnam, D. G. Cahill, and G. C. L. Wong. Temperature dependence of thermodiffusion in aqueous suspensions of charged nanoparticles. *Langmuir*, 23(18):9221–9228, 2007.
- [112] J. Rauch and W. Köhler. Collective and thermal diffusion in dilute, semidilute, and concentrated solutions of polystyrene in toluene. *J. Chem. Phys.*, 119(22):11977–11988, 2003.
- [113] J. Rauch and W. Köhler. Diffusion and thermal diffusion of semidilute to concentrated solutions of polystyrene in toluene in the vicinity of the glass transition. *Phys. Rev. Let.*, 88(18):185901, 2002.
- [114] J. Rauch and W. Köhler. On the molar mass dependence of the thermal diffusion coefficient of polymer solutions. *Macromolecules*, 38:3571–3573, 2005.
- [115] Lord Rayleigh. The incidence of light upon a transparent sphere of dimensions comparable with the wave-length. *Proc. R. Soc. London Ser. A*, 84:25–46, 1910.
- [116] Z. S. A. Rehim and M. A. Ziada. Thermal behavior study of salt-gradient solar pond located in cairo. *Energy Sources Part a-Recovery Utilization and Environmental Effects*, 30(4):349–360. 250TU.
- [117] D. Reith and F. Müller-Plathe. On the nature of thermal diffusion in binary lennard-jones liquids. *J. Chem. Phys.*, 112(5):2436–2443, 2000.
- [118] E. Ruckenstein. Can phoretic motions be treated as interfacial-tension gradient driven phenomena. *J. Colloid Interf. Sci.*, 83(1):77–81, 1981.
- [119] R. Rusconi, L. Isa, and R. Piazza. Thermal-lensing measurement of particle thermophoresis in aqueous dispersions. *J. Opt. Soc. Am. B*, 21(3):605–616, 2004.

- [120] A. I. Rushdi and B. R. T. Simoneit. Lipid formation by aqueous fischer-tropsch-type synthesis over a temperature range of 100 to 400 degrees c. *Origins of Life and Evolution of the Biosphere*, 31(1-2):103–118, 2001.
- [121] W. M. Rutherford. Effect of mass distribution on the isotopic thermal diffusion of substituted benzenes. *J. Chem. Phys.*, 81(12):6136–6139, 1987.
- [122] M. P. Santos, S. L. Gomez, E. Bringuier, and A. M. F. Neto. Thermodiffusion in a multicomponent lyotropic mixture in the vicinity of the critical micellar concentration by using the z-scan technique. *Phys. Rev. E*, 77(1):011403, 2008.
- [123] M. E. Schimpf. Advances in field-flow fractionation for polymer analysis. *Trends in Polymer Science*, 4(4):114–121, 1996.
- [124] M. Schoen and C. Hoheisel. The mutual diffusion coefficient-d12 in binary-liquid model mixtures - molecular-dynamics calculations based on lennard-jones (12-6) potentials. 1. the method of determination. *Mol. Phys.*, 52(1):33–56, 1984.
- [125] S. Semenov and M. E. Schimpf. Molecular thermodiffusion (thermophoresis) in liquid mixtures. *Phys. Rev. E*, 72:041202, 2005.
- [126] Kyoko Shinzawa-Itoh, Hidefumi Ueda, Shinya Yoshikawa, Hiroshi Aoyama, Eiki Yamashita, and Tomitake Tsukihara. Effects of ethyleneglycol chain length of dodecyl polyethyleneglycol monoether on the crystallization of bovine heart cytochrome c oxidase. *Journal of Molecular Biology*, 246(5):572–575, 1995.
- [127] P. M. Shiundu and J. C. Giddings. Influence of bulk and surface-composition on the retention of colloidal particles in thermal field-flow fractionation. *J. Chromatogr. A*, 715(1):117–126, 1995.
- [128] J.-M. Simon, D.K. Dysthe, A.H. Fuchs, and B. Rousseau. Thermal diffusion in alkane binary mixtures, a molecular dynamics approach. *Fluid Phase Equilibria*.
- [129] C. Soret. Sur l'état d'équilibre que prend au point de vue de sa concentration une dissolution saaline primitivement homogène dont deux parties sont portées a des températures différentes. *Arch. Geneve*, 3:48, 1879.
- [130] C. Soret. Influence de la température sur la distribution des sels dans leurs solutions. 91:289, 1880.
- [131] C. Soret. Sur l'état d'équilibre que prend au point de vue de sa concentration une dissolution saaline primitivement homogène dont deux parties sont portées a des températures différentes. *Ann. Chim. Phys.*, 22:293, 1881.
- [132] T. Sottmann and R. Strey. Shape similarities of ultra-low interfacial tension curves in ternary microemulsion systems of the water-alkane-c(i)e(j) type. *Ber. Bunsen. Phys. Chem.*, 100(3):237–241, 1996.
- [133] T. Sottmann and R. Strey. Ultralow interfacial tensions in water-n-alkane-surfactant systems. *J. Chem. Phys.*, 106(20):8606–8615, 1997.
- [134] T. Sottmann and R. Strey. *Microemulsions*, volume V. Academic Press, 2005.

- [135] J. Srinivasan. Solar pond technology. *Sadhana-Academy Proceedings in Engineering Sciences*, 18:39–55. 1Kt898.
- [136] D. Stadelmaier and W. Köhler. From small molecules to high polymers: Investigation of the crossover of thermal diffusion in dilute polystyrene solutions. *Macromolecules*, 41(16):6205–6209.
- [137] R. Strey. Microemulsion microstructure and interfacial curvature. *Colloid. Polym. Sci.*, 272(8):1005–1019, 1994.
- [138] R. Strey. Microemulsion microstructure and interfacial curvature. *Colloid and Polymer Science*, 272(8):1005–1019, 1994.
- [139] R. Strey, J. Winkler, and L. Magid. Small-angle neutron-scattering from diffuse interfaces. 1. monolayers and bilayers in the water octane c12e5 system. *J. Phys. Chem.*, 95(19):7502–7507, 1991.
- [140] N. V. Tabiryan and W. L. Luo. Soret feedback in thermal diffusion of suspensions. *Phys. Rev. E*, 57(4):4431–4440, 1998.
- [141] N. Takeyama and K. Nakashima. Steady-state thermodynamics of thermal-diffusion with micelle formation of aqueous ionic surfactants. *J. Phys. Soc. Japan*, 62:2180–2181, 1993.
- [142] T. Telgmann and U. Kaatze. On the kinetics of the formation of small micelles .1. broadband ultrasonic absorption spectrometry. *J. Phys. Chem. B*, 101(39):7758–7765, 1997.
- [143] T. Tlustý, S. A. Safran, R. Menes, and R. Strey. Scaling laws for microemulsions governed by spontaneous curvature. *Phys. Rev. Lett.*, 78(13):2616–2619, 1997.
- [144] J. Valencia, M. M. Bou-Ali, O. Ecenarro, J. A. Madariaga, and C. M. Santamaria. Validity limits of the fjo thermogravitational column theory. *Thermal Nonequilibrium Phenomena in Fluid Mixtures*, 584:233–249, 2002.
- [145] J. J. Valencia, M. M. Bou-Ali, J. K. Platten, O. Ecenarro, J. M. Madariaga, and C. M. Santamaria. Fickian diffusion coefficient of binary liquid mixtures in a thermogravitational column. *J. Non-Equil. Thermody.*, 32:299–307, 2007.
- [146] D. Vigolo, G. Brambilla, and R. Piazza. Thermophoresis of microemulsion droplets: Size dependence of the soret effect. *Phys. Rev. E*, 75:R040401–1–R040401–4, 2007.
- [147] T. Voelker, E. Blums, and S. Odenbach. Thermodiffusive processes in ferrofluids. *Magnetohydrodynamics*, 37(3):274–278, 2001.
- [148] B. Vonnegut. Rotating bubble method for the determination of surface and interfacial tensions. *Rev. Sci. Instrum.*, 13(1):6–9, 1942.
- [149] Zilin Wang, Hartmut Kriegs, Johan Buitenhuis, Jan Dhont, and Simone Wiegand. Thermophoresis of charged colloidal rods. *Soft matter*, 9:8697–8704, 2013.
- [150] Zilin Wang, Hartmut Kriegs, and Simone Wiegand. Thermal diffusion of nucleotides. *J. Phys. Chem. B*, 116:7463–7469, 2012.

-
- [151] R. Weast, editor. *CRC Handbook of Chemistry and Physics*, volume 58th ed. CRC Press Inc., New York, 1977.
- [152] Franz M. Weinert, Christof B. Mast, and Dieter Braun. Optical fluid and biomolecule transport with thermal fields. *Phys. Chem. Chem. Phys.*, 13(21):9918–9928, 2011.
- [153] S. Wiegand. Thermal diffusion in liquid mixtures and polymer solutions. *J. Phys. Condens. Matter*, 16(10):R357–R379, 2004.
- [154] S. Wiegand, H. Ning, and H. Kriegs. Thermal diffusion forced rayleigh scattering setup optimized for aqueous mixtures. *J. Phys. Chem. B*, 111(51):14169–14174, 2007.
- [155] S. Wiegand, H. Ning, and H. Kriegs. Thermal diffusion forced rayleigh scattering setup optimized for aqueous mixtures. *J. Phys. Chem. B*, 111(51):14169–14174, 2007.
- [156] C. J. Wienken, P. Baaske, U. Rothbauer, D. Braun, and S. Duhr. Protein-binding assays in biological liquids using microscale thermophoresis. *Nat. Commun.*, 1:100, 2010.
- [157] G. Wittko and W. Köhler. Precise determination of the soret, thermal diffusion and mass diffusion coefficients of binary mixtures of dodecane, isobutylbenzene and 1,2,3,4-tetrahydronaphthalene by a holographic grating technique. *Philos. Mag.*, 83(17-18):1973–1987, 2003.
- [158] A. Würger. Thermal non-equilibrium transport in colloids. *Rep. Prog. Phys.*, 73(12):126601–126636, 2010.
- [159] C.L. Yaws. *Chemical Properties Handbook*. McGraw Hill, New York, 1999.
- [160] K. J. Zhang, M. E. Briggs, R. W. Gammon, and J. V. Sengers. Optical measurement of the soret coefficient and the diffusion coefficient of liquid mixtures. *J. Chem. Phys.*, 104(17):6881–6892, 1996.

Erklärung

Ich versichere, dass ich die von mir vorgelegte Dissertation selbständig angefertigt, die benutzten Quellen und Hilfsmittel vollständig angegeben und die Stellen der Arbeit - einschließlich Tabellen, Karten und Abbildungen -, die anderen Werken im Wortlaut oder dem Sinn nach entnommen sind, in jedem Einzelfall als Entlehnung kenntlich gemacht habe; dass diese Dissertation noch keiner anderen Fakultät oder Universität zur Prüfung vorgelegen hat; dass sie - abgesehen von angegebenen Teilpublikationen - noch nicht veröffentlicht worden ist sowie, dass ich eine solche Veröffentlichung vor Abschluß des Promotionsverfahrens nicht vornehmen werde. Die Bestimmungen dieser Promotionsordnung sind mir bekannt. Die von mir vorgelegte Dissertation ist von Prof. Dr. J.K.G Dhont betreut worden.

Ich versichere an Eides Statt, dass die Dissertation von mir selbstständig und ohne unzulässige fremde Hilfe unter Beachtung der "Grundsätze zur Sicherung guter wissenschaftlicher Praxis an der Heinrich-Heine-Universität Düsseldorf" erstellt worden ist.

Philipp Naumann